Vol. 46, No. 5
May 2024

ISSN 1024-1809

METALLOPHYSICS and ADVANCED TECHNOLOGIES

МЕТАЛОФІЗИКА ТА НОВІТНІ ТЕХНОЛОГІЇ

METALLOFIZIKA I NOVEISHIE TEKHNOLOGII

Том 46, № 5 (2024)

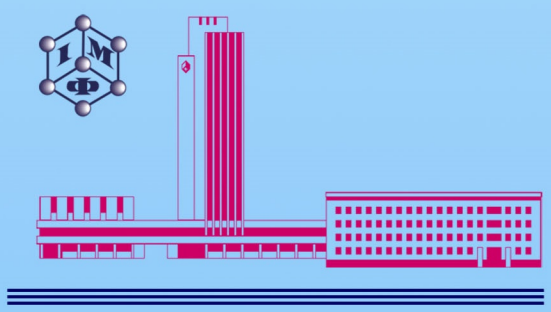

G.V. Kurdyumov Institute for Metal Physics
National Academy of Sciences of Ukraine
https://mfint.imp.kiev.ua

Засновник: Національна академія наук України, Інститут металофізики ім. Г. В. Курдюмова НАН України
Видавець: ВД «Академперіодика» НАН України

«Металофізика та новітні технології» ● 'Metallophysics and Advanced Technologies'

Щомісячний науковий журнал ○ A Monthly Research Journal

NATIONAL ACADEMY OF SCIENCES OF UKRAINE ● G. V. KURDYUMOV INSTITUTE FOR METAL PHYSICS

AN INTERNATIONAL RESEARCH JOURNAL

METALLOPHYSICS AND ADVANCED TECHNOLOGIES

(Metallofizika i Noveishie Tekhnologii)

FOUNDED IN SEPTEMBER, 1979

Volume 46, No. 5; May 2024

CONTENTS

Scientific Editors of Issue—*O. S. Gatsenko, V. A. Tatarenko*
Executive Managing Editor—*O. S. Gatsenko*
Editors—*L. I. Makarenko, M. V. Manilo, I. V. Zagorulko*
The artwork for direct reproduction is made by computer group of EPD of the G. V. Kurdyumov Institute for Metal Physics, N.A.S. of Ukraine

Editorial Office Address:
G. V. Kurdyumov Institute for Metal Physics, N.A.S. of Ukraine, EPD—'MNT',
36 Academician Vernadsky Boulevard, UA-03142 Kyiv, Ukraine
Telephone: +380 44 4249042, +380 44 4241221. Fax: +380 44 4242561. E-mail: mfint@imp.kiev.ua

Registration Certificate of the Publishing Subject: ДК № 5875 on 13.12.2017
State Registration Certificate of the Printed Mass Medium: media identifier R30-03171.

Approved for publication by the Academic Council of the G. V. Kurdyumov Institute for Metal Physics of the National Academy of Sciences of Ukraine
Published in English or Ukrainian languages according to resolution of Editorial Board of the journal

Printed by Publishing House 'Akademperiodyka', of the NAS of Ukraine
4 Tereshchenkivs'ka Str., UA-01024 Kyiv, Ukraine
Registration Certificate of Publishing Subject: ДК № 544 on 27.07.2001

Journal website: http://mfint.imp.kiev.ua
Journal DOI: https://doi.org/10.15407/mfint

Issue DOI: https://doi.org/10.15407/mfint.46.05

НАЦІОНАЛЬНА АКАДЕМІЯ НАУК УКРАЇНИ ● ІНСТИТУТ МЕТАЛОФІЗИКИ ім. Г. В. Курдюмова

МЕТАЛОФІЗИКА ТА НОВІТНІ ТЕХНОЛОГІЇ

МІЖНАРОДНИЙ НАУКОВИЙ ЖУРНАЛ
ЗАСНОВАНИЙ У ВЕРЕСНІ 1979 р.

Том 46, № 5; травень, 2024

ЗМІСТ

Наукові редактори випуску: *О. С. Гаценко, В. А. Татаренко*
Відповідальний секретар редакційної колегії *О. С. Гаценко*
Редактор-коректор *О. С. Гаценко*
Технічні редактори *І. В. Загорулько, Л. І. Макаренко, М. В. Маніло*
Художні редактори *І. В. Загорулько, Л. І. Макаренко, М. В. Маніло*
Оригінал-макет для прямого репродукування виготовлено комп'ютерною групою РВВ Інституту металофізики ім. Г. В. Курдюмова НАН України

Адреса редакції:
Інститут металофізики ім. Г. В. Курдюмова НАН України, РВВ—Редакція «МНТ»
бульв. Акад. Вернадського, 36; 03142 Київ, Україна
Тел.: +380 44 4249042; факс: +380 44 4242561
Ел. пошта: mfint@imp.kiev.ua
Свідоцтво суб'єкта видавничої справи: ДК № 5875 від 13.12.2017 р.
Свідоцтво про державну реєстрацію друкованого засобу масової інформації: Ідентифікатор медіа R30-03171.

Затверджено до друку вченою радою Інституту металофізики ім. Г. В. Курдюмова НАН України
Друкується за постановою редакційної колегії журналу англійською або українською мовами

Підписано до друку 30.05.2024 р. Формат 70 × 100/16.
Ум. друк. арк. 11,29. Обл.-вид. арк. 10,39.
Тираж 55 пр. Зам. № 7345 від 08.07.2024 р.

Віддруковано ВД «Академперіодика» НАН України
вул. Терещенківська, 4; 01024 Київ, Україна
Свідоцтво суб'єкта видавничої справи ДК № 544 від 27.07.2001 р.

Сайт журналу: http://mfint.imp.kiev.ua
DOI (журналу): https://doi.org/10.15407/mfint
DOI (випуску): https://doi.org/10.15407/mfint.46.05

INFORMATION (GUIDELINES) FOR CONTRIBUTORS

Submission of Manuscripts: Manuscripts should be sent by e-mail (mfint@imp.kiev.ua). Additionally, they can be sent by regular mail to Executive Managing Editor, Editorial Office, G. V. Kurdyumov Institute for Metal Physics, N.A.S. of Ukraine, 36 Academician Vernadsky Boulevard, UA-03142 Kyiv, Ukraine. Manuscripts may also be submitted to a member of the Editorial Advisory Board or to the appropriate Regional Editor who is familiar with the research presented.
Submission of a paper to '*Metallophysics and Advanced Technologies*' (transliteration: '*Metallofizika i Noveishie Tekhnologii*', *i.e.*, '*MfNT*') will be taken to imply that it represents original work not previously published, that it is not being considered for publication elsewhere, and that, if accepted for publication, it will not be republished without the consent of the Editors and Publisher. It is a condition of acceptance by the Editor of a manuscript for publication that the Publishers acquire automatically the copyright in the manuscript throughout the world. Journal '*MfNT*' supports the generally accepted principles described in documents on publication ethics and unacceptable practices, which are presented on the journal website.
Scope of the Journal: *Electronic Structure and Properties, Crystal-Lattice Defects, Phase Transformations, Physics of Strength and Plasticity, Metallic Surfaces and Films, Structure and Properties of Nanoscale and Mesoscopic Materials, Amorphous and Liquid States, Interactions of Radiation and Particles with Condensed Matter, Materials in Extremal Conditions, Reactor and Aerospace Metals Science, Medical Metals Science, New Metallic Materials and Synthetic Metals, Metal-Containing Smart Materials, Physical and Technical Basis of Experiment and Diagnostics, Articles under Discussion*.
Language: The language of publication may be English (preferably) or Ukrainian.
Abstract: Each paper requires an abstract of 200–250 words summarizing the significant coverage and findings (the use of mathematical symbols and expressions in abstract is not recommended).
Keywords and PACS numbers: 5–7 keywords and PACS numbers reflecting the content of the contribution should be supplied (see 'Physics and Astronomy Classification Scheme 2010').
Manuscript Preparation: Papers should be formatted according to the template, which can be downloaded from the Journal's website. The length of **research papers** should not in general exceed 5000 words and 10 figures; **review articles** should not exceed 10000 words and 30 figures, including tables and diagrams. Authors are urged to arrange the subject matter clearly under headings such as: 1. Introduction, 2. Experimental/Theoretical Details, 3. Results, 4. Discussion, 5. Conclusion, References. Subsections should be identified with section and subsection numbers (such as 6.1. Second-Value Subheading).
References and Notes: Notes are indicated in the text by consecutive superior Arabic numbers (without parentheses). References should be numbered consecutively (in square brackets) throughout the text. The full list should be collected and typed at the end of the paper in numerical order. Listed references should be completed in all details including **DOI** (if available) but excluding article titles in journals. **All authors'** initials should precede their names. Examples of references preparation:

1. S. O. Firstov and T. G. Rogul, *Metallofiz. Noveishie Tekhnol.*, **44**, No. 1: 127 (2022) (in Ukrainian). https://doi.org/10.15407/mfint.44.01.0127
2. V. B. Tarelnyk, O. P. Gaponova, and Ye. V. Konoplianchenko, *Prog. Phys. Met.*, **23**, No. 1: 27 (2022). https://doi.org/10.15407/ufm.23.01.027
3. A. Meisel, G. Leonhardt, and R. Szargan, *Röntgenspektren und Chemische Bindung* [X-Ray Spectra and Chemical Bond] (Leipzig: Akademische Verlagsgesellschaft Geest & Portig K.-G.: 1977) (in German).
4. J. M. Ziman, *Printsipy Teorii Tverdogo Tela* [Principles of the Theory of Solids] (Moscow: Mir: 1974) (Russian translation).
5. M. A. Stucke, D. M. Dimiduk, and D. M. Hazzledine, *High Temperature Ordered Intermetallic Alloys. V* (Eds. I. Baker and R. Darolia) (Pittsburgh, PA, USA: MRS: 1993), p. 471.
6. *Handbook of Mathematical Functions with Formulas, Graphs and Mathematical Tables* (Eds. M. Abramowitz and I. A. Stegun), Nat'l Bureau of Standards. Appl. Math. Ser. Vol. **55** (Washington, D.C.: U.S. Govt. Printing Office: 1964).
7. B. B. Karpovych and O. B. Borovkoff, *Proc. of Symp. 'Micromaterials Engineering' (Dec. 25–31, 1999)* (Kyiv: RVV IMF: 2000), vol. **2**, p. 113 (in Russian).
8. A. E. Krug, *Abstr. Int. Conf. Phys. Phenomena (Dec. 25–31, 1991, Alushta)* (Kharkiv: 1991), p. 12.
9. T. M. Radchenko, *Vplyv Uporyadkuvannya Defektnoyi Struktury на Transportni Vlastyvosti Zmishanykh Krystaliv* [Influence of Ordering of the Defect Structure on Transport Properties of the Mixed Crystals] (Thesis of Disser. for the Degree of Dr. Phys.-Math. Sci.) (Kyiv: G. V. Kurdyumov Institute for Metal Physics, N.A.S.U.: 2015) (in Ukrainian). https://doi.org/10.13140/RG.2.2.35430.22089

10. E. M. Gololobov, V. B. Shipilo, N. I. Sedrenok, and A. I. Dudyak, *Sposob Polucheniya Karbonitridov Metallov* [Production Method of Metal Carbonitrides], Authors' Certificate 722341 SSSR (Publ. November 21, 1979) (in Russian).
11. V. G. Trubachev, K. V. Chuistov, V. N. Gorshkov, and A. E. Perekos, *Sposob Polucheniya Metallicheskikh Poroshkov* [The Technology of Metallic Powder Production]: Patent 1639892 SU. MKI, B22 F9/02, 9/14 (Otkrytiya i Izobreteniya, **34**, No. 13: 11) (1991) (in Russian).
12. Yu. M. Koval' and V. V. Nemoshkalenko, *O Prirode Martensitnykh Prevrashcheniy* [On the Nature of Martensitic Transformations] (Kyiv: 1998) (Prepr./N.A.S. of Ukraine. Inst. for Metal Physics. No. 1, 1998) (in Russian).

Journal title abbreviations should conform to generally accepted styles:
https://www.cas.org/support/documentation/references/corejournals;
https://cdn.journals.aps.org/files/rmpguapb.pdf;
https://images.webofknowledge.com/WOK46P9/help/WOS/A_abrvjt.html;
https://mathscinet.ams.org/msnhtml/serials.pdf.

Equations and Formulae: Formulas in the text should be inserted by **MathType**, fully compatible with MS Office. Vectors should be typed in bold without arrows above. Note that complicated formulae, mathematical expressions or (de)notations are not recommended in the title, abstract, and keywords.

Tables: Number tables consecutively with Arabic numerals and give a clear descriptive caption at the top.

Figures: All figures should be numbered with consecutive Arabic numbers, have descriptive captions and be mentioned in the text. Keep figures separate at the end of the text and clearly label each figure with author's name and figure number. The labels at axis should contain the designation (or notation) of quantities and their units.

Preparation: Figures submitted must be of a high enough standard for reproduction with 300–600 dpi resolution (including half-tone illustrations). Redrawing or retouching of unusable figures will be charged to the authors.

Colour Plates: Whenever, the use of colour is an integral part of the research, or where the work is generated in colour, the Journal will publish (in paper version) the colour illustrations with charge to the author. Reprints in colour will carry a surcharge. Please write to the Publisher for details.

Submission of Electronic Text: Authors should submit the electronic version of their paper by e-mail to the Editorial Office. The text file should be saved in the native formats of the MS Word with a name consisting the name of the first author, for example, Hotovchenko.docx. The electronic form of figures (in TIF, EPS, JPG, PNG formats preferably and with name consisting the name of the first author also, for example, Hotovchenko_fig2a.jpg) should be planned so that they reduce to 12.7 cm column width (or less), and keep them separated from the text file. It is desirable to submit additionally all the **figures** within the format of the program, in which they were created.

Proofs: Contributors will receive page proofs for correction by e-mail as a PDF document. These must be returned to Kyiv office (mfint@imp.kiev.ua with subject beginning by word 'mfint') within 5 days of receipt.

Page Charges: There are no page charges to individuals or institutions.

Reprints: Authors can freely download a PDF version of their published article from journal website: https://mfint.imp.kiev.ua. The printed issues may be ordered by completing the appropriate form sent with proofs and prepaid by authors under the terms as for subscription.

Further Information: All questions arising during the **peer review** or after acceptance of manuscripts, especially those relating to reprints, should be directed to G. V. Kurdyumov Institute for Metal Physics, N.A.S. of Ukraine, Executive Managing Editor, Editorial Office, 36 Academician Vernadsky Blvd., UA-03142 Kyiv, Ukraine;
Fax: +380 44 4242561, e-mail: mfint@imp.kiev.ua (with subject beginning by word 'mfint').
We ask the authors to apply with their manuscript Copyright Transfer Agreement form.

Copyright Transfer Agreement

We, the undersigned authors of the manuscript '_____', transfer to the Founders, Publisher, and Editorial Board of the Journal 'Metallophysics and Advanced Technologies' (according to agreements between them) the right to publish this manuscript in original language or in translation to the other languages. We confirm that publication of this manuscript **will not** infringe a copyright of other persons or organizations and publication ethics.

Author(s):_____
(Last Name, First Name, Affiliation)

Correspondence Address:_____

Phone and e-mail: _____

_____ _____
(Signature) *(Date)*

ІНФОРМАЦІЯ (ПРАВИЛА) ДЛЯ АВТОРІВ

Науковий журнал «Металофізика та новітні технології» (МфНТ) щомісяця публікує статті, які раніше ще не публікувалися та не перебувають на розгляді для опублікування в інших виданнях. Статті мають містити результати експериментальних і теоретичних досліджень в області фізики та технологій металів, стопів і сполук з металічними властивостями; рецензії на монографії; інформацію про конференції, семінари; відомості з історії металофізики; рекламу нових технологій, матеріялів, приладів. Журнал дотримується загальноприйнятих принципів, зазначених на його сайті в документах з публікаційної етики та щодо неприйнятних практик.

Тематика журналу: *Електронні структура та властивості, Дефекти кристалічної ґратниці, Фазові перетворення, Фізика міцности та пластичности, Металічні поверхні та плівки, Будова та властивості наномасштабних і мезоскопічних матеріялів, Аморфний і рідкий стани, Взаємодії випромінення та частинок із конденсованою речовиною, Матеріяли в екстремальних умовах, Реакторне й авіакосмічне металознавство, Медичне металознавство, Нові металеві матеріяли та синтетичні метали, Металовмісні смарт-матеріяли, Фізико-технічні основи експерименту та діягностики, Дискусійні повідомлення*.

Статті публікуються однією з двох мов: англійською (віддається перевага) або українською.

Статті, в оформленні яких не дотримано наступних правил для опублікування в МфНТ, повертаються авторам без розгляду по суті. (Датою надходження вважається день повторного надання статті після дотримання зазначених нижче правил.)

1. Стаття має бути підписаною всіма авторами (із зазначенням їхніх адрес електронної пошти); слід вказати прізвище, ім'я та по батькові автора, з яким редакція буде вести листування, його поштову адресу, номери телефону та факсу й адресу електронної пошти.

2. Виклад матеріялу має бути чітким, **структурованим** (розділами, наприклад, «1. Вступ», «2. Експериментальна/Теоретична методика», «3. Результати та їх обговорення», «4. Висновки», «Цитована література»), стислим, без довгих преамбул, відхилень і повторів, а також без дублювання в тексті даних таблиць, рисунків і підписів до них. Анотація та розділ «Висновки» мають не дублювати один одного. Числові дані слід наводити в загальноприйнятих одиницях.

3. Об'єм оригінальної (неоглядової) статті має бути не більше 5000 слів (з урахуванням основного тексту, таблиць, підписів до рисунків, списку використаних джерел) і 10 рисунків. **Об'єм оглядової статті** — до 10000 слів та 30 рисунків.

4. За потреби до редакції може надаватися друкований (А4, подвійний інтервал) примірник рукопису з ілюстраціями.

5. До редакції обов'язково надається (по **e-mail**) файл статті, набраний у текстовому редакторі Microsoft Word, з назвою, що складається з прізвища першого автора (латиницею), наприклад, Hotovchenko.docx.

6. Електронна версія рукопису та його друкований варіянт (в разі його надання) мають бути ідентичними. Вони мають оформлюватися за шаблоном, який можна завантажити з сайту журналу, і містити 5–7 **індексів PACS** в редакції 'Physics and Astronomy Classification Scheme 2010'. Тексти статей мають також містити **назву статті**, **список авторів**, **повні назви** та **поштові адреси установ**, в яких вони працюють, **анотацію статті** (200–250 слів), **5–7 ключових слів** двома мовами (**англійською** та **українською**), а заголовки таблиць і підписи до рисунків мають подаватися **як мовою рукопису, так і англійською мовою**; англомовна анотація може бути представленою в більш розгорнутому варіянті (до 500 слів). Назва статті, її анотація та ключові слова мають не містити складні формули, математичні вирази чи позначення.

7. Електронні версії рисунків мають бути представленими у вигляді окремих файлів (у форматах TIF, EPS, JPG, PNG з розріженням у 300–600 dpi) з назвами, що складаються з прізвища першого автора (латиницею) та номера рисунка, наприклад, Hotovchenko_fig2a.jpg. Додатково рисунки надаються у форматі програми, в якій вони створювалися.

8. Написи на рисунках (особливо на півтонових) слід по можливості замінити літерними позначеннями (набраними на контрастному фоні), а криві позначити цифрами або різними типами ліній/маркерів, які мають бути роз'ясненими в підписах до рисунків або в тексті. На графіках усі лінії/маркери мають бути достатньої товщини/розміру для якісного відтворення їх у зменшеному в 2–3 рази вигляді (рекомендована початкова ширина рисунка — 12,7 см). Світлини мають бути чіткими та контрастними, а написи та позначення мають не закривати істотні деталі (для чого можна використовувати стрілки). Замість зазначення в підтекстовці збільшення під час зйомки бажано проставити масштаб (на контрастному фоні) на одній з ідентичних світлин. На графіках підписи до осей, **виконані мовою статті**, мають містити позначення (або найменування) величин, що відкладаються вздовж осей, і відділені комою їхні одиниці вимірювання.

9. Формули в текст треба вставляти за допомогою редактора формул **MathType**, сумісного з MS Office. **Вектори** слід набирати напівтовстим шрифтом без стрілок зверху.

10. Рисунки, таблиці, формули, а також підрядкові **примітки (виноски)** мають нумеруватися поспіль по всій статті.

11. Посилання на літературні джерела слід давати у вигляді порядкового номера, надрукованого в рядок у квадратних дужках. Список цитованої літератури складається почергово за першою згадкою джерела. Приклади оформлення посилань наведено нижче (просимо звернути увагу на порядок розташування ініціалів і прізвищ авторів, бібліографічних відомостей і на розділові знаки, а також на необхідність зазначення **всіх** співавторів цитованої роботи та її ідентифікатора **DOI**, якщо він є):

1. S. O. Firstov and T. G. Rogul, *Metallofiz. Noveishie Tekhnol.*, **44**, No. 1: 127 (2022) (in Ukrainian). https://doi.org/10.15407/mfint.44.01.0127
2. V. B. Tarelnyk, O. P. Gaponova, and Ye. V. Konoplianchenko, *Prog. Phys. Met.*, **23**, No. 1: 27 (2022). https://doi.org/10.15407/ufm.23.01.027
3. A. Meisel, G. Leonhardt, and R. Szargan, *Röntgenspektren und Chemische Bindung* [X-Ray Spectra and Chemical Bond] (Leipzig: Akademische Verlagsgesellschaft Geest & Portig K.-G.: 1977) (in German).
4. J. M. Ziman, *Printsipy Teorii Tverdogo Tela* [Principles of the Theory of Solids] (Moscow: Mir: 1974) (Russian translation).
5. M. A. Stucke, D. M. Dimiduk, and D. M. Hazzledine, *High Temperature Ordered Intermetallic Alloys. V* (Eds. I. Baker and R. Darolia) (Pittsburgh, PA, USA: MRS: 1993), p. 471.
6. *Handbook of Mathematical Functions with Formulas, Graphs and Mathematical Tables* (Eds. M. Abramowitz and I. A. Stegun), Nat'l Bureau of Standards. Appl. Math. Ser. Vol. **55** (Washington, D.C.: U.S. Govt. Printing Office: 1964).
7. B. B. Karpovych and O. B. Borovkoff, *Proc. of Symp. 'Micromaterials Engineering' (Dec. 25–31, 1999)* (Kyiv: RVV IMF: 2000), vol. **2**, p. 113 (in Russian).
8. A. Eh. Krug, *Abstr. Int. Conf. Phys. Phenomena (Dec. 25–31, 1991, Alushta)* (Kharkiv: 1991), p. 12.
9. T. M. Radchenko, *Vplyv Uporyadkuvannya Defektnoyi Struktury na Transportni Vlastyvosti Zmishanykh Krystaliv* [Influence of Ordering of the Defect Structure on Transport Properties of the Mixed Crystals] (Thesis of Disser. for the Degree of Dr. Phys.-Math. Sci.) (Kyiv: G. V. Kurdyumov Institute for Metal Physics, N.A.S.U.: 2015) (in Ukrainian). https://doi.org/10.13140/RG.2.2.35430.22089
10. E. M. Gololobov, V. B. Shipilo, N. I. Sedrenok, and A. I. Dudyak, *Sposob Polucheniya Karbonitridov Metallov* [Production Method of Metal Carbonitrides], Authors' Certificate 722341 SSSR (Publ. November 21, 1979) (in Russian).
11. V. G. Trubachev, K. V. Chuistov, V. N. Gorshkov, and A. E. Perekos, *Sposob Polucheniya Metallicheskikh Poroshkov* [The Technology of Metallic Powder Production]: Patent 1639892 SU. MKI, B22 F9/02, 9/14 (Otkrytiya i Izobreteniya, **34**, No. 13: 11) (1991) (in Russian).
12. Yu. M. Koval' and V. V. Nemoshkalenko, *O Prirode Martensitnykh Prevrashcheniy* [On the Nature of Martensitic Transformations] (Kyiv: 1998) (Prepr./N.A.S. of Ukraine. Inst. for Metal Physics. No. 1, 1998) (in Russian).

Слід використовувати загальноприйняті скорочення назв журналів:
https://www.cas.org/support/documentation/references/corejournals;
https://cdn.journals.aps.org/files/rmpguapb.pdf;
https://images.webofknowledge.com/WOK46P9/help/WOS/A_abrvjt.html;
https://mathscinet.ams.org/msnhtml/serials.pdf.

Необхідною вимогою є також надання авторами додаткового списку цитованої літератури (**References**) в **латинській транслітерації** (система **BGN/PCGN**; рекомендовані транслітератори: http://www.slovnyk.ua/services/translit.php; http://ru.translit.net/?account=bgn).

Після транслітерованих назв книг, дисертацій, патентів та ін. слід у квадратних дужках наводити їхній англомовний переклад (див. приклади вище). При транслітерації статей з МфНТ слід використовувати написання П.І.Б. авторів, наведені **лише** в англомовному змісті відповідного випуску, і **офіційну** транслітеровану назву журналу (див. також першу сторінку кожної статті та сайт).

12. Коректура авторам надсилається електронною поштою у вигляді pdf-файлу після завершення етапу **рецензування**. На перевірку коректури авторам відводяться 5 робочих днів. Після закінчення зазначеного терміну стаття автоматично направляється до друку. Виправлення слід відмітити та прокоментувати в самому pdf-файлі або оформити у вигляді переліку виправлень (підписаного уповноваженим представником колективу авторів) і переслати електронною поштою на адресу редакції.

Електронний варіянт статті надсилається на e-mail: mfint@imp.kiev.ua (з темою, що починається словом 'mfint'). Друкована версія рукопису (якщо у ній є потреба) надсилається за адресою: **Інститут металофізики ім. Г. В. Курдюмова НАН України, редакція МфНТ; бульвар Акад. Вернадського, 36; 03142 Київ, Україна** або відповідному реґіональному редактору (див. сайт).

Автори можуть вільно завантажити pdf-файли опублікованих статей з сайту журналу (https://mfint.imp.kiev.ua), а також замовити друковані примірники випуску журналу зі своєю статтею, надіславши до редакції журналу **разом з коректурою відповідну заявку та квитанцію про оплату** друку необхідної кількості примірників випуску на умовах, аналогічних передплатним.

Відповідно до угод між редакцією МфНТ, засновниками та видавцем журналу, редакція вважає, що автори, надсилаючи їй рукопис статті, передають засновникам, видавцю та редколеґії право опублікувати цей рукопис мовою ориґіналу та в перекладі іншими мовами, і просить авторів відразу прикладати до рукопису «Угоду про передачу авторського права».

Угода про передачу авторського права

Ми, що нижче підписалися, автори рукопису «_____», передаємо засновникам, видавцю та редколеґії журналу «Металофізика та новітні технології» (згідно з угодами між ними) право опублікувати цей рукопис мовою ориґіналу та в перекладі іншими мовами. Ми підтверджуємо, що ця публікація **не** порушує авторського права інших осіб або організацій і принципів наукової етики. При цьому за авторами зберігаються всі інші права як власників цього рукопису.

Підписи авторів: _____ (П.І.Б., дата, адреса, тел., e-mail)

Metallophysics and Advanced Technologies
Металофіз. новітні технол.
Metallofiz. Noveishie Tekhnol.
2024, vol. 46, No. 5, pp. 385–413
https://doi.org/10.15407/mfint.46.05.0385
Reprints available directly from the publisher

PACS numbers: 61.66.Dk, 62.20.Qp, 64.70.dj, 81.05.Bx

The Structure and Properties of G-CuZn15Si4 Cast Brass After Inoculation of Its Melt with Dispersed FeCr Intermetallic Component

I. A. Nebozhak, V. G. Novytskyi, Ie. M. Dzevin*, and A. M. Verkhovliuk

Physico-Technological Institute of Metals and Alloys, NAS of Ukraine,
34/1 Academician Vernadsky Blvd.,
UA-03142 Kyiv, Ukraine
**G. V. Kurdyumov Institute for Metal Physics, NAS of Ukraine,*
36 Academician Vernadsky Blvd.,
UA-03142 Kyiv, Ukraine

With using of a dispersed-filled gasifying model, it is possible to inoculate the cast brass of the G-CuZn15Si4 (DIN) alloy with intermetallic FeCr, known in the alloys of the binary Fe–Cr system as the σ phase, and to obtain the test castings. With the use of x-ray spectral microanalysis, the chemical composition of cast samples is determined before and after the process of inoculation of the matrix melt with dispersed intermetallic FeCr. The results of x-ray spectral microanalysis show that the cast composite includes Fe and Cr within 1% that vary along the height of the cast sample, while the chemical composition of the control casting contains half as much Fe and Cr is not detected at all. The metallographic analysis of G-CuZn15Si4 cast brass after inoculation make it possible to detect the inclusions of the σ-phase in the field of the metallographic section that is a sign of the microstructure of the zero-dimensional cast composite material of the Cu–FeCr system, while the microstructure of the control casting is characteristic of G-CuZn15Si4 cast brass. The results of mechanical tests of cast samples and their wear tests under dry-friction conditions allow us to come to the conclusion that the hardness of G-CuZn15Si4 cast brass, which is determined according to the Brinell scale, and its tribotechnical characteristics depend on the height of casts of both types, and on the same properties of cast of the sample after inoculation

Corresponding author: Ivan Anatoliyovych Nebozhak
E-mail: nebozhak@ukr.net

Citation: I. A. Nebozhak, V. G. Novytskyi, Ie. M. Dzevin, and A. M. Verkhovliuk, The Structure and Properties of G-CuZn15Si4 Cast Brass After Inoculation of Its Melt with Dispersed FeCr Intermetallic Component, *Metallofiz. Noveishie Tekhnol.*, **46**, No. 5: 385–413 (2024). DOI: 10.15407/mfint.46.05.0385

with dispersed intermetallide FeCr is affected by Fe and Cr concentrations. Graphical interpretation of the experimental data shows that the mechanical and tribotechnical properties of brass castings after the process of inoculation of the matrix melt by the σ phase significantly exceed the similar characteristics of G-CuZn15Si4 cast brass before inoculation.

Key words: dispersed-filled gas model, dispersed inoculator, composite cast, lost-foam casting process, G-CuZn15Si4 cast brass, matrix melt, tribotechnical properties.

Із застосуванням дисперсно-наповненого моделю, що газифікується, вдалося здійснити інокулювання ливарної латуні марки ЛЦ16К4 інтерметалідом FeCr, відомим у стопах бінарної системи Fe–Cr як σ-фаза, й одержати тестові виливки. За допомогою рентґеноспектральної мікроаналізи було визначено хемічний склад литих зразків до і після процесу інокулювання матричного розтопу дисперсним інтерметалідом FeCr. Результати рентґеноспектральної мікроаналізи показали, що до складу композитного виливка в межах 1% входять Fe і Cr, які змінюються по висоті литого зразка, у той час коли в хемічному складі контрольного виливка Fe вдвічі менше, а Cr взагалі не виявлено. Металографічна аналіза ливарної латуні марки ЛЦ16К4 після інокулювання уможливила виявити в полі металографічного шліфа включення σ-фази, що є ознакою мікроструктури нульвимірного литого композиційного матеріялу системи Cu–FeCr, у той час коли мікроструктури контрольного виливка є характерними для ливарної латуні марки ЛЦ16К4. Результати механічних випробувань литих зразків та їх випробувань на зношування в умовах сухого тертя дали змогу дійти висновку, що твердість ливарної латуні марки ЛЦ16К4, яку було визначено за Брінеллєвою шкалою, та її триботехнічні характеристики залежать від висоти обох типів виливків, а на ті ж самі властивості литого зразка після інокулювання дисперсним інтерметалідом FeCr впливають концентрації Fe та Cr. Графічна інтерпретація експериментальних даних показала, що механічні та триботехнічні властивості латунних виливків після процесу інокулювання матричного розтопу σ-фазою значно перевищують аналогічні характеристики ливарної латуні марки ЛЦ16К4 до інокулювання.

Ключові слова: дисперсно-наповнений газмодель, дисперсний інокулятор, композитний виливок, ЛҐМ-процес, ливарна латунь марки ЛЦ16К4, матричний розтоп, триботехнічні властивості.

(Received 25 January 2024; in final version, 28 March 2024)

1. INTRODUCTION

Brass is a unique structural material with good physical, mechanical and technological characteristics. It has become widespread in almost all branches of the economy. This became possible due to a successful combination of high strength and plasticity with aesthetic appeal.

Foundry brasses are intended for shaped casting of workpieces of

complex configuration. This includes many special additives that improve the pouring properties. Brass castings are characterized by high corrosion resistance, increased strength, and antifriction properties.

As a structural material the foundry grades of brass are used in transport mechanical engineering, as well as for the manufacture of a wide variety of fittings, however, low hardness and wear resistance limit its use in engineering for the manufacture of parts of the machines and mechanisms operating under conditions of abrasive wear.

In present time, a number of technological methods and techniques for improving foundry brasses are known, among which its inoculation occupies a central place, in our case it is reinforcement or composite strengthening. However, the inoculation of foundry brasses by traditional methods is generally a long and uneconomical process. At the same time, the use of special casting methods allows to avoid the specified disadvantages. The most promising method of inoculating brasses is casting according to gasifying models (lost-foam casting process—LFC process), since its main feature is the use of a model that is not removed before filling of the casting mold (CM) by metal, which determines the main advantages of this technological process in comparison with other methods of casting. In addition, the gas model (GM) can be obtained in the volume of the press form (PF) from granular model material.

These circumstances made it possible to introduce dispersed additives into the composition of GM, and thus to solve a twofold task—to inoculate the matrix melt in the 'volume' of the CM and to carry out the utilization of dust-like waste from the ferroalloy industry and foundry production.

In practice, the implantation of inoculators into the 'body' of the GM is go to cold plating of the granules surface of the model material with dispersed ferroalloys before it is blown or filled into the PF volume.

Based on these and other considerations, the goal of this scientific and research work was formulated and set, which consists in the inoculation of molten cast brass of the G-CuZn15Si4 (DIN) alloy with FeCr intermetallic, known in the alloys of the binary system Fe–Cr as the σ phase, with the help of a dispersed-filled gasifying model (DFGM). Since the criteria for evaluating the efficiency of the inoculation process of cast alloys are the absorption indicators of the dispersed inoculant (DI) by the matrix melt, the parameters of the cast samples microstructure, its physical and mechanical and special properties, in order to achieve the goal, it is necessary to investigate the indicators of absorption of the σ phase by the matrix melt, the microstructure of brass castings, its mechanical and tribotechnical properties, as well as to identify factors that significantly effect on these indicators.

2. BASICS OF THEORY AND TECHNOLOGY

2.1. Physics and Chemistry of the LFC Process

Polystyrene foam (PSF) is used in most cases for the manufacture of GM. On an industrial scale, it is obtained in reactors at increased temperatures by the method of suspension styrene polymerization [1]. The physics-and-chemistry and technology of the two-stage polystyrene production process are described in detail by the author of the monograph mentioned above.

At the first stage, ethylene (rational formula C_2H_4) and benzene (rational formula C_6H_6) in the presence of aluminium chloride (chemical formula $AlCl_3$) as a catalyst, ethylene benzene (rational formula C_8H_{10}) produces, which is then subjected to catalytic dehydrogenation and the output is an intermediate product—styrene (rational formula C_8H_8):

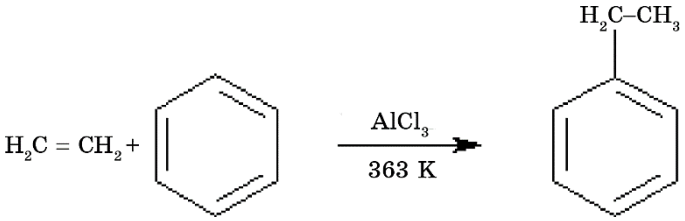

(1)

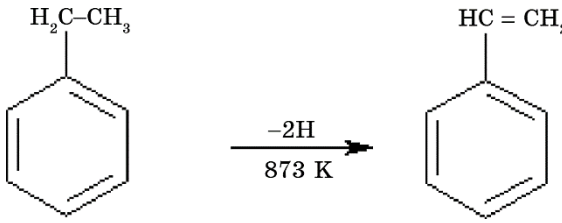

(2)

At the second stage, as a result, the final product is obtained, *i.e.*, polystyrene (rational formula $(C_8H_8)_{n-2}$) in the presence of a potassium persulfate (chemical formula $K_2S_2O_8$) catalyst, by means of suspension polymerization of styrene (rational formula C_8H_8):

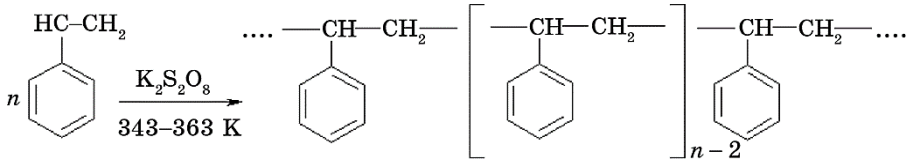

(3)

The physical model of the LFC process as well as the mechanism of the interaction of polystyrene GM with the metal melt are clearly presented and described in the [2]. However, the proposed physical model does not take into account the presence of DI in the system 'metal melt–GM–DI–CM'.

Based on these and other considerations, a physical model of the LFC

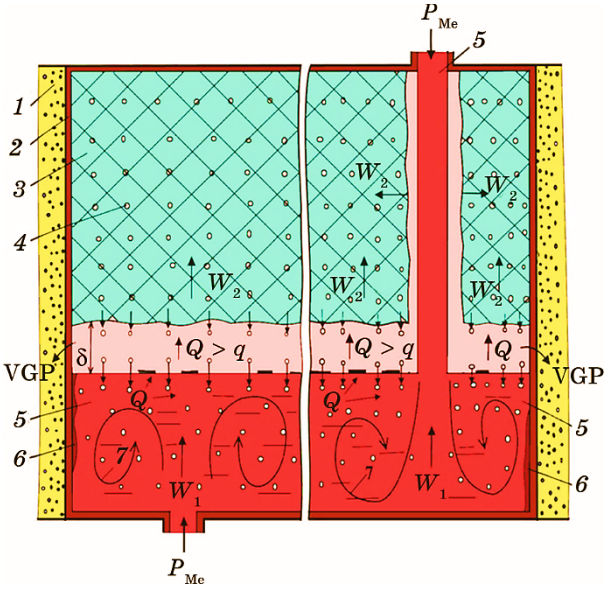

Fig. 1. Physical model of the process of interaction of the matrix melt with the GM and the dispersed inoculator implanted to it during the lower (left) and upper (right) introduction of liquid metal into the 'volume' of the CM [3]: *1* is forming material, *2* is non-stick coating, *3* is gasified model, *4* is dispersed inoculator, *5* is matrix melt, *6* is foundry crust, *7* is convective flows, W_1, W_2 are rates of form filling and thermal destruction of GM, respectively, Q is radiation energy of the matrix melt, q is specific heat of thermal destruction of GM material, VGP is vapour-gas phase, LP is liquid phase, P_{Me} is hydrostatic head of molten metal.

process (Fig. 1) with correction for DFGM was created at the Physico-Technological Institute of Metals and Alloys, N.A.S. of Ukraine (PTIMA) and the heat balance equation of the system under consideration was derived [3]:

$$c_{[Cu-Zn]}\rho_{[Cu-Zn]}\Delta V_{CM}(T_P - T_L^{[Cu-Zn]}) = c_{FeCr}\rho_{FeCr}V_{FeCr}(T_L^{[Cu-Zn]} - T_L^{FeCr}) + \\ + L_{GM}\rho_{GM}\Delta V_{CM} + 1.13 b_{CM}\Delta F_{CM}T_P\sqrt{\tau_P} + L_{FeCr}\rho_{FeCr}V_{FeCr}, \quad (4)$$

where $c_{[Cu-Zn]}$ is the heat capacity of the matrix brass melt, J/(kg·K), $\rho_{[Cu-Zn]}$ is density of matrix brass melt, kg/m^3, ΔV_{CM} is change in the volume of the casting mold in the contact zone with the matrix brass melt, m^3, T_P is pouring temperature, K, $T_L^{[Cu-Zn]}$ is liquidus temperature of matrix brass melt, K, c_{FeCr} is heat capacity of dispersed intermetallic FeCr, J/(kg·K), ρ_{FeCr} is density of dispersed intermetallic FeCr, kg/m^3, V_{FeCr} is volume of dispersed intermetallic FeCr, m^3, T_L^{FeCr} is liquidus temperature of dispersed intermetallide FeCr, K, L_{GM} is specific heat of

thermal destruction of expanded polystyrene, J/kg, ρ_{GM} is density of the material of the gasified model, kg/m^3, b_{CM} is heat-accumulating capacity of the casting mold material, W·s$^{0.5}$/(m^2·K), ΔF_{CM} is change in the surface area of the casting mold in the contact zone with the matrix brass melt, m^2, τ_P is duration of form filling, s, L_{FeCr} is the latent heat of fusion of dispersed FeCr intermetallide, J/kg.

An emphasis is also placed on the convective component of the mass transfer process of DI in the volume of the metal bath, which, according to the condition of form filling in the laminar mode and in the process of crystallization of the matrix brass melt, is predominant.

This can be described using a semi-empirical differential equation of convective diffusion, which for the one-dimensional case will have the form [4]:

$$-\frac{\partial}{\partial x}(\upsilon^{CM}_{[Cu-Zn]} C^{GM}_{FeCr} S)dxdf = \\ = \upsilon^{CM}_{[Cu-Zn]} C^{GM}_{FeCr} Sdf - (\upsilon^{CM}_{[Cu-Zn]} + \frac{\partial \upsilon^{CM}_{[Cu-Zn]}}{\partial x} dx)(C^{GM}_{FeCr} + \frac{\partial C^{GM}_{FeCr}}{\partial x} dx)(S + \frac{\partial S}{\partial x} dx), \quad (5)$$

where x is linear space coordinate (abscissa axis), m, $\upsilon^{CM}_{[Cu-Zn]}$ is the average speed of convective flows of the matrix brass melt in the foundry mold, m/s, C^{GM}_{FeCr} is concentration of dispersed intermetallic FeCr in the 'body' of the gasifying model, kg/m^3, S is relative amount of matrix brass melt in the two-phase zone, f is cross-sectional area of the casting mold in the direction perpendicular to the convective flow of matrix brass melt, m^2.

It has been experimentally proven that the hydro- and gas dynamics of the LFC process actively influence on the indicators of absorption of DI by the matrix melt [5, 6], the parameters of the microstructure of composite castings [6, 7], their mechanical [8] and tribotechnical [9] properties.

Quantitative characteristics of the hydro- and gas dynamics of the LFC process are the volume of gaseous products of thermal destruction of the GM material that seep through the wall of the CM, the thickness of the gap between the mirror of the matrix melt and the GM during mold filling, as well as the total cross-sectional area of all feeders. In the conditions of a real CM, there is a one-dimensional parallel laminar filtration of gases released as a result of the thermal destruction of the PSF, which is directed along the normal to the wall of the CM [10]. The regularities of the gases movement in a capillary-porous environment, which is the CM, can be described by the one-dimensional Darcy filtration equation, according to which the flow of these gases along the ordinate axis, that is, perpendicular to the vertical surface of the CM volume, is proportional to their pressure gradient ($\text{grad}P_{CM} = dP_{CM}/dy$); see Ref. [11]:

$$dV = -D\frac{\sum_{i=1}^{n} S_i dP_{CM}}{\gamma dy}d\tau, \quad (6)$$

where dV is the elementary volume of gas filtered through the thickness of the forming material during the time $d\tau$ due to gradP_{CM}, m^3, D is Darcy filtration coefficient, m^2/s, $\sum_{i=1}^{n} S_i$ is the total cross-sectional area of the filtration flow (including the cross-section of solid particles), m^2, γ is the specific gravity of the filtrate, N/m^3.

The authors of [12], with reference to the results of the study of influence of the various technological factors on the size of the gap between the metal mirror and the GM, obtained by Yu. A. Stepanov and V. G. Moskalyov [13] report that at any moment in time this gap can be described by the equation:

$$\delta = 0.25a\tau_P^m - \mu\frac{F_F}{F_{CM}}\int_0^{\tau_P}\sqrt{2g\left[H_C(\tau) - \frac{F_{CM}(\tau)}{\rho_{Me}}\right]}d\tau, \quad (7)$$

where a is the specific coefficient of gas evolution, cm/s, m is relative coefficient of gas evolution, μ is the mass flow coefficient of the shower system, $\mu = 0.5–0.6$ kg/(cm^2·s), F_F is cross-sectional area of the feeder, cm^2, F_{CM} is cross-sectional area of the casting mold in the area of interaction of the gasifying model with the matrix melt, cm^2, g is acceleration of free fall, $g = 9.80665$ m/s^2 [14], H_C is calculated hydrostatic pressure of the metal melt, cm, τ is current time, s, ρ_{Me} is the density of the matrix melt, kg/m^3.

Calculation of the total cross-sectional area of all feeders in practice is carried out using the ratio proposed by the authors of [15]:

$$\sum_{i=1}^{n}(F_F)_i = \frac{m_C}{0.31\mu\tau_P\sqrt{H_C - P_{CM}/\rho_{Me}}}, \quad (8)$$

where m_C is the mass of cast workpiece, kg, P_{CM} is the pressure of gaseous products of the thermal destruction of polystyrene foam in the gap between the dispersed-filled gas model and the liquid metal mirror, Pa.

First of all, the modes of filling CM with matrix melt and gasification of the model material depend on these factors. Under its influence, the structure of brass castings is formed, which, as a final result, largely effects on the quality indicators of cast samples.

The interaction of the components of system ‘metal melt–GM–DI–CM’ is a complex thermo-physical and physics-chemical process, and the material presented above is not enough to describe it in detail. A large number of treatises by domestic and foreign researchers are de-

voted to this topic. The mechanism of the process of interaction of the system components under consideration is revealed on the example of a zero-dimensional cast composite material (CCM) of the Al–FeCr system and is described in detail in the [16].

2.2. Theoretical Basis of Tribology

Cast brasses, which work for wear under conditions of dry friction with other structural materials (materials of the counterbody (MCB)), a tribological system form together with its. The physical quantities that quantitatively characterize this system [17] in practice are the friction coefficient of the 'brass–MCB' pair, the rate of wear and/or wear of cast brass, as well as the operation of the MCB. The physical meaning of these quantities [17–22], from the point of tribology view, is briefly described below.

According to the definition [18], the coefficient of friction is a value that characterizes the force of resistance from friction between interacting bodies. Depending on the type of friction, a distinction is made [17]: the shear friction coefficient (rest friction, incomplete sliding friction, and sliding friction) and the rolling friction coefficient. These coefficients can be represented using mathematical expressions [18], respectively:

$$f = F_{\mathrm{f}} / N , \tag{9}$$

$$f = k + A_0 / N , \tag{10}$$

where F_{f} is the force of sliding friction, N, N is the force of the normal reaction of the support, N, k is a coefficient depending on the properties of the surfaces of the bodies in contact, A_0 is the adhesion coefficient of these surfaces, N.

According to the authors of [19], friction processes determine energy flows in tribosystems. In order to manage these flows, you need to know the mechanisms of heat generation and friction force formation. For their analysis [19], they adopted a model of tribological contact in the form of an ensemble of connections, that is, diatomic systems that arise in contact when an external loading is applied, in which the elastic forces of such connections then compensate for this loading. According to the created model, which is described in detail by the authors of the same work, the relative number of such bonds is proportional to the ratio of the loading to the modulus of bulk elasticity, and under real loadings it is in the range of 10^{-6}–10^{-4} of the total number of atoms on the contact area. Since, according to the authors [19], the bond strength is equivalent to gradE_{pot} (where E_{pot} is potential energy, J); the friction force arises under the influence of energy. For

their reasons, it can be presented as a dependency:

$$F_f = \frac{n_A P}{K} \int_{r_{min}}^{r_{max}} F(r) p(r) dr , \quad (11)$$

where F_f is the force of sliding friction, N, n_A is the number of atoms per unit of contact area, nm^{-2}, P is loading, N, K is modulus of bulk elasticity, GPa, r is interatomic distance, Å, $F(r)$ is the bond strength in the interatomic distance state, N, $p(r)$ is the probability density of states at the interatomic distance, nm^{-1}.

In turn, the bulk elasticity modulus is a value that characterizes the elastic properties of the material under small deformations. It can be determined by the calculation method [20]:

$$K = E/\{3(1 - 2\mu)\} , \quad (12)$$

where E is the modulus of elasticity (Young's modulus) ($E = 70–74$ GPa (Al alloys), $E = 190–210$ GPa (steel), $E = 78–123$ GPa (brass)), μ is Poisson's ratio ($\mu = 0.30–0.33$ (Al alloys), $\mu = 0.27–0.30$ (steels), $\mu = 0.37$ (brass)).

The amount of wear is a change in the geometric dimensions and shape of solids, which are determined by the participation of their substance in the formation of tribostructures. The flow of this substance, averaged over the contact plane of the touching bodies, is equivalent to the wear rate of the material of the test sample [21]:

$$i(t) = dI(t)/dt , \quad (13)$$

where t is the current time, s, $I(t)$ is material wear, mg/(cm²·km).

The process of material wear over time, according to M. V. Kindrachuk and colleagues [19, 21, 22], consists of 2 non-equivalent stages: run-in and steady state. At the preparation stage, tribological structures are formed, and then the process fluctuates in a stationary mode with a constant average value and dispersion. Excessive growth of the tribostructure is limited by entropy, and its lower level is limited by free energy.

Equations that analytically describe the functional dependence of the wear rate of material under test and its wear, respectively, on the current time, are clearly presented below [22]:

$$i(t) = (i_0 - < i >) \exp(-t / t_R) + < i > , \quad (14)$$

$$I(t) = t_R (i_0 - < i >)(1 - \exp(-t / t_R)) + t < i > , \quad (15)$$

where i_0 and $<i>$ are the initial and average steady-state values of material wear rate, respectively, mg/(cm²·km·s), t_R is the relaxation time

of running-in, s.

The exponents on the right-hand side of equations (14) and (15), according to the authors describe the evolutionary process of material wear-in, while the wear-in duration estimates the relaxation time, and the contribution of material wear-in to its wear is a functional [22]:

$$I_0 = t_R(i_0 - < i >)(1 - \exp(-t / t_R)) . \quad (16)$$

At this stage, the desire for free energy to a minimum prevails, in the contact zone of the bodies that form a friction pair, aggregation of transported particles occurs, internal flows of matter are directed to the formation of a tribological structure and an increase in its volume, and the flow of matter from of the system decreases until it reaches a stationary level [22]. In a stationary state, the tribostructure fluctuates near the average value, during one fluctuation part of the substance leaves this system in the form of material wear products, and then the tribological structure is restored [22].

If the tribological structure of the material under study is restored at a time interval τ, then its wear $I(t)$ at the same interval can be considered as an independent physical quantity. Then, according to the central limit theorem, the authors of [22] develop their opinion: at $t >> \tau$, the wear of this material $I(t)$ has a normal distribution and can be represented using mathematical expressions as follow:

$$I(t) = t < i > \pm \eta\sigma\tau\sqrt{t / \tau} , \quad (17)$$

$$< i >= I(t) / t \pm \eta\sigma\tau\sqrt{t / \tau} , \quad (18)$$

where η is a Gaussian variable with unit variance, σ is the root mean square deviation of the arithmetic mean, τ is correlation time interval, s.

According to the authors of [19], the tribostructure is a special state of matter that is arbitrarily formed under conditions of tribological contact that are far from equilibrium. According to M. V. Kindrachuk and E. A. Kulgavyi [19], stable equilibrium states in liquids and gaseous substances correspond to the maximum entropy, that is, the uniform distribution of matter in space. The structure of solids, the authors of the same paper continue their opinion, is determined by the desire of free energy to be minimized, and this determines the crystalline structure of the substance.

3. METHODS

3.1. Subject and Object of Research

As cast brass of the G-CuZn15Si4 (DIN) alloy is characterized by high

casting and technological properties [23], which was already mentioned earlier, the influence of the technological parameters of the LFC process and other independent factors during the inoculation of brasses on its mechanical and tribotechnical characteristics was studied using the example of this commercially available alloy. As an inoculator of the matrix melt a dispersed intermetallic FeCr better known in the alloys of the binary system Fe–Cr as the σ phase was used, which was also mentioned earlier, in the amount of 7% of the volume of the control casting which is equivalent to 6.3% wt. More detailed information about these materials and technology of their preparation is given below in the text.

3.2. Technology of the Inoculation Process

Dispersed-filled gasifying model (Fig. 2, *a*) was obtained by the autoclave method [2, 10–12, 15] from PSF with introduced FeCr intermetallide powder. Implantation of the dispersed σ phase in the 'body' of the GM was made by cold plating of the surface of PSF granules with it before PF blowing into the volume [24, 25]. A solution of polyvinyl butyral (rational formula $(C_8H_{14}O_2)_n$) of the 'SDW-3A' trademark in rectified ethyl alcohol (chemical formula C_2H_5OH) was used as an adhesive [24]. GM without additive (Fig. 2, *b*) was also produced by the autoclave method from 'pure' PSF. In order to prevent the formation of scorch on the surface of future castings, a non-stick coating was applied to the GM. The characteristics of model materials will be presented below.

For the manufacture of GM, PSF was used, which was obtained from cast polystyrene (density 1069–1125 kg/m^3) of the 'STMMA-FD' (Castchem, China) trademark. This polystyrene was specially devel-

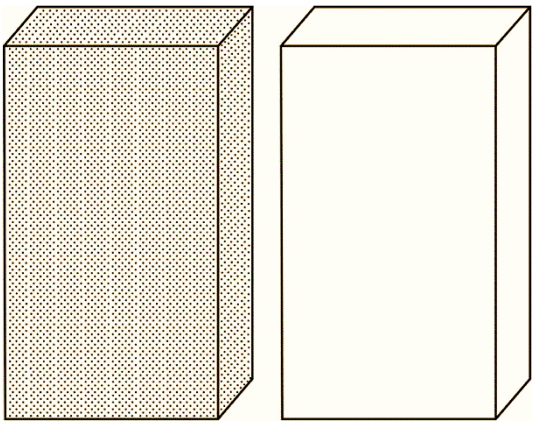

Fig. 2. Appearance of gasified models (diagram): dispersed-filled (*a*), without additive (*b*).

oped for the 'Lost Foam' casting technology, that is, LFC process. The PSF used in the process of implementing this work is characterized by such indicators as: dispersion of the original material (rational formula $(C_8H_8)_{n-2}$) is 0.2–0.4 mm, apparent density is 25 kg/m^3, sintering time is 150 s (DFGM), 120 s (GM without additive).

Dispersed intermetallic FeCr was obtained from cast samples of a high-chromium alloy based on Fe. For this, the piece material was preannealed in a laboratory muffle furnace of the model СНО-2,5.5.2,5/13,6 И1 for the formation and separation of the σ phase from a solid solution of Cr in Fe, crushed in a laboratory jaw crusher of the model «Вибротехник ЩД-10 6411-00013» and sifted through sieves. Characteristics of dispersed inoculant (DI): annealing temperature is 1073 K, time of isothermal exposure is 3600 s, dispersion is 20–100 μm, shape of particles is scaly, and unevenness factor is 2–5. The chemical composition of DI (Table 1) is given below in the text.

It was possible to obtain FeCr intermetallide powder of a given dispersion thanks to sieve analysis. For this, a set of laboratory sieves made of woven wire fabric was used, which is regulated by relevant regulatory documents, in particular ДСТУ EN 933-2:201 (EN 933-2:1995, IDT). The average dispersion of the σ phase particles was determined according to the formula [26]:

$$< d >= \frac{\sum_{i=1}^{n} m_i d_i}{\sum_{i=1}^{n} m_i}, \qquad (19)$$

where m_i is the mass of the i-th fraction of the powdered σ phase, kg, d_i is the arithmetic mean of dispersion of σ phase particles in the i-th fraction, $\times 10^{-6}$ m.

Depending on the size of the particles (dispersity), the powders are divided into groups. Dispersed FeCr intermetallide, in our case, is a mixture of powders of 2 incomplete groups [26]. Such groups are fine powder (10–40 μm) and medium-sized powder (40–250 μm).

In order to protect the surface of future castings from scorching, an anti-stick coating developed and prepared at PTIMA was used in this work. Anti-stick paint for the LFC process had the following chemical

TABLE 1. Chemical composition (% mass fraction) of the reinforcing phase before reinforcement.

Material	Alloying elements and impurities (Fe—base)							
	Al	Cu	Mn	Ni	Ti	Cr	Mo	W
Intermetallide	0.363	0.147	1.105	0.359	0.297	39.951	0.447	0.930

composition [27], % vol.: pyrophyllite (chemical formula $Al_2[Si_4O_{10}](OH)_2$) or disten-sillimanite (chemical formula $Al_2[SiO_4]O$) is 30.0–50.0, bentonite (60.0–70.0% wt.—montmorillonite, chemical formula $Al_2[Si_4O_{10}](OH)_2 \cdot nH_2O$)—10.0–20.0, acid dextrin (rational formula $(C_6H_{10}O_5)_n$) is 10.0–20.0, technical water (chemical formula H_2O) is the rest. To prevent the fermentation process in the warm season, sodium alginate (rational formula $C_6H_7O_6Na$) was added to the non-stick coating in the amount of 0.3 to 4.0% of the weight of the finished coating.

To obtain the cast samples, the G-CuZn15Si4 (DIN) cast brass was prepared. The studied material, the chemical composition of which (Table 2) is given below, was melted in a pot furnace for melting Cu and alloys based on it, such as brasses and bronzes, model 'CMT-01'. Technological parameters of the LFC process: a) matrix melt temperature, K: at the output from the melting unit—1523, during mold filling—1423, b) speed of mold filling, cm/s: experimental casting—7, control casting—5. The supply of liquid metal into the 'volume' of the CM was carried out from below into the sidewall of the CM along the thickness of the future cast sample (with the lower side siphon), which will be specified later in the text.

The study of the influence of melt inoculation of the G-CuZn15Si4 (DIN) cast brass on its microstructure, mechanical and tribotechnical characteristics was carried out according to the original method proposed by specialists of PTIMA and similar to that described in [6–9]. To do this, brass castings (Table 3, Fig. 3) were pre-marked and cut into templates, from which grindstones for metallographic analysis (MGA), samples for determination of hardness and wear resistance

TABLE 2. Chemical composition (% wt.) of the initial material.

Alloy brand (cast brass)	Alloying elements (Zn—base)									
	Fe	Si	Mn	Ni	P	Al	Cu	Pb	Sb	Sn
G-CuZn15Si4 (DIN)	0.53	4.18	0.75	0.17	0.89	0.04	80.0	0.42	0.91	0.26

TABLE 3. Concentration (% wt. fraction) of thermal dissociation products of FeCr intermetallide in the volume of the composite casting.

Investigated material	Chemical element	The height of the cast sample, $\times 10^{-3}$ m			
		0.015	0.045	0.075	0.105
Zero-dimensional CCM of Cu–FeCr system	Fe	0.980	1.000	1.000	1.010
	Cr	0.750	0.760	0.770	0.780

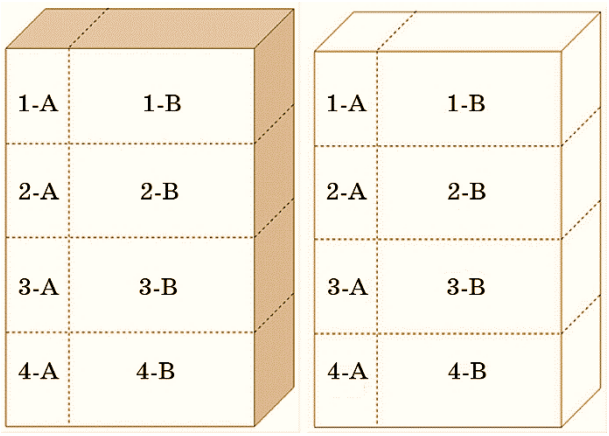

Fig. 3. Scheme of cutting castings into templates for studying the structure (1-A–4-A) and properties (1-B–4-B) of the material according to the height of the cast samples: zero-dimensional CCM of Cu–FeCr system (*a*), G-CuZn15Si4 (DIN) cast brass (*b*).

tests, as well as samples for determination of chemical composition were then made. The overall dimensions of the cast samples (see Fig. 3) were as follows, in mm: length is 50, width is 10, height is 120; and the overall dimensions of each template are 0.25 of the size of the test casting. Coordinates of the feeder (places where the matrix melt is fed into the CM 'volume'), mm: length is 50, width is 5, and height is 0.

The chemical composition of zero-dimensional CCM of the system Cu–FeCr was determined using the x-ray spectral microanalysis (XSM) method. The research was carried out with the help of a raster electron microscope-microanalyser РЭММА-102. The coefficient of assimilation of the σ phase by the melt of the G-CuZn15Si4 (DIN) cast brass can be determined from a ratio similar to the one proposed by the authors of [6]:

$$k_{\text{FeCr}} = \frac{[\text{FeCr}]_1 - [\text{FeCr}]_0}{C_{\text{FeCr}}^{\text{GM}}}, \qquad (20)$$

where $[\text{FeCr}]_1$, $[\text{FeCr}]_0$ are the concentrations of dispersed FeCr intermetallide in the matrix melt, respectively, after and before the inoculation process of the G-CuZn15Si4 (DIN) cast brass, % wt. fraction, $C_{\text{FeCr}}^{\text{GM}}$ is FeCr intermetallic content (from the mass of the cast sample) in the dispersed-filled, gasifying model, % wt. fraction.

However, XSM does not allow directly determining the concentration of the σ phase in the studied casting. In this case, the absorption coefficients of Fe and Cr can be taken separately as criteria for evaluating the efficiency of inoculation of the matrix brass melt with a dis-

persed intermetallic FeCr. In order to solve this problem, it is necessary to convert the content of the σ phase in DFGM into mass fractions, and then determine the concentration of each chemical element (% wt. fraction) that is part of the dispersed intermetallic FeCr. The mass fraction of a given element in a chemical compound, in general, can be calculated using the formula [28]:

$$\omega = 100\frac{nA_r}{M_r}, \tag{21}$$

where n is the number of atoms of an element in a chemical compound, A_r is the relative atomic mass of the element, M_r is the relative molecular weight of the substance.

The metallographic analysis of the material of the cast samples was carried out according to the recommendations of M. V. Maltsev [29]. The microstructure of the metallographic sections was etched using an acid-salt solution with the following chemical composition: 100 ml H_2O, 25 ml HCl, 10 g $FeCl_3$.

Mechanical tests of the materials that were the object of the study were carried out according to standard methods regulated by ГОСТ 1497-84, ГОСТ 9012-59, as well as ГОСТ 25.503-97. Testing of brass castings for wear under dry friction conditions in this work was carried out according to a non-standard method described by the authors of [30], which will be discussed later. The parameters of the process of testing brass castings for wear resistance were: test duration is 1800 s, the contact area of the sample-counterbody pair is 1 cm^2, counterbody rotation frequency is 480 rpm, linear speed of rotation of the counterbody is 1 m/s, normal reaction force of the support (loading) is of 5 kgf, friction path is of 1.8 km.

Cast samples worked in a pair with a counterbody, which had the shape of a hollow washer. Geometric dimensions of the counterbody, mm: outer diameter is 40, inner diameter is 16, and thickness is 12. As the MCB, structural low-chromium steel 41Cr4 (DIN) was used. The hardness of MCB according to the Rockwell scale, after its oil quenching and subsequent tempering [32], is in the range of 52–54 *HRC*. The testing of cast brass of the G-CuZn15Si4 (DIN) for wear resistance was carried out using a laboratory installation (friction machine) of the 'M22M' model, the schematic diagram of which is given in [33]. The change in the mass of the counterbody and cast samples was monitored by weighing them on analytical balances of the 'Radwag XAS 100/C' model.

The amount of wear of the zero-dimensional CCM of the system Cu–FeCr and the G-CuZn15Si4 (DIN) cast brass, as well as the wear of structural low-chromium steel 41Cr4 (DIN), was determined, practically, as the ratio of the mass loss of the material of the cast sample and the counterbody, respectively, to the product of the nominal contact area of the pair 'sample–counterbody' and friction paths [30, 31]:

$$I_q = \frac{\Delta m}{Sl}, \tag{22}$$

where Δm is the mass loss of the studied casting and counterbody, mg, S is the contact area of the sample-counterbody pair, cm^2, l is the friction distance, km.

The loss of material mass by both the cast sample and the counterbody, in turn, was determined using the empirical formula proposed by the authors of [30, 31, 33]:

$$\Delta m = m_1 - m_2, \tag{23}$$

where m_1, m_2 are the masses of the cast sample and counterbody before and after the test process, respectively, mg.

The research was carried out on 5 castings from the experimental alloy (the cast brass G-CuZn15Si4 (DIN) inoculated with 7% vol. fraction dispersed intermetallide FeCr) and 1 from the control (the cast brass G-CuZn15Si4 without additive). The research results were obtained by means of the mathematical processing of experimental data taken from each casting as an arithmetic mean. A cast sample from a control alloy (G-CuZn15Si4) and a test casting were subjected to MGA (G-CuZn15Si4 + FeCr), the properties of which were as close as possible to the arithmetic mean.

4. RESULTS AND DISCUSSION

For convenience and for the purpose of presenting the developed material in an accessible form, research on the inoculation process of the cast brass G-CuZn15Si4 (DIN) with dispersed intermetallic FeCr in the 'volume' of the CM according to the LFC process was carried out in stages. The results of the research showed that zero-dimensional CCM of the Cu–FeCr system has an optimal microstructure, high mechanical and tribotechnical properties, which will be discussed in detail later.

At the first stage, the dependence of Fe and Cr concentrations on the height of the cast sample was studied, and it was also clarified how and to what extent these parameters influence each other. The results of the presented experiment (Table 3) showed that in addition to the main components in the alloy under study.

G-CuZn15Si4 (DIN) + 7% vol. fraction FeCr such elements as Fe and Cr are also present. With the use of XSM, it was possible to establish that the concentrations of Fe and Cr (see Table 3) vary with the height of the composite casting. Graphical interpretation of experimental data is presented in Fig. 4. Visualization of the results of research (see Table 3) made it possible to find out that as the height of the cast sample increases, the concentrations of Fe and Cr in the zero-dimensional CCM of the

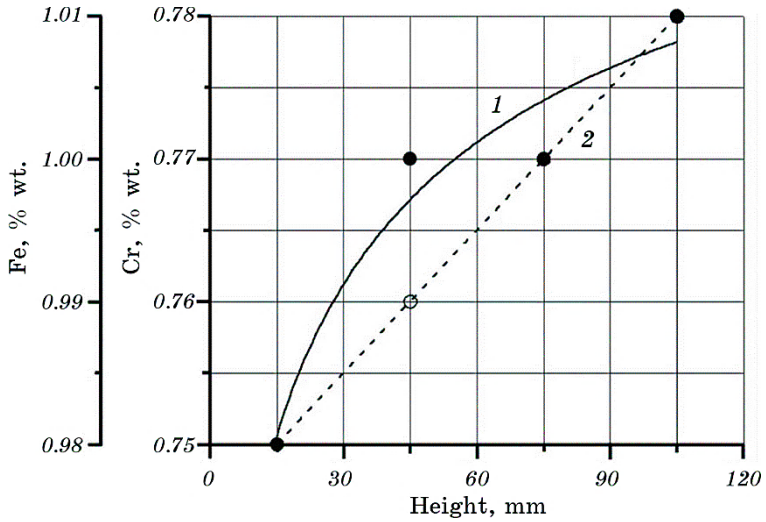

Fig. 4. Distribution of iron and chromium concentration along the height of the composite casting: *1* is iron concentration, *2* is chromium concentration.

system Cu–FeCr gradually increase. Therefore, for example, increasing the height of the composite casting from 15 mm to 105 mm leads to the fact that the concentration of Fe in the volume of the cast sample increases monotonically from 0.98% wt. fraction to 1.01% wt. fraction.

At the same time, the concentration of Cr in the G-CuZn15Si4 (DIN) cast brass after the inoculation process at 15 mm is 0.75% wt. fraction, while at a height of 105 mm this indicator reaches its maximum value and reaches 0.78% wt. fraction. The results of the experiment (see Table 3) and its graphical interpretation also showed that an increase in Cr concentration, which is part of the zero-dimensional CCM of the Cu–FeCr system, from 0.75% wt. fraction to 0.78% wt. fraction is the reason for the increase in Fe concentration in the composition of the composite casting from 0.98% wt. fraction to 1.01% wt. fraction. Since the temperature of the metal melt during mold filling significantly exceeds 1093 K, the σ phase turns into a solid solution of Cr in Fe [15], and in this case, obviously, a chemical reaction occurs:

$$[\mathrm{FeCr}] \xrightarrow{T} [\mathrm{Fe}] + [\mathrm{Cr}], \tag{24}$$

where T is the melting temperature of cast brass of the G-CuZn15Si4 (DIN), K, [Fe] and [Cr] are concentrations of iron and chromium in the matrix melt, respectively, % wt. fraction.

In order to predict, in the future, the influence of height of the cast sample on the concentrations of Fe and Cr in the composition of zero-dimensional CCM of the Cu–FeCr system (Fig. 4) and thus minimize

the volume of experimental work, the empirical equations of the corresponding trend lines were derived.

This also applies to the functional dependence (Fig. 5) of Fe concentration on Cr concentration. Such equations analytically describe the influence of independent factors on the characteristics of the test materials ($R^2 = 0.95–1.00$), which were mentioned above. Equations were obtained using computer technologies as a result of mathematical processing of experimental data (Table 3), given in tabular form, and they are given below:

$$[\mathrm{Fe}] = 9.36765 \cdot 10^{-1} - 4.75807 \cdot 10^{-5} H_{\mathrm{C}} + 1.64249 \cdot 10^{-2} \lg H_{\mathrm{C}}, \quad (25)$$

$$[\mathrm{Cr}] = 7.45 \cdot 10^{-1} + 3.33333 \cdot 10^{-4} H_{\mathrm{C}}, \quad (26)$$

$$[\mathrm{Fe}] = 37.6971 - 37.645[\mathrm{Cr}] + 29.4835 \lg[\mathrm{Cr}], \quad (27)$$

where H_{C} is the height of the brass casting, mm.

This type of dependence (Figs. 4, 5) is explained by the fact that [FeCr] depends on the height of the cast sample under the influence of circulation flows that take place in the volume of the metal bath. The nonlinear nature of these ratios indicates that [Fe] (Table 2) in the alloy of initial composition is imposed on the hydro- and gas dynamics of the LFC process. Since the σ phase in the alloys of the binary system Fe–Cr is formed near the ratio [Fe]:[Cr] = 1:1 [34], this is the nature of the functional connection between the concentration of Fe and the concentration of Cr (see Fig. 5) in the composition of the zero-dimensional

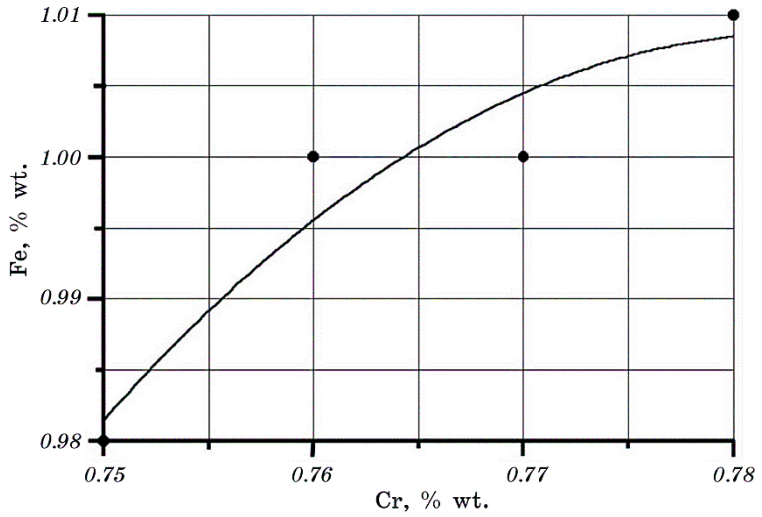

Fig. 5. Dependence of Fe concentration in the G-CuZn15Si4 (DIN) cast brass on the concentration of Cr in it.

CCM of the system Cu–FeCr 'speaks' in favour of the coefficient of assimilation of dispersed intermetallide FeCr and its thermal dissociation products (Eq. (24)) by the melt of the G-CuZn15Si4 (DIN) cast brass. Mathematical processing (Eqs. (20) 21)) of experimental data given in tabular form (Table 3) made it possible to find out that the coefficient of assimilation of dispersed intermetallide FeCr by the matrix melt, provided that the density of cast brass of the G-CuZn15Si4 (DIN) is 8500 kg/m^3 [23], the density of iron is 7874 kg/m^3 [35], and the density of chromium is 7180 kg/m^3 [36], the average is 0.397. The low coefficient of assimilation of the σ phase by the matrix melt can be explained by poor wetting of the powder by the molten G-CuZn15Si4 (DIN) cast brass and the lower supply of liquid metal into the 'volume' of the CM.

The second stage is dedicated to the study of microstructure (Fig. 6) of the control and composite castings. The results of MGA showed that the microstructure of the control casting (Fig. 6, *a*) is typical for the microstructure of the cast brass G-CuZn15Si4 (DIN).

The bright field of metallographic slides is α solid solution of a complex chemical composition and the light inclusions of an irregular outline are eutectoid α + γ. The basis of this eutectoid is the γ phase, *i.e.*, a chemical compound with a metallic Cu_5Si bond type, while the dark component is the α phase. The increased content of this eutectoid is explained by the imbalance of the considered alloys. MGA of composite casting (Fig. 6, *b*) made it possible to detect in the field of the metallographic section inclusions of the σ phase, which grind the structure of the base of the cast brass G-CuZn15Si4 (DIN), which is a sign of the microstructure of zero-dimensional CCM of the Cu–FeCr system. The darker, compared to the previous case, base of the cast sample indi-

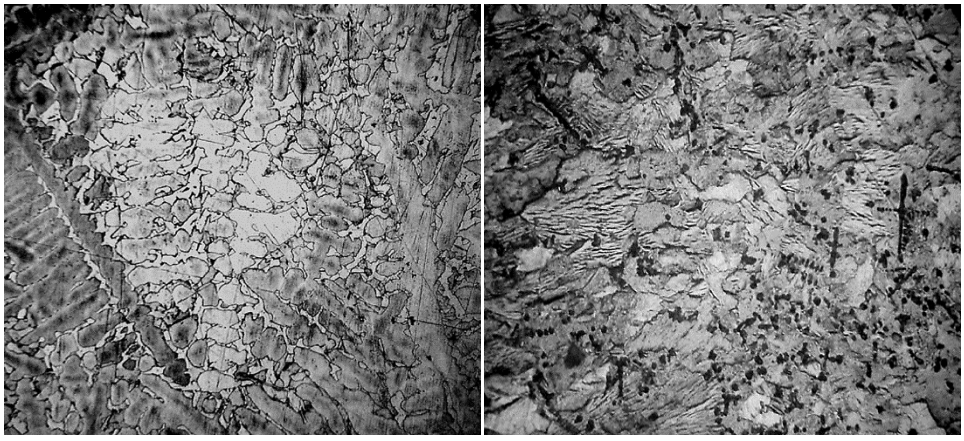

a *b*

Fig. 6. Microstructure (×100) of the material of cast samples: the cast brass G-CuZn15Si4 (DIN) (*a*), zero-dimensional CCM of the Cu–FeCr system (*b*).

cates its possible contamination by products of thermal dissociation of FeCr intermetallide.

At the third stage, the dependence of the hardness determined on the Brinell scale, of the control and composite castings on their height (Fig. 7), as well as Fe and Cr concentrations (Fig. 8) was studied. The results of the research (Table 4) showed that the hardness of brass castings varies not only with their height, but also depends on the concentration of Fe and Cr in the test material.

As a result of the graphical interpretation of experimental data (Fig. 7), it was possible to prove in practice that as the height of the cast samples increases from 15 mm to 105 mm, their hardness increases noticeably. So, for example, at the first horizon, that is, at a height of 15 mm, the hardness of the zero-dimensional CCM of the system Cu–FeCr, which was determined according to the Brinell scale, is 107.0 kgf/mm^2, while the hardness of the cast brass G-CuZn15Si4

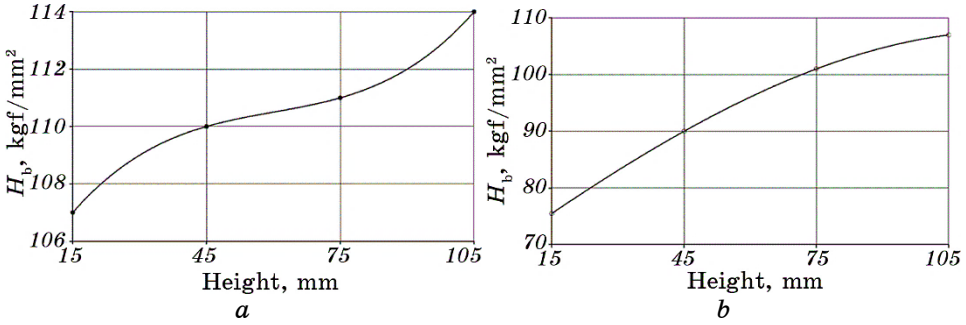

Fig. 7. Distribution of hardness of the test material along the height of the cast sample: zero-dimensional CCM of Cu–FeCr system (*a*), the cast brass G-CuZn15Si4 (DIN) (*b*).

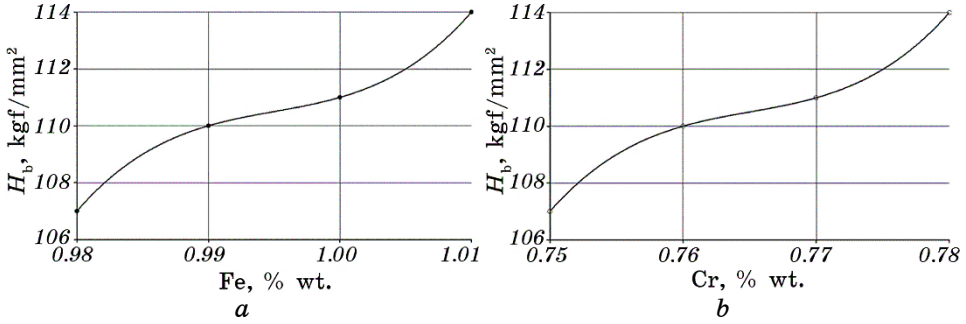

Fig. 8. The influence of the concentration of thermal dissociation products of the intermetallic reinforcing phase on the hardness on the Brinell scale of composite casting: Fe (*a*), Cr (*b*).

TABLE 4. Efficiency indicators of the process of inoculation of the cast brass G-CuZn15Si4 (DIN) with a dispersed FeCr intermetallic.

Position		Coordinates, mm				Thermal dissociation products of σ phase,% wt.		Hardness according to Brinell, kgf/mm²	Tribotechnical properties			
Casting material	Template index	Summary melt		Control point					$I_q \cdot 10^{-2}$ g/(cm²·km)	$I_{KT} \cdot 10^{-3}$ g/(cm²·km)	$i_q \cdot 10^{-6}$ g/(cm²·km·s)	Friction coefficient *f*
		H_B	a_B	H_B	a_B	Fe	Cr					
001	002	003	004	005	006	007	008	009	010	011	012	013
CCM of Cu–FeCr system	1-B	00	80	105	040	1.01	0.78	114.0	0.54	+3.40	03.000	0.3
	2-B			075		1.00	0.77	111.0	0.57	+3.60	03.167	0.4
	3-B			045		0.99	0.76	110.0	0.73	–0.56	04.056	0.6
	4-B			015		0.98	0.75	107.0	1.00	–3.10	05.556	0.7
The cast brass G-CuZn15Si4	1-B	00	80	105	040	–	–	107.0	1.00	–0.44	05.556	0.8
	2-B			075		–	–	101.0	1.74	–0.28	09.667	0.8
	3-B			045		–	–	090,0	1,90	–0.56	10.556	0.7
	4-B			015		–	–	075,5	2,84	–2.70	15.778	0.7

(DIN), under similar conditions, it is equivalent to 75.5 kgf/mm². The increase in the height of the cast samples contributes to the fact that its hardness gradually increases, and subsequently leads to the fact that on the forth horizon, *i.e.*, at a height of 105 mm, it is 114 kgf/mm² for the experimental alloy, and 107 kgf/mm² for control one.

Graphical interpretation of the results of experiment (Figure 8, *a*) also made it possible to find out that increasing of the concentration of Fe in the composite casting from 0.98% wt. fraction to 1.01% wt. fraction contributes to an increase in its hardness from 107 kgf/mm² to 114 kgf /mm². The same values (Fig. 8, *b*) acquires the hardness of samples of zero-dimensional CCM system Cu–FeCr at 0.75% wt. fraction Cr and 0.78% wt. fraction Cr, respectively.

Mathematical processing of experimental data (Table 4), which practically amounted to the approximation of the ratios of physical quantities given in tabular form, made it possible to derive a number of empirical equations that analytically describe the influence of height of the cast samples and the concentration of products of thermal dissociation of the σ phase, that is, Fe and Cr, on the hardness of the studied materials. These equations ($R^2 = 1$), which have the form of polynomials of the third order, are given below:

$$HB_{\text{Cu–FeCr}} = 2 \cdot 10^{-5} H_C^3 - 4.4 \cdot 10^{-3} H_C^2 + 2.944 \cdot 10^{-1} + 103.5, \quad (28)$$

$$HB_{\text{G-CuZn15Si4}} = 67.406 + 5.521 \cdot 10^{-1} H_C - 7 \cdot 10^{-4} H_C^{-2} - 9 \cdot 10^{-6} H_C^{-3}, \quad (29)$$

$$HB_{\text{Cu–FeCr}} = 666667[\text{Fe}]^3 - 2 \cdot 10^6[\text{Fe}]^2 + 2 \cdot 10^6[\text{Fe}] - 656689\,, \quad (30)$$

$$HB_{\text{Cu–FeCr}} = 666667[\text{Cr}]^3 - 2 \cdot 10^6[\text{Cr}]^2 + 10^6[\text{Cr}] - 298418\,. \quad (31)$$

This dependence of the hardness of zero-dimensional CCM of the Cu–FeCr system and the G-CuZn15Si4 (DIN) cast brass on the height of the test castings is explained by the fact that when the matrix melt is introduced from the bottom into the 'volume' of the CM, the density of the material increases from the bottom to the top, and therefore its hardness increases in the same direction. The influence of the concentration of thermal dissociation products of intermetallic AP (amorphous phase) on the hardness of the zero-dimensional CCM of the system Cu–FeCr is explained by the increase of its concentration also from the bottom to the top, and since the hardness of Fe and Cr exceeds the hardness of the binary system Cu–Zn, then the hardness of the cast samples under such conditions, in the end, increases.

The fourth stage of the research is dedicated to the study of the influence of height of the control and composite castings and the products of thermal dissociation of the σ phase on the tribotechnical properties of the G-CuZn15Si4 (DIN) cast brass and zero-dimensional CCM of the Cu–FeCr system. As in the previously discussed case, the results of the experiment showed (Table 4, Fig. 9) that the wear and rate of wear of cast samples, as well as the operation of MCB and the sliding friction coefficient of the 'casting–counterbody' pair depend, first of all, on the height of cast samples, concentrations of Fe and Cr, which are included in their composition. More details on this will be provided below.

Visualization of the results (Table 4) of the research carried out during the implementation of this investigation made it possible to find out (Fig. 9, *a*, *c*, *d*, *e*) that the tribotechnical characteristics of the composite casting improve as its height increases. The same can be said about the tribotechnical properties of the G-CuZn15Si4 (DIN) cast brass (Fig. 9, *b*, *d*, *e*, *g*), which, like the zero-dimensional CCM of the Cu–FeCr system, forms a sliding friction pair with structural low-chromium 41Cr4 (DIN) steel. It has been experimentally proven that in the interval from 15 mm to 105 mm the wear and wear rate of the composite casting decreases from $1.00 \cdot 10^{-2}$ g/(cm^2·km) and $5.556 \cdot 10^{-6}$ g/(cm^2·km·s) to $0.54 \cdot 10^{-2}$ g/(cm^2·km) and $3{,}000 \cdot 10^{-6}$ g/(cm^2·km·s), respectively. At the same time, at a height of 15 mm, the MCB activation and the sliding friction coefficient of the CCM system Cu–FeCr–41Cr4 (DIN) steel are, respectively, $3.1 \cdot 10^{-3}$ g/(cm^2·km) and wear rate is 0.7, while when at a height of 105 mm, the same indicators become $3.4 \cdot 10^{-3}$ g/(cm^2·km) and 0.3, respectively.

In addition, on the first horizon of the cast sample, which is 15 mm, the wear and wear rate of the control alloy, as well as the activation of the MCB and the coefficient of sliding friction of the G-CuZn15Si4 (DIN) cast brass–41Cr4 (DIN) steel, respectively, acquire the value of

$2.84 \cdot 10^{-2}$ g/(cm^2·km) and $15.778 \cdot 10^{-6}$ g/(cm^2·km·s), as well as $-2.70 \cdot 10^{-3}$ g/(cm^2·km) and wear rate is 0.7. A further increase in the height of the brass casting leads to the fact that already at the fourth horizon, equivalent to 105 mm, the same indicators change to $1.00 \cdot 10^{-2}$ g/(cm^2·km), $5.556 \cdot 10^{-6}$ g/(cm^2·km·s), $-0.44 \cdot 10^{-3}$ g/(cm^2·km) and wear rate is 0.8, respectively. The negative values of the coefficients of sliding friction of the 'cast sample–counterbody' pairs indicate that in the process of brass castings testing for wear under dry friction conditions, the base of the test materials adhered to the surface of the counterbody.

As a result of the approximation of the experiment results (Table 4), it was possible to derive a number of empirical equations that analytically describe the functional influence of the height of cast samples on the wear and wear rate of zero-dimensional CCM system Cu–FeCr and the G-CuZn15Si4 (DIN) cast brass, which form a sliding friction pair with the structural low-chromium 41Cr4 (DIN) steel, the triggering of MCB, which works in a pair with the zero-dimensional CCM of Cu–FeCr system and of the G-CuZn15Si4 (DIN) cast brass, the sliding fric-

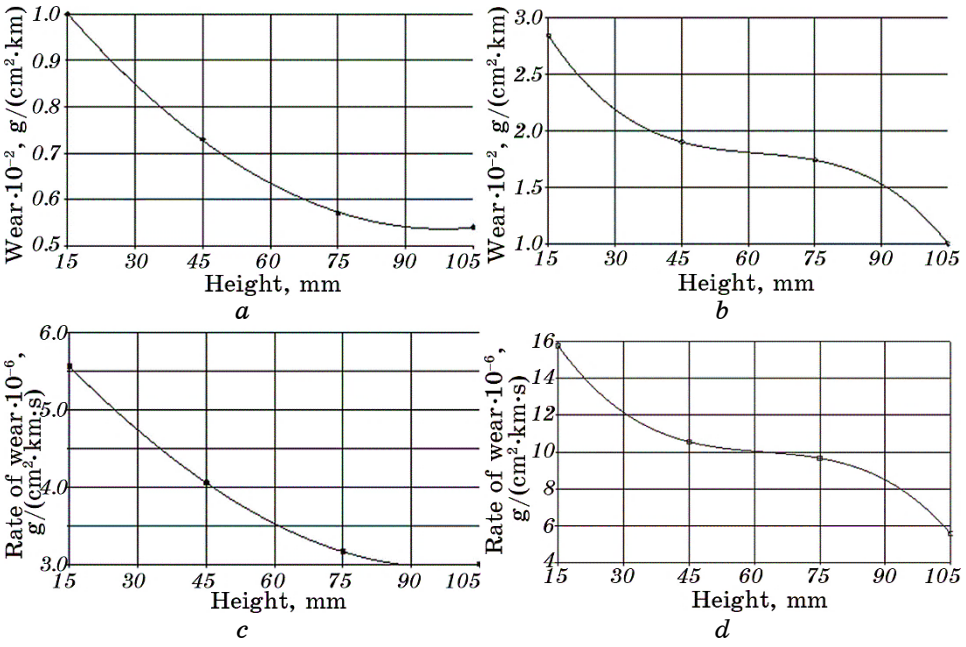

Fig. 9. Distribution of tribotechnical characteristics of zero-dimensional CCM of the system Cu–FeCr (*a*, *c*, *e*, *g*) and the G-CuZn15Si4 (DIN) cast brass (*b*, *d*, *f*, *h*) by the height of the cast samples: casting wear (*a*, *b*), the rate of wear of the cast sample (*c*, *d*), activation of the counterbody material (*e*, *f*), the sliding friction coefficient of the pair 'composite casting–counterbody', 'control casting–counterbody', respectively (*g*, *h*).

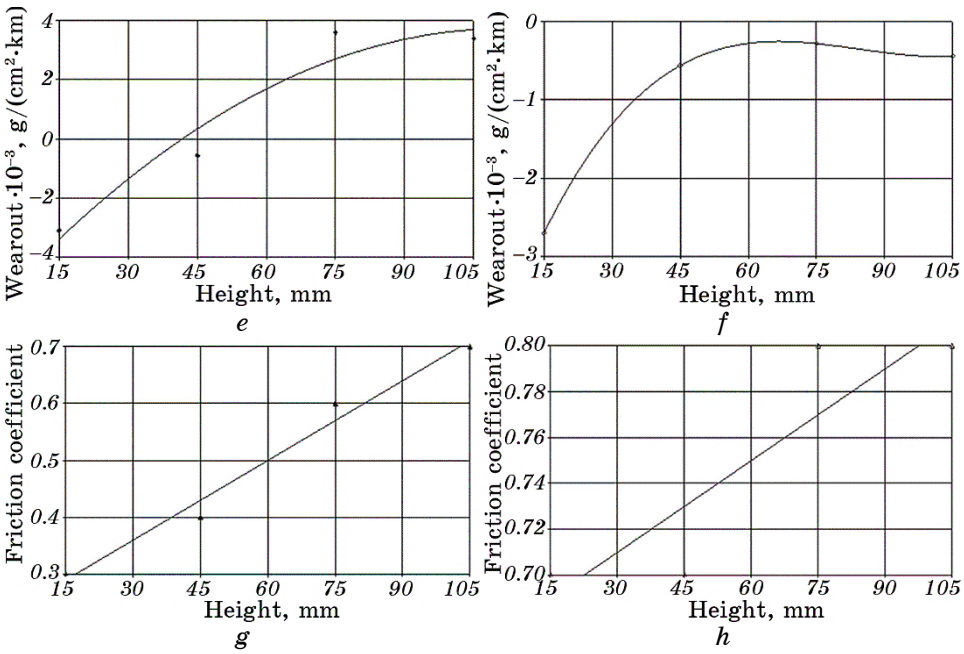

Continuation of Fig. 9.

tion coefficients of the pairs 'composite casting–counterbody' and 'control casting–counterbody', respectively. These equations (where I is wear, i is wear rate), in the form of polynomials of the second and third orders, as well as linear dependencies, are given below:

$$I^{41Cr4}_{q(Cu-FeCr)} = 7\cdot10^{-5}H_C^2 - 1.31\cdot10^{-2}H_C + 1.183, \quad (32)$$

$$I^{41Cr4}_{q(G\text{-}CuZn15Si4)} = 4.0275 - 1.008\cdot10^{-1}H_C + 1.6\cdot10^{-3}H_C^2 - 8\cdot10^{-6}H_C^3, \quad (33)$$

$$i^{41Cr4}_{q(Cu-FeCr)} = 7\cdot10^{-7}H_C^3 + 2\cdot10^{-4}H_C^2 - 6.68\cdot10^{-2}H_C + 6.5004, \quad (34)$$

$$i^{41Cr4}_{G\text{-}CuZn15Si4} = 22.375 - 5.598\cdot10^{-1}H_C + 8.7\cdot10^{-3}H_C^2 - 5\cdot10^{-5}H_C^3, \quad (35)$$

$$I^{Cu-FeCr}_{CB(40X)} = -8\cdot10^{-4}H_C^2 + 1.702\cdot10^{-1}H_C - 5.7807, \quad (36)$$

$$I^{G\text{-}CuZn15Si4}_{CB(41Cr4)} = 9\cdot10^{-6}H_C^3 - 2.2\cdot10^{-3}H_C^2 + 1.787\cdot10^{-1}H_C - 4.9113, \quad (37)$$

$$f^{41Cr4}_{Cu-FeCr} = 4.7\cdot10^{-3}H_C + 2.2\cdot10^{-1}, \quad (38)$$

$$f^{41Cr4}_{G\text{-}CuZn15Si4} = 1.3\cdot10^{-3}H_C + 6.7\cdot10^{-1}. \quad (39)$$

Therefore, the reliability values of the approximation of mathematical expressions presented above are sufficient and, for each ratio, are as follow: $R^2 = 0.9998$, $R^2 = 1$, $R^2 = 1$, $R^2 = 1$, $R^2 = 0.9435$, $R^2 = 1$, $R^2 = 0.98$, $R^2 = 0.8$, respectively. This certainly indicates the fact that

the discrepancies between the functional dependencies given in the Table 4 and the corresponding equations of the trend lines (32)–(39) are minimal.

This type of dependences (Fig. 9, Eqs. (32)–(39)) can be explained by the structural heterogeneity of the material of cast samples. Since it was previously proven that there is a functional relationship between the concentration of Fe, Cr and the height of the casting under test (Figs. 4, 5, Eqs. (25)–(27)), it can be asserted with a high degree of probability that on the tribotechnical properties of zero-dimensional CCM of Cu–FeCr system and of the G-CuZn15Si4 (DIN) cast brass are influenced by the concentrations of Fe and Cr. However, this is the subject of especial studies, and it will be discussed further.

The results of the proposed experiment (Table 4), when performing the research task and their graphic interpretation (Fig. 10), confirmed the assumption made above. According to this assumption, the concentration of the products of thermal σ phase dissociation determines the tribotechnical characteristics of the composite and control castings. Such products are Fe and Cr.

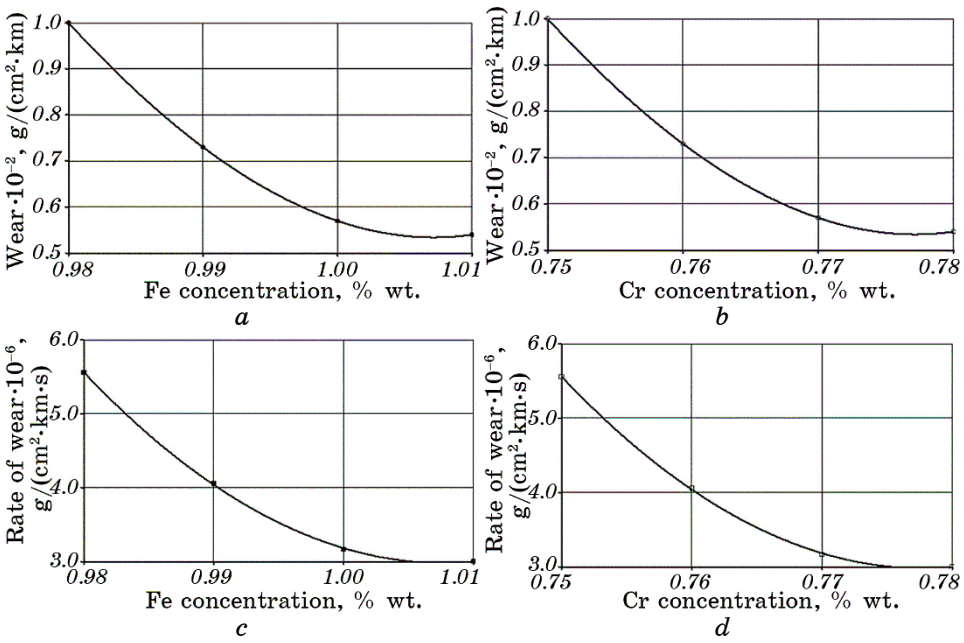

Fig. 10. Dependence of the tribotechnical properties of the zero-dimensional CCM Cu–FeCr system on the concentration of iron (*a*, *c*, *e*, *g*) and chromium (*b*, *d*, *f*, *h*) in the volume of cast samples: wear of the composite casting (*a*, *b*), wear rates of the cast sample (*c*, *d*), activation of the counterbody material (*e*, *f*), the friction coefficient of the sliding pair 'composite casting–counterbody' (*g*, *h*).

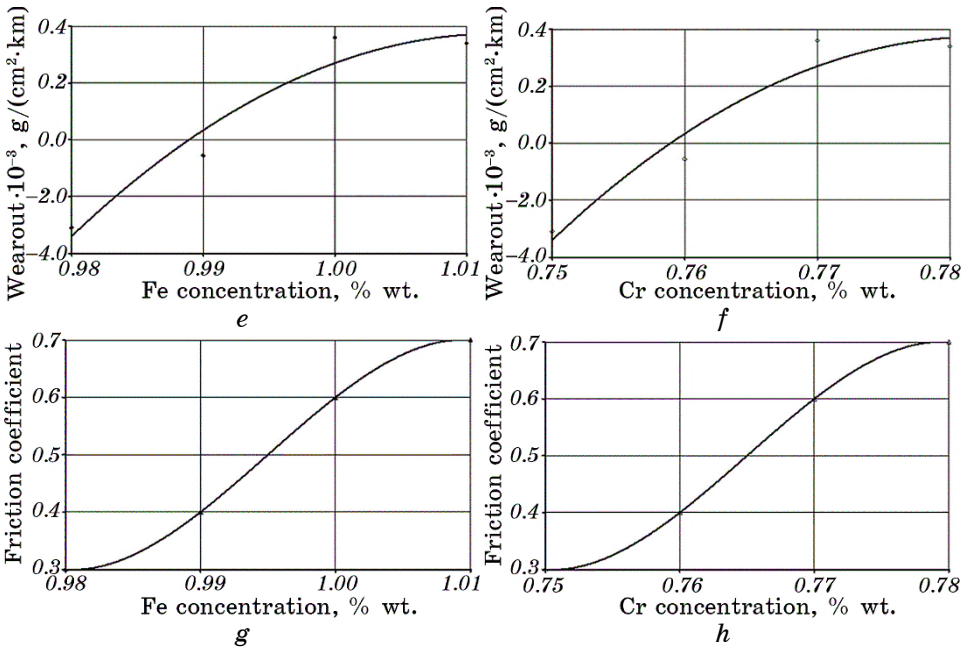

Continuation of Fig. 10.

In particular, it was established that increasing of the Fe and Cr concentrations in the cast sample has the same effect as the height on the tribotechnical properties of zero-dimensional CCM Cu–FeCr system (Fig. 9, *a*, *c*, *d*, *e*) composite casting. Since the coordinates of control points, concentrations of products of the σ phase thermal dissociation, mechanical characteristics and tribotechnical properties of the cast sample (Table 4) are linked by the indices of the corresponding templates (Table 4, Fig. 3), then the need for in-depth analysis of graphical interpretation of experimental data (Fig. 10) is currently eliminated. The truth of this statement is also proved by the graphic interpretation of research results (Fig. 4), considered and analysed earlier, which, through the scheme of marking and cutting composite castings into templates (Fig. 3), indirectly demonstrates a functional connection with the tribotechnical characteristics of zero-dimensional CCM system Cu–FeCr.

In order to predict, in the future, the dependence of the tribotechnical properties of a composite casting on the concentrations of Fe and Cr in its composition, it is necessary to approximate the ratios of physical quantities (Table 4) given in tabular form. Empirical equations (polynomials of the second and third orders), which with a sufficient value of approximation reliability ($R^2 = 1$, $R^2 = 1$, $R^2 = 0.9998$, $R^2 = 0.9998$, $R^2 = 0.9435$, $R^2 = 0.9435$, $R^2 = 1$, $R^2 = 1$, respectively) were

obtained as a result of mathematical processing of experimental data (Table 4), given below:

$$I^{41Cr4}_{q(Cu-FeCr)} = 3333.3[Fe]^3 - 9350[Fe]^2 + 8690.2[Fe] - 2672.9, \quad (40)$$

$$I^{41Cr4}_{q(Cu-FeCr)} = 3333.3[Cr]^3 - 7050[Cr]^2 + 4918.2[Cr] - 1128.2, \quad (41)$$

$$i^{41Cr4}_{q(Cu-FeCr)} = 3332.5[Fe]^2 - 6717.2[Fe] + 3387.9, \quad (42)$$

$$i^{41Cr4}_{q(Cu-FeCr)} = 3332.5[Cr]^2 - 5184.3[Cr] + 2019.3, \quad (43)$$

$$I^{Cu-FeCr}_{CB(40Cr4)} = -6850[Fe]^2 + 13868[Fe] - 7015.4, \quad (44)$$

$$I^{Cu-FeCr}_{CB(41Cr4)} = -6850[Cr]^2 + 10717[Cr] - 4188.1, \quad (45)$$

$$f^{41Cr4}_{Cu-FeCr} = -33333[Fe]^3 + 99500[Fe]^2 - 98982[Fe] + 32816, \quad (46)$$

$$f^{41Cr4}_{Cu-FeCr} = -33333[Cr]^3 + 76500[Cr]^2 - 58502[Cr] + 14908. \quad (47)$$

The dependence of the tribotechnical characteristics of cast sample on the concentrations of Fe and Cr in its volume is explained by the fact that the hardness and wear resistance of these components significantly exceeds the hardness of the Me-matrix of zero-dimensional CCM Cu–FeCr system. Therefore, increasing the concentrations of Fe and Cr contributes to the reduction of wear and the rate of wear of the composite casting, as well as to the increase of triggering of the MCB and the coefficient of friction sliding of the 'CCM Cu–FeCr system–41Cr4 (DIN) steel'.

5. CONCLUSIONS

During the implementation of this investigation, valuable scientific, technical and practical results were obtained and, in this way, the effectiveness of inoculation of the melt of G-CuZn15Si4 (DIN) cast brass grade with dispersed intermetallic FeCr in the 'cavity' of the CM according to the LFC process was proven. The results of research made it possible to reach certain conclusions and find out that.

1. The assimilation coefficient of dispersed intermetallide FeCr by the matrix melt is 0.397, which is quite acceptable when performing the given task.
2. Composite castings have an optimal microstructure, which is characteristic of zero-dimensional CCM system Cu–FeCr.
3. The hardness of composite castings, determined according to the Brinell scale, on average, is 18.3% higher than the similar value of the G-CuZn15Si4 (DIN) cast brass.
4. The wear and wear rate of the zero-dimensional CCM Cu–FeCr system, on average, is on 62.0% lower than the same characteristics of the control casting, and the sliding friction coefficient of the 'CCM Cu–FeCr system–41Cr4 (DIN) steel' according to average value, on 33.3%

inferior to the similar value of the pair 'the G-CuZn15Si4 (DIN) cast brass–41Cr4 (DIN) steel'; activation of the MCB, which forms a pair of sliding friction with the G-CuZn15Si4 (DIN) cast brass, is on 183.9% lower than the triggering of the MCB, which works in a pair with a zero-dimensional CCM of Cu–FeCr system.

REFERENCES

1. V. A. Pavlov, *Penopolistirol* [Polistirene Foam] (Moskva: Khimiya: 1973) (in Russian).
2. V. S. Shulyak, *Lit'yo po Gazifitsiruyemym Modelyam* [Casting on Gasifying Models] (Saint Petersburg: NPO 'Professional': 2007) (in Russian).
3. O. I. Shinskiy, V. V. Sumenkova, and V. P. Vishniakova, *Casting Processes*, No. 2: 51 (2002) (in Russian).
4. G. F. Balandin, *Osnovy Teorii Formirovaniya Otlivki: Formirovanie Makroskopicheskogo Stroyeniya Otlivki* [Fundamentals of the Theory of Casting Formation: Formation of the Macroscopic Structure of the Casting] (Moskva: Mashinostroenie: 1979) (in Russian).
5. I. A. Nebozhak, V. G. Novytskyy, and O. I. Shynsky, *Casting Processes*, No. 5: 50 (2008) (in Russian).
6. I. A. Nebozhak, V. V. Sumenkova, I. V. Tkachuk, and O. I. Shynsky, *Metal Sci. Treatment Metals*, No. 4: 43 (2001) (in Ukrainian).
7. I. A. Nebozhak and O. V. Derev'yanko, *Metal ta Lyttya Ukrayiny*, **29**, No. 1: 70 (2021) (in Ukrainian).
8. I. A. Nebozhak, O. V. Derev'yanko, A. M. Verkhovlyuk, D. S. Kanibolots'kyy, and V. H. Novyts'kyy, *Metal ta Lyttya Ukrayiny*, **31**, No. 2: 51 (2023) (in Ukrainian).
9. I. A. Nebozhak, V. H. Novyts'kyy, O. V. Derev'yanko, D. S. Kanibolots'kyy, and A. M. Verkhovlyuk, *Metal ta Lyttya Ukrayiny*, **31**, No. 3: 8 (2023) (in Ukrainian).
10. V. A. Ozerov, V. S. Shuliak, and G. A. Plotnikov, *Lit'yo po Modelyam iz Penopolistirola* [Casting from Polystyrene Foam Models] (Moskva: Mashinostroenie: 1969) (in Russian).
11. Yu. A. Stepanov, *Lit'yo po Gazifitsiruyemym Modelyam* [Casting Using Gasified Models] (Moskva: Mashinostroenie: 1976) (in Russian).
12. V. S. Shuliak, S. A. Rybnikov, and K. A. Grigorian, *Proizvodstvo Otlivok po Gazifitsiruyemym Modelyam* [Production of Castings Using Gasified Models] (Moscow: MGIU: 2001) (in Russian).
13. Yu. A. Stepanov and V. G. Moskalyov, *Casting Processes*, No. 7: 1 (1972) (in Russian).
14. B. M. Yavorskiy and A. A. Detlaf, *Spravochnik po Fizike* [Physics Handbook] (Moskva: Nauka: 1985) (in Russian).
15. O. I. Shinskiy and V. S. Shulyak, Lit'yo po gazifitsiruyemym modelyam [Casting on Gasifying Models] (Kiev: Znaniye: 1979) (in Russian).
16. I. A. Nebozhak, O. V. Derev'yanko, A. M. Verkhovlyuk, and D. S. Kanibolots'kyy, *Metal ta Lyttya Ukrayiny*, **30**, No. 4: 36 (2022) (in Ukrainian).
17. D. I. Garkonov, *Tribotekhnika* [Tribotechnics] (Moskva: Mashinostroenie:

1985) (in Russian).
18. *Koehfitsient Tertya* [Friction Coefficient] (Wikipedia: 2023) (in Ukrainian).
19. M. V. Kindrachuk and E. A. Kul'havyy, *Proc. National Aviation University*, No. 4: 67 (2005) (in Ukrainian).
20. *Mekhanichni Vlastyvosti Materialiv* [Mechanical Properties of Materials] (Wikipedia: 2023) (in Ukrainian).
21. M. V. Kindrachuk, E. A. Kul'havyy, D. I. Perro, and V. O. Podlyesnyy, *Proc. National Aviation University*, **4**, No. 4: 32 (2009) (in Ukrainian).
22. M. V. Kindrachuk, E. A. Kul'havyy, O. L. Shevchenko, and A. P. Danilov, *Proc. National Aviation University*, **1**, No. 1: 102 (2009) (in Ukrainian).
23. *Tsvetnoye Lit'yo* [Colour Casting] (Ed. N. M. Galdin) (Moskva: Mashinostroenie: 1989) (in Russian).
24. O. I. Shynsky, L. P. Vyshnyakova, V. N. Plotnikova, and Ye. F. Knyazev, *Sposib Vyhotovlennya Modeley iz Polistyrolu* [Method for Producing Models from Polystyrene Foam], Patent of Ukraine No. 3493216 (Published 1993) (in Ukrainian).
25. A. Wittmoser and J. Schade, *Verfahren zur Herstellung von Gußstücken unter Verwandung Vergasbaren Modelle*, German Patent No. 114482 (in German).
26. *Vlastyvosti Metalevykh Poroshkiv* [The Properties of Metal Powders].
27. O. I. Shynsky, I. O. Shynsky, and Yu. A. Goncharenko, *Protypryharne Pokrytya dlya Lyttya za Modelyamy, shcho Hazyfikuyut'sya* [Non-Stick Coating for Casting by Gasified Models], Patent of Ukraine No. 58824 (Published 2003) (in Ukrainian).
28. *Masova Chastka Elementa* [Mass Fraction of an Element] (Wikipedia: 2023) (in Ukrainian).
29. M. V. Mal'tsev, *Metallografiya Promyshlennykh Tsvetnykh Metallov i Splavov* [Metallography of Industrial Colour Metals and Alloys] (Moskva: Metallurgiya: 1970) (in Russian).
30. L. I. Kuksenova, V. G. Lapteva, A. G. Kolmakov, and L. M. Rybakova, *Metody Ispytaniy na Trenie i Iznos* [Friction and Wear Test Methods] (Moskva: Intermet Inzhiniring: 2001) (in Russian).
31. I. V. Kragelskiy, M. N. Dobychin, and V. S. Kombalov, *Osnovy Raschyotov na Trenie i Iznos* [Basics of Friction and Wear Calculations] (Moskva: Mashinostroenie: 1977) (in Russian).
32. F. I. Maslennikov, *Laboratornyi Praktikum po Metallovedeniyu* [Laboratory Workshop on Metal Science] (Moskva: Mashgiz: 1961) (in Russian).
33. V. P. Gavrilyuk and V. G. Novitskiy, *Metodika Opredeleniya Iznosostoykosti Materialov v Usloviyakh Treniya Skol'zheniya na Mashine Treniya M22M* [Methodology for Determining the Wear Resistance of Materials under Conditions of Sliding Friction on a Friction Machine M22M] (Kyiv: PTIMA: 2002) (in Russian).
34. A. P. Gulyayev, *Metallovedenie* [Metal Science] (Moskva: Metallurgiya: 1977) (in Russian).
35. *Hustyna Zaliza* [Density of Iron] (Wikipedia: 2023).
36. *Khrom* [Chromium] (Wikipedia: 2023).
37. *Sigma phases*.

Metallophysics and Advanced Technologies
Металофіз. новітні технол.
Metallofiz. Noveishie Tekhnol.
2024, vol. 46, No. 5, pp. 415–429
https://doi.org/10.15407/mfint.46.05.0415
Reprints available directly from the publisher

PACS numbers: 06.60.Vz, 64.70.dj, 68.37.Hk, 81.20.Vj, 81.30.Bx, 81.30.Fb, 81.40.Wx

Визначення структур литого металу та зварного з'єднання після електронно-променевого зварювання інтерметалідного титанового стопу Ti–28Al–7Nb–2Mo–2Cr, одержаного методою електронно-променевого топлення

С. В. Ахонін, А. Ю. Северин, В. Ю. Білоус, В. А. Костін, В. О. Березос

Інститут електрозварювання ім. Є. О. Патона НАН України,
вул. Казимира Малевича, 11,
03150 Київ, Україна

Проведено дослідження структури основного металу та металу шва після електронно-променевого зварювання (ЕПЗ) інтерметалідного титанового стопу Ti–28Al–7Nb–2Mo–2Cr (ваг.%), одержаного методою електронно-променевого перетоплення (ЕПП). Макроструктура виливка ЕПП стопу Ti–28Al–7Nb–2Mo–2Cr характеризується зернами, близькими до рівновісних з величиною зерна у 8–9 балів. Показано, що мікроструктура литого металу стопу Ti–28Al–7Nb–2Mo–2Cr складається з матричної світлої γ-фази, що чергується з ділянками двофазної ($\gamma + \alpha_2$)-лямельної структури розміром до 50 мкм, з товщиною лямелей близько 1 мкм, та впорядкованої β-фази, яка утворює сітчастий візерунок на тлі матриці. Встановлено, що внутрішньозеренна структура металу зварного з'єднання після ЕПЗ з локальним термічним обробленням (ЛТО) відрізняється від структури основного металу та складається з невеликих (до 20 мкм) ділянок з ($\gamma + \alpha_2$)-лямельною структурою на тлі світлої матричної γ-фази із сіткою з витягнутих частинок довжиною у 30–80 мкм і товщиною у 1–3 мкм.

Ключові слова: інтерметалідний титановий стоп, структура, фаза , електронно-променеве топлення, електронно-променеве зварювання.

Corresponding author: Andrii Yuriievych Severyn
E-mail: tim.severin72@gmail.com

E. O. Paton Electric Welding Institute, N.A.S. of Ukraine,
11 Kazymyr Malevych Str., UA-03150 Kyiv, Ukraine

Citation: S. V. Akhonin, A. Yu. Severyn, V. Yu. Belous, V. A. Kostin, and V. O. Berezos, Determination of Cast-Metal Structures and Welded Joints After Electron-Beam Welding of the Intermetallic Titanium Alloys Ti–28Al–7Nb–2Mo–2Cr Obtained by Electron-Beam Melting Method, *Metallofiz. Noveishie Tekhnol.*, **46**, No. 5: 415–429 (2024) (in Ukrainian). DOI: 10.15407/mfint.46.05.0415

The structure of the base metal and weld metal after electron-beam welding (EBW) of the intermetallic titanium alloy Ti–28Al–7Nb–2Mo–2Cr (wt.%) obtained by the electron-beam melting method is studied. The macrostructure of the Ti–28Al–7Nb–2Mo–2Cr alloy ingot is characterized by grains close to equiaxed with a grain size of 8–9 points. As shown, the microstructure of the cast metal of the Ti–28Al–7Nb–2Mo–2Cr alloy consists of a matrix bright γ-phase alternating with sections of a two-phase ($\gamma + \alpha_2$) lamellar structure up to 50 μm in size, with a lamellae thickness of about 1 μm, and of the ordered β-phase, which forms a mesh pattern against the background of the matrix. As established, the intragranular structure of the metal of the welded joint after EBW with local heat treatment (LHT) differs from the structure of the base metal and consists of small (up to 20 μm) areas with a ($\gamma + \alpha_2$) lamellar structure against the background of a light matrix γ-phase with a network of elongated particles of 30–80 μm long and 1–3 μm thick.

Key words: intermetallic titanium alloy, structure, phase, electron-beam melting, electron-beam welding.

(Отримано 17 жовтня 2023 р.; остаточн. варіянт — 28 листопада 2023 р.)

1. ВСТУП

В Україні, в умовах воєнного стану, наразі виникає велика потреба в одержанні та застосуванні нового класу матеріялів для авіаційного й енергетичного машинобудування. В даний час до числа найбільш перспективних матеріялів для двигунобудівної области промисловости відносяться інтерметалідні стопи на основі системи Ti–Al з робочими температурами вище 650°C, що мають високі показники жароміцних властивостей. Використання стопів на основі інтерметалідів титану для виготовлення лопаток турбін, а також деталів гарячого газового тракту (камери згорання, дифузори, вихлопні системи) газотурбінних двигунів (ГТД) авіаційного й іншого призначень дасть змогу підвищити робочу температуру ГТД на 100–150°C, зменшити вагу двигуна на 20–40%, підвищити ресурс двигуна у 2–3 рази. На теперішній час на підприємствах України (ПАТ «Мотор Січ», ДП НВКГ «Зоря»–«Машпроект») освоєно виробництво лопаток газотурбінних двигунів з титанових стопів методами фасонного лиття у вакуумно-дугових печах і штампування. Це ж обладнання може бути використане для виробництва виробів із алюмінідів титану. Але в ливарних вакуумно-дугових печах різних типів діяметер витратної електроди складає від 200 до 350 мм, що зумовлює можливість створення виробництва виливків-заготівок з інтерметалідів на основі алюмініду титану. На відміну від звичайних жароміцних титанових стопів, сучасні інтерметалідні титанові стопи мають підвищений вміст Алюмінію та Ніобію, що викликає певні труднощі, пов'язані з великим вмістом крихкої

складової шихти, які можуть призвести до обриву електрод під час вакуумно-дугового перетоплення (ВДП) і формування неоднорідного хемічного складу зливка. Також в Україні відсутні потужності для одержання якісних електрод великого діяметра методом ВДП, але є можливість задіяти для цих цілей установки електронно-променевого перетоплення (ЕПП). Для виробництва деталів з алюмінідів титану методами штампування та прокатування також необхідні крупногабаритні виливки. Так, наприклад, на ДП «КБ «Південне» планують використовувати у виробництві БПЛА листи з інтерметалідів Ti–Al розмірами до 1,5×3500×6000 мм, а необхідна маса заготовок для одержання листів такого сортаменту складає 200–400 кг.

Електронно-променеве зварювання (ЕПЗ) широко застосовується для виробництва конструкцій з леґованих титанових стопів. В даний час це — найбільш поширений метод одержання зварних з'єднань жароміцних стопів на основі алюмініду титану.

Вищезазначене зумовлює нагальну потребу в створенні інтерметалідних стопів системи титан–алюміній з найліпшим поєднанням властивостей, розробці технології одержання виливків цих інтерметалідних стопів і розробці технології зварювання цих матеріялів.

2. АНАЛІЗА ЛІТЕРАТУРНИХ ДАНИХ І ПОСТАНОВКА ПРОБЛЕМИ

Інтерметаліди — клас легких, жароміцних і жаростійких матеріялів, які призначені для роботи в різних конструкціях за температур у 600–900°C [1, 2]. Промислові жароміцні титанові стопи мають робочу температуру не вище 600°C (ВТ18У, ВТ-25, TIMETAL1100, TIMETAL-15-3, IMI 834), оскільки за більш високих температур в титанових стопах розвиваються характерні для них процеси міжзеренного руйнування, що призводить до різкого погіршення властивостей. В роботах [3, 4] показано, що інтерметалід TiAl вигідно відрізняється від інших сполук тим, що його межа плинности зростає з підвищенням температури до 600–800°C. Сильні ковалентні зв'язки між атомами інтерметаліду TiAl забезпечують підвищення енергії активації дифузії, що уповільнює розвиток процесів плазучости за температур до 900°C і забезпечує високу жорсткість в широкому інтервалі температур. Однак інтерметалід TiAl дуже сильно поступається промисловим суперстопам за пластичністю, але перевершує кераміки за характеристиками низькотемпературної пластичности, в'язкости руйнування й опору термоудару, має більш високу теплопровідність і кращу технологічність, ніж кераміка [5].

Топлення інтерметалідних титанових стопів пов'язане з певними технологічними труднощами через велику кількість Алюмінію, що входить до складу стопу, та його високу летючість у вакуумі, знач-

ну ріжницю в температурах топлення титану й алюмінію, високу хемічну активність розтопу, необхідність одержати гомогенний розтоп. Стопи на основі алюмініду титану мають малий інтервал кристалізації та мають гарні ливарні властивості [6, 7]. Виливки алюмініду титану або розтоп рідкого металу для подальшої заливки у форму одержують тими ж способами, що і промислові титанові стопи. В даний час основною методою одержання виливків жароміцних стопів титану є вакуумно-дугове перетоплення (ВДП). Але в роботах [8, 9] доведено, що технологія ВДП не дає змоги вирішити одну з найважливіших проблем якости матеріялу, який використовуються в деталях відповідального призначення, а саме, ґарантувати відсутність в ньому дефектів у вигляді включень з низькою щільністю (так звані тверді α-включення) та тяжкотопких включень з високою щільністю. А в роботі [10] припускається, що нерівномірний розподіл леґувальних елементів у титанових стопах, одержаних методою ВДП, призводить до руйнування виробів. Але в роботах [11–13] доведено, що технологія ЕПП уможливлює уникнути цих недоліків. У підсумку: доцільним є проведення експериментів з одержання жароміцних інтерметалідних титанових стопів саме методою ЕПП й дослідження якости та властивостей одержаних виливків.

Однією з причин, що обмежує використання алюмінідів титану, є їхня низька технологічність, у тому числі складність зварювання, зумовлена надзвичайно низькою пластичністю, високою чутливістю до напружень у зварному з'єднанні, які з'являються в умовах нерівномірного нагріву з'єднання під час зварювання, що в свою чергу, призводить до утворення поперечних і поздовжніх тріщин у зварному з'єднанні [14]. Процес електронно-променевого зварювання має істотні переваги під час зварювання стопів на основі алюмінідів титану: універсальність, гнучкість, висока питома погонна енергія та швидкість зварювання, а також надійний захист зони зварювання та можливість здійснювати локальне термічне оброблення у вакуумній камері, що дає змогу одержувати зварні з'єднання найвищої якости [15, 16]. Параметри процесу електронно-променевого зварювання та локального термічного оброблення можуть забезпечити формування сприятливої $(\gamma + \alpha_2)$-структури у металі зварного шва [17]. Для пониження ймовірности появи у зварних з'єднаннях алюмінідів титану тріщин під час зварювання топленням необхідний попередній підігрів з'єднань, що зварюються до значних температур (у 200–500°C). В роботах [18, 19] проаналізовано розвиток пружньо-пластичних деформацій під час зварювального нагрівання й охолодження зразків на основі алюмінідів титану. Тому доцільно оцінити вплив зварювання із застосуванням попереднього підігріву та локального термічного оброблення на структуру з'єднань зі стопу на основі алюмініду титану.

3. МЕТА ТА ЗАДАЧІ ДОСЛІДЖЕННЯ

Метою дослідження є визначення структури литого металу та визначення структурно-фазових перетворень під час проведення ЕПЗ в металі зварного з'єднання інтерметалідного титанового стопу, одержаного методою ЕПП, що дасть можливість показати перспективу застосування ЕПП для одержання якісних виливків і використання ЕПЗ для можливости зварювання складнолеґованого інтерметалідного стопу.

Для досягнення поставленої мети потрібно вирішити наступні задачі:

– одержати методою ЕПП бездефектний інтерметалідний титановий стоп;

– дослідити структуру та хемічний склад фазових складових одержаного металу ЕПП;

– дослідити структуру металу зварного з'єднання інтерметалідного титанового стопу, одержаного методою електронно-променевого топлення після електронно-променевого зварювання.

4. МАТЕРІЯЛИ ТА МЕТОДИ ДОСЛІДЖЕНЬ

В якості вихідних шихтових матеріялів використовувалися титан, ніобій, молібден і хром у чистому вигляді й алюміній марки А7 у вигляді чушок. Елементи з високою пружністю пари додавали з урахуванням втрат їх на випаровування.

Виливки інтерметалідного стопу Ti–28Al–7Nb–2Mo–2Cr (ваг.%) одержували за розробленою в ІЕЗ ім. Є. О. Патона НАН України технологією електронно-променевого топлення з проміжною місткістю [12, 13]. Дослідні топлення проводили на електронно-променевій установці УЕ-121, оснащеній 3 електронно-променевими гарматами «Патон 300» (Україна) потужністю у 300 кВт кожна. Процес топлення здійснювали у вакуумі 0,1–0,01 Па, що створювало найбільш сприятливі умови для видалення Гідроґену з металу й унеможливлювало забруднення титану Нітроґеном і Оксиґеном.

Для аналізи вмісту леґувальних елементів у виливках одержаних стопів використовувався метод оптичної емісійної спектрометрії (ICP-OES) з використанням ICP-спектрометра ICAP 6500 DUO з індуктивно зв'язаною плазмою виробництва фірми Thermo Electron Corporation (США).

Для дослідження наявности або відсутности в титанових виливках внутрішніх дефектів у вигляді неметалевих включень, а також пор і нещільностей використовувалася метода ультразвукової дефектоскопії. Дослідження проводилися з використанням дефектоскопа ультразвукового УД4-76 (Україна) відлуння-імпульсною ме-

тодою із контактним варіянтом контролю.

Для виявлення мікроструктури зразків здійснювали щавлення в реактиві, який складається з суміші плавикової й азотної кислот у співвідношенні: 5% плавикової кислоти (HF), 30% азотної кислоти (HNO_3) та дистильованої води.

Огляд структури зразків здійснювали на світловому мікроскопі «Neophot-32» (Німеччина) за різних збільшень. Також на растровому електронному мікроскопі JEOL JSM-840 (JEOL Ltd, Японія) проведено мікроструктурні дослідження структурних складових, одержаних методою ЕПП стопу, а методою мікрорентґеноспектральної аналізи на приладі INCAPentaFET-x3 фірми «Oxford Instruments» (Англія) з Si(Li)-детектором встановлювався хемічний склад фаз і неметалевих включень, що утворилися.

Електронно-променеве зварювання (ЕПЗ) проводили на модернізованій установці УЛ-144, оснащеній джерелом живлення ЕЛА 60/60, зварювальною гарматою ЦФ-19 і приладом керування променем СУ-220. ЕПЗ виконували за один прохід без оброблення кромок і без присадного матеріялу; тому властивості зварних з'єднань визначалися хемічним складом основного металу, кількістю леґувальних елементів і домішок, режимом зварювання та характером термічного циклу.

5. ДОСЛІДЖЕННЯ СТРУКТУРИ ЛИТОГО ІНТЕРМЕТАЛІДНОГО ТИТАНОВОГО СТОПУ, ОДЕРЖАНОГО МЕТОДОЮ ЕЛЕКТРОННО-ПРОМЕНЕВОГО ТОПЛЕННЯ, ТА СТРУКТУРИ МЕТАЛУ ШВА ПІСЛЯ ЕПЗ

5.1. Хемічний склад виливка інтерметалідного титанового стопу, одержаного методою електронно-променевого топлення

На електронно-променевій установці УЕ-121 одержано виливок стопу Ti–28Al–7Nb–2Mo–2Cr (ваг.%) діяметром у 200 мм і довжиною у 500 мм. Відбір проб проводили вздовж виливка на глибині у 10 мм від поверхні виливка. Досліджувалися три зони — верхня, нижня та середина виливка. Результати досліджень хемічного складу металу показали достатньо рівномірний розподіл леґувальних елементів по довжині витопленого виливка (табл. 1).

Ультразвуковий контроль одержаного виливка не виявив внутрішніх дефектів.

5.2. Дослідження структури інтерметалідного титанового стопу, одержаного методою електронно-променевого топлення

Макроструктура інтерметалідного стопу Ti–28Al–7Nb–2Mo–2Cr

ТАБЛИЦЯ 1. Хемічний склад виливка ЕПП ∅ 200 мм.

TABLE 1. Chemical composition of EBM ingot ∅ 200 mm.

Місце відбору зразків	Вміст елементів, мас.%				
	Al	Nb	Mo	Cr	Ti
Верх	27,6	7,6	2,0	1,5	
Середина	28,7	7,5	2,1	1,8	осн.
Низ	29,5	7,2	2,2	1,7	

характеризується зернами, близькими до рівновісних (рис. 1). Величина зерна, що визначається за 10-бальною шкалою макроструктур Інструкції № 1054-76, відповідає 8–9 балам (присутні ділянки з балом зерна у 6–7). Істотної ріжниці у характері кристалізації по довжині виливка не спостерігається.

У процесі вивчення мікроструктури металу виливка методою оптичної мікроскопії виявлено кілька фазових складових: *1* — світла матрична фаза; *2* — ділянки з лямелярною структурою на тлі матриці (рис. 2, *в*); *3* — темна фаза, яка утворює сітчастий візерунок на тлі матриці (рис. 2, *а*, *б*); *4* — світла фаза, частинки якої мають різну форму та примикають до фази, що утворює сітку (рис. 2, *г*).

На растровому електронному мікроскопі проведено дослідження структурних складових одержаного методою ЕПП стопу Ti–28Al–7Nb–2Mo–2Cr та встановлено хемічний склад фаз і включень, що утворилися (рис. 3).

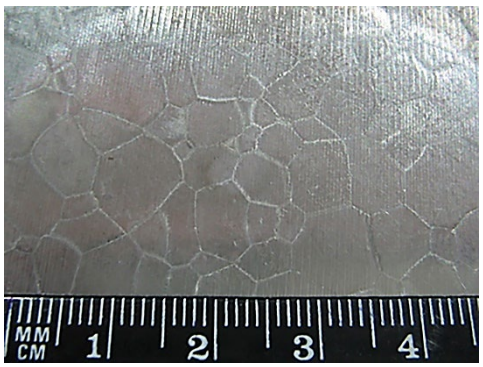

Рис. 1. Макроструктура поперечного перерізу виливка алюмініду титану Ti–28Al–7Nb–2Mo–2Cr (ваг.%) ∅ 200 мм.

Fig. 1. Macrostructure of the cross-section of titanium-aluminide ingot Ti–28Al–7Nb–2Mo–2Cr (wt.%) ∅ 200 mm.

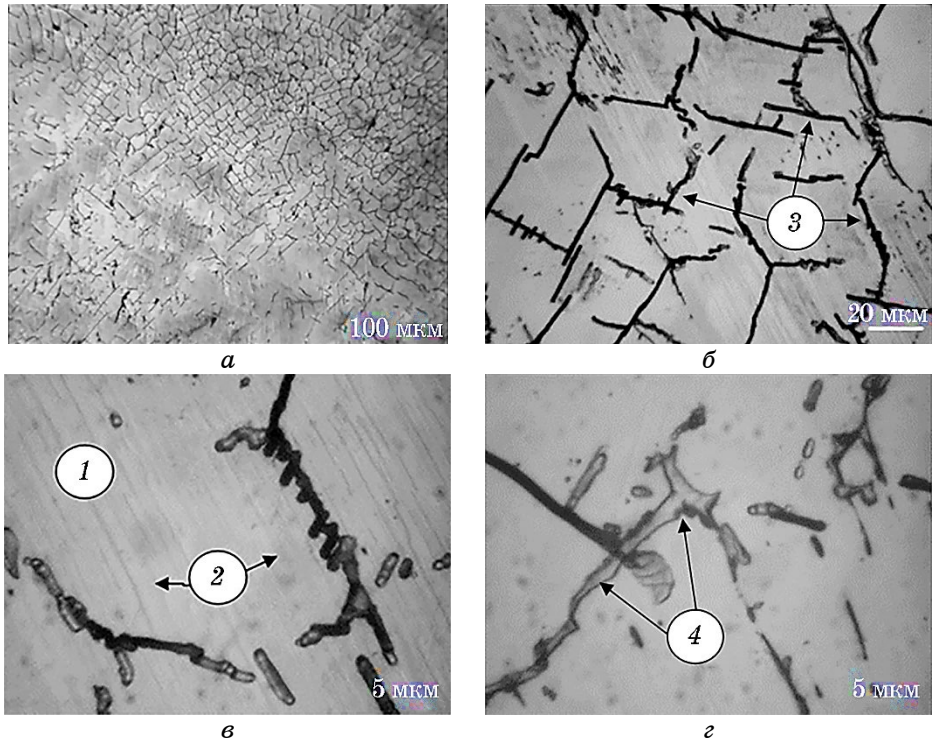

Рис. 2. Мікроструктура зразків виливка алюмініду титану.

Fig. 2. Microstructure of titanium-aluminide samples.

Рентґеноспектральні дослідження видовжених фаз по межах первинних зерен (рис. 3, *а*) показали, що вони збагачені Хромом (5,69%) і Молібденом (12,16%), але мають понижений вміст Алюмінію (23,04%) порівняно з матрицею. Це вказує на те, що це, ймовірно, — впорядкована кубічна β-фаза. Відомо, що леґування Ніобієм, Хромом і Молібденом, які є сильними β-стабілізаторами, приводить до утворення $\beta(B2) + \alpha_2$-структури, яка завдяки наявності $B2$-фази забезпечує більш високу пластичність матеріялу (понад 10%). Аналіза включень (рис. 3, *б*) вказує на підвищений вміст Молібдену (6,48%) і Ніобію (8,84%), що вказує на утворення складних фаз, які, ймовірно, уможливлюють підвищити жароміцні властивості матеріялу.

Аналіза области, яку наведено на рис. 3, *в*, показує, що це — пластинчата структура з почергових α_2- та γ-фаз, яка притаманна двофазним $(\alpha_2 + \gamma)$-алюмінідам титану. Аналіза включення на рис. 3, *г* вказує на те, що це, як і включення на рис. 3, *а*, — ймовірно, також є $\beta/B2$-фазою, яка має понижений вміст Алюмінію (18,64%) і під-

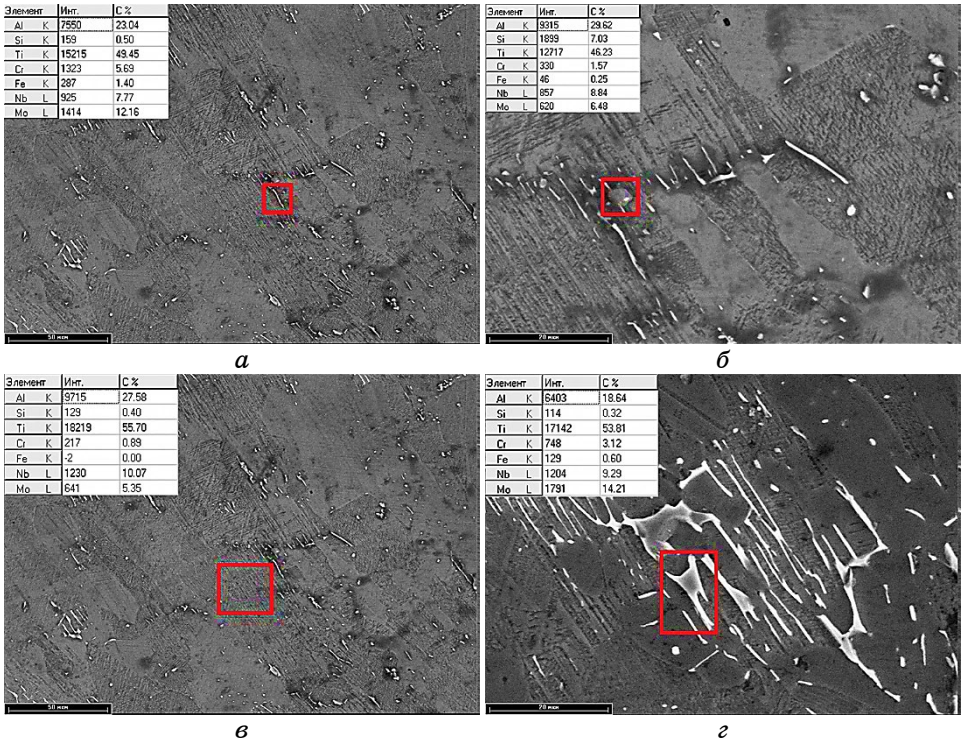

Рис. 3. Електронне зображення та локальна хемічна аналіза фаз, що утворилися за кристалізації виливка ЕПП Ti–28Al–7Nb–2Mo–2Cr ∅ 200 мм.

Fig. 3. Electronic image and local chemical analysis of the phases formed during the crystallization of the EBM ingot of Ti–28Al–7Nb–2Mo–2Cr ∅ 200 mm.

вищений вміст Молібдену (14,21%) і Ніобію (9,29%).

Методою рентґеноспектральної аналізи було визначено розподіл елементів по полю зразка. Встановлено, що розподіл основних леґувальних елементів по полю зразка у межах сусідніх зерен є достатньо рівномірним. Є деякі неістотні відхилення за складом із переходом меж від одного зерна до іншого. Відхилення в хемічному складі спостерігаються тільки із переходом через світлі включення. Таким чином, проведена фазова аналіза мікроструктури стопу Ti–28Al–7Nb–2Mo–2Cr, одержаного методою ЕПП, показала, що вона складається з матричної світлої однофазної структури γ-TiAl (фаза *1* рис. 2), що чергується з ділянками двофазної $(\gamma+\alpha_2)$-лямельної структури (фаза *2* рис. 2) розміром до 50 мкм із товщиною лямелей близько 1 мкм, та $\beta/B2$-фази (фаза *4* рис. 2), яка утворює сітчастий візерунок на тлі матриці.

6. ДОСЛІДЖЕННЯ СТРУКТУРИ ЗВАРНОГО З'ЄДНАННЯ ІНТЕРМЕТАЛІДНОГО ТИТАНОВОГО СТОПУ, ОДЕРЖАНОГО МЕТОДОЮ ЕЛЕКТРОННО-ПРОМЕНЕВОГО ТОПЛЕННЯ

Зварювання зразків зі стопу Ti–28Al–7Nb–2Mo–2Cr на основі алюмініду титану товщиною у 8 мм, попередньо підігрітого до 400°С, виконували зі швидкостями зварювання у 7 мм/с. Після зварювання зварні з'єднання піддавалися локальному термообробленню у вакуумній камері за температури у 750°С протягом 10 хвилин [20]. Зображення поперечного макрошліфа зварного з'єднання стопу Ti–28Al–7Nb–2Cr–2Mo, виконаного ЕПЗ з попереднім підігрівом і післязварювальним локальним термічним обробленням (ЛТО), наведено на рис. 4.

Формування швів під час ЕПЗ з попереднім підігрівом і післязварювальним ЛТО добре: підрізів, пор і тріщин не виявлено. Не виявлено тріщин ні в зварному шві, ні в зоні термічного впливу. Таким чином, попередній підігрів за 400°С та післязварювальне ЛТО за температури у 750°С ефективно запобігають утворенню тріщин у з'єднаннях алюмініду титану Ti–28Al–7Nb–2Cr–2Mo.

Мікроструктуру металу шва, виконаного ЕПЗ, представлено на рис. 5. Метал шва складається переважно з великих, витягнутих у напрямку тепловідведення зерен; тільки вздовж осі шва утворюються дрібніші рівновісні зерна розміром у 100–200 мкм (рис. 5, *а*, *б*). Лінійна темна фаза, що утворює сітку, розташована у вигляді поперечних щодо осі шва смуг у середній по висоті частині шва (рис. 5, *а*). У верхній і кореневій (рис. 5, *б*) частинах шва структурні складові у вигляді сітки не спостерігаються. Внутрішньозеренна структура металу середньої частини шва складається з невеликих (до 20 мкм) ділянок з лямельною структурою із товщиною лямелей

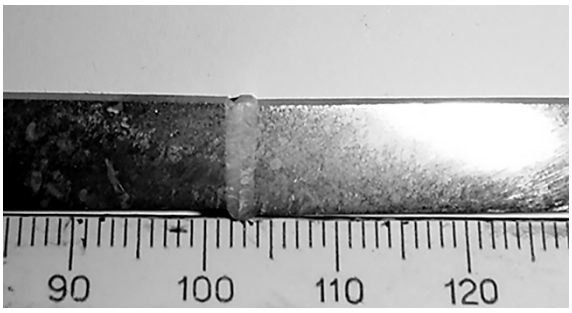

Рис. 4. Макрошліф зварного з'єднання стопу на основі алюмініду титану Ti–28Al–7Nb–2Mo–2Cr, виконаного ЕПЗ.

Fig. 4. Macrosample of a welded joint of the alloy based on titanium-aluminide Ti–28Al–7Nb–2Mo–2Cr produced by means of EBW.

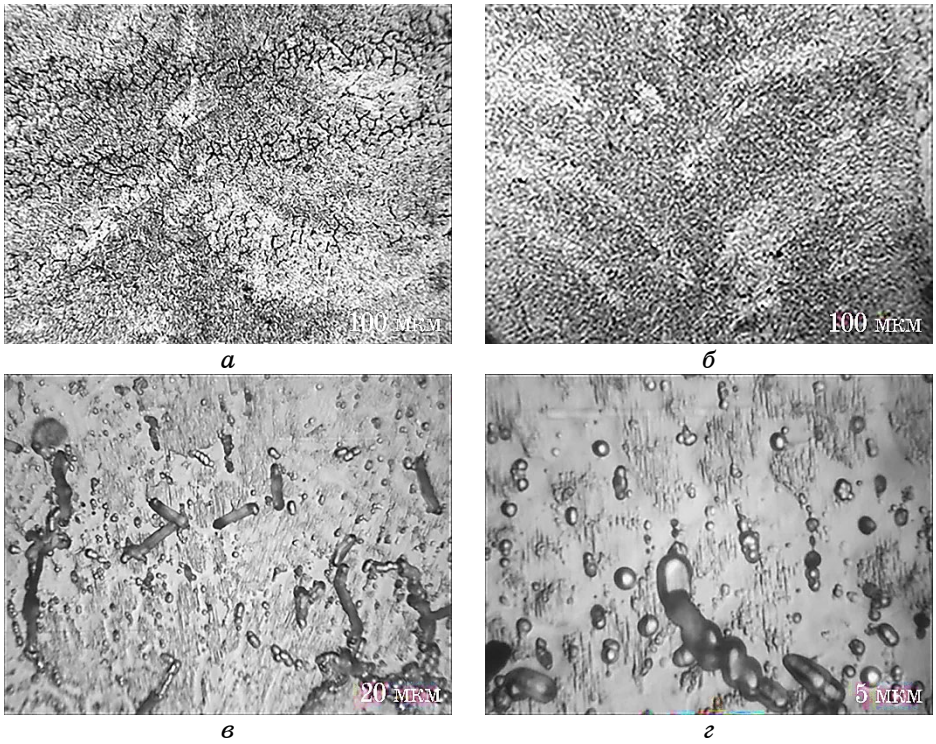

а *б* *в* *г*

Рис. 5. Мікроструктура металу шва зварного з'єднання, виконаного ЕПЗ алюмініду титану Ti–28Al–7Nb–2Cr–2Mo.

Fig. 5. The microstructure of the metal of the welded joint of titanium-aluminide Ti–28Al–7Nb–2Cr–2Mo produced by means of EBW.

близько 1 мкм на тлі світлої матричної фази. Крім того, в структурі присутні лінійні частинки, що утворюють сітку довжиною у 3–80 мкм, завтовшки у 1–3 мкм (рис. 5, *в*), яка буває як однорідною (рис. 5, *а*), так і фраґментованою (рис. 5, *г*). На багатьох лінійних частинках концентруються дисперсні фазові виділення, що розташовуються і на тлі матричної фази. У структурі металу шва також присутні округлі елементи, які є мікропорами; їхній розмір становить 1–2 мкм.

Так було досліджено мікроструктуру зони термічного впливу (ЗТВ), яку зображено на рис. 6. На відміну від основного металу, в ЗТВ спостерігається лямелярна структура із достатньо невеликою довжиною лямелей (до 10 мкм) і товщиною близько 1 мкм (рис. 6, *б*). Також метал ЗТВ відрізняється значно меншою щільністю розташування ділянок із лямелярною структурою (рис. 6, *в*). Інші структурні складові ЗТВ ідентичні аналогічним елементам

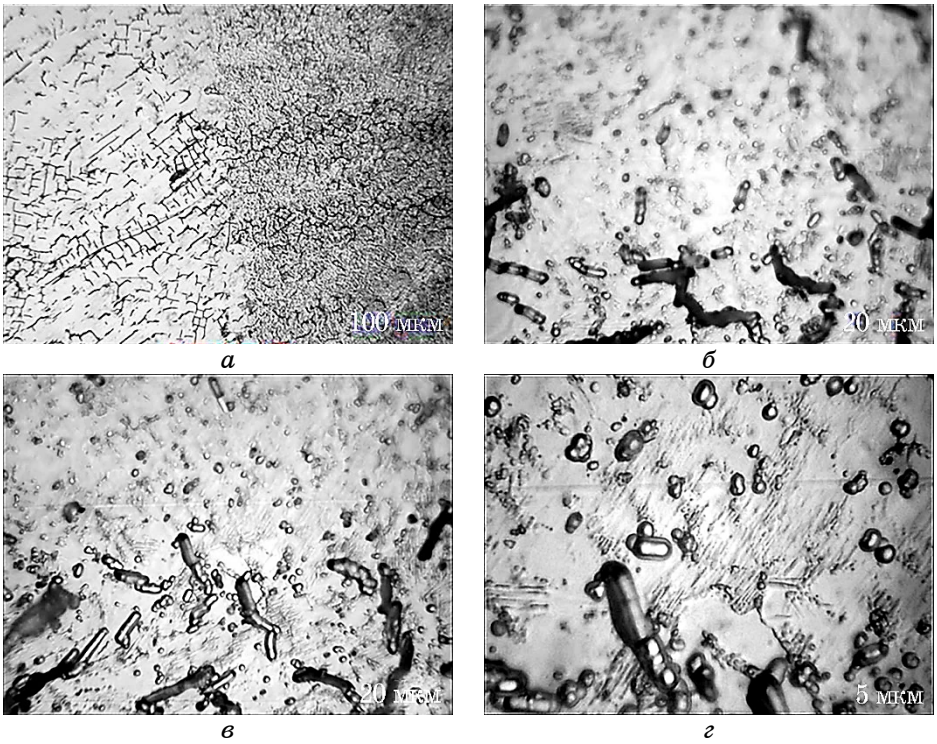

Рис. 6. Мікроструктура металу ЗТВ зварного з'єднання алюмініду титану Ti–28Al–7Nb–2Cr–2Mo, виконаного ЕПЗ.

Fig. 6. The microstructure of the metal of the heat-affected zone of the welded joint of titanium-aluminide Ti–28Al–7Nb–2Cr–2Mo produced means of EBW.

структури металу шва, за винятком того, що фаза, що утворює сітчасту структуру, в ЗТВ не утворює поперечних щодо осі шва смуг, а, швидше за все, успадковує характер розташування фази основного металу, що утворює сітку (рис. 6, *г*).

7. ОБГОВОРЕННЯ РЕЗУЛЬТАТІВ ДОСЛІДЖЕННЯ СТРУКТУРИ ЛИТОГО МЕТАЛУ ТА МЕТАЛУ ЗВАРНОГО З'ЄДНАННЯ ІНТЕРМЕТАЛІДНОГО ТИТАНОВОГО СТОПУ, ОДЕРЖАНОГО МЕТОДОЮ ЕЛЕКТРОННО-ПРОМЕНЕВОГО ТОПЛЕННЯ

Результати дослідження інтерметалідного титанового стопу Ti–28Al–7Nb–2Mo–2Cr, одержаного за технологією ЕПП, показало, що в об'ємі виливку відсутні дефекти, неметалеві включення, а також щільні скупчення більш дрібних включень. Структура одержаного металу ЕПП є щільною, кристалічна неоднорідність і зона-

льна ліквація відсутні. Характерної для виливків ВДП сеґреґації леґувальних елементів не виявлено. Розподіл леґувальних елементів по довжині виливка є достатньо рівномірним (табл. 1). Макроструктура металу виливка є рівномірною по усьому перетину та характеризується кристалами, за формою близькими до рівновісної (рис. 1). Ділянки стовбчастої структури відсутні.

Досліджена мікроструктура стопу Ti–28Al–7Nb–2Mo–2Cr є типовою для двофазних алюмінідів титану і складається з матричної світлої однофазної γ-фази, що чергується з ділянками двофазної $(\gamma + \alpha_2)$-лямельної структури, але завдяки великій кількості β-стабілізувальних леґувальних елементів має достатньо великий об'єм $\beta(B2)$-фази, яка утворює сітчастий візерунок на тлі матриці (рис. 2 та рис. 3).

Встановлено, що литий метал виливків алюмініду титану Ti–28Al–7Nb–2Cr–2Mo задовільно зварюється ЕПЗ. Під час ЕПЗ без попереднього підігріву та ЛТО в з'єднаннях утворюються поперечні та повздовжні холодні тріщини. Для попередження утворення тріщин потрібно застосовувати попередній підігрів і ЛТО. Температуру попереднього підігріву обрано у 400°C згідно з досвідом зварювання стопу на основі алюмініду титану 47XD. Формування швів під час ЕПЗ з попереднім підігрівом і після зварювального ЛТО є добрим: підрізів, пор і тріщин не виявлено. Внутрішньозеренна структура металу середньої частини шва складається з невеликих (до 20 мкм) ділянок з лямельною структурою на тлі світлої матричної фази; товщина лямелей у металі шва — близько 1 мкм.

Таким чином, проведені дослідження показали, що електронно-променеве топлення є ефективною методою одержання якісних складнолеґованих виливків інтерметалідних титанових стопів, а електронно-променеве зварювання уможливлює одержати якісне зварне з'єднання цих матеріялів.

8. ВИСНОВКИ

1. Електронно-променеве топлення є ефективною методою одержання якісних складнолеґованих виливків інтерметалідних титанових стопів, а електронно-променеве зварювання уможливлює одержати якісне зварне з'єднання цих матеріялів. Методою ЕПП одержано виливки інтерметалідного титанового стопу Ti–28Al–7Nb–2Mo–2Cr, які характеризуються достатньою хемічною однорідністю та відсутністю дефектів литого походження.
2. Показано, що макроструктура стопу Ti–28Al–7Nb–2Mo–2Cr, одержаного методою ЕПП, є однорідною по усьому перетину виливка та характеризується кристалами, за формою близькими до рівновісної, а його мікроструктура складається з матричної світлої γ-фази, що чергується з ділянками двофазної $(\gamma + \alpha_2)$-лямельної структури

розміром до 50 мкм із товщиною лямелей близько 1 мкм, та кубічної β-фази, яка утворює сітчастий візерунок на тлі матриці.
3. Внутрішньозеренна структура металу шва після ЕПЗ з ЛТО відрізняється від структури основного металу та складається з невеликих (до 20 мкм) ділянок із ($\gamma + \alpha_2$)-лямельною структурою на тлі світлої матричної γ-фази із сіткою з лінійних частинок довжиною у 3–80 мкм і товщиною у 1–3 мкм.
4. Розроблено технологію зварювання виливків на основі алюмініду титану Ti–28Al–7Nb–2Cr–2Mo, одержаних методою ЕПП. В умовах застосування додаткових технологічних прийомів, а саме, попереднього підігріву (за 400°C) та локального післязварювального термічного оброблення (за 750°C) уможливлює одержати метал без підрізів, пор та ефективно запобігти утворенню тріщин у зварних з'єднаннях алюмініду титану Ti–28Al–7Nb–2Cr–2Mo.

Автори декларують, що не мають конфлікту інтересів стосовно даного дослідження, в тому числі фінансового, особистісного характеру, авторства чи іншого характеру, що міг би вплинути на дослідження та його результати, представлені в даній статті.

ЦИТОВАНА ЛІТЕРАТУРА

1. F. Appel, J. D. H. Paul, and M. Oehring, *Gamma Titanium Aluminide Alloys – Science and Technology* (Weinheim: Wiley-VCH: 2011).
2. H. Clemens and S. Mayer, *Adv. Eng. Mater.*, **15**: 191 (2013).
3. H. Clemens, M. Schloffer, E. Schwaighofer, R. Werner, A. Gaitzenauer, B. Rashkova, T. Schmoelzer, R. Pippan, and S. Mayer, *MRS Online Proc. Libr.*, **1516**: 3 (2013).
4. B. P. Bewlay, M. Weimer, T. Kelly, A. Suzuki, and P. R. Subramanian, *MRS Online Proc. Libr.*, **1516**: 49 (2013).
5. А. А. Ильин, Б. А. Колачев, И. С. Полькин, *Титановые сплавы. Состав, структура, свойства: Справочник* (Москва: ВИЛС–МАТИ: 2009).
6. O. Genc and R. Unal, *J. Alloys and Compd.*, **929**: 167262 (2022).
7. С. В. Ладохин, *Электронно-лучевая плавка в литейном производстве* (Киев: Сталь: 2007).
8. J. C. Williams and R. R. Boyer, *Metals*, **10**, Iss. 6: 705 (2020).
9. H. Mizukami, T. Kitaura, and Y. Shirai, *MATEC Web Conf. The 14th World Conference on Titanium (Ti 2019)*, **321**: 10005 (2020).
10. Е. П. Бабенко, Е. В. Долженкова, *Металлургическая и горнорудная промышленность*, **3**: 82 (2014).
11. S. Akhonin, O. Pikulin, V. Berezos, A. Severyn, O. Erokhin, and V. Kryzhanovskyi, *East.-Eur. J. Enterp. Technol.*, **5**, No. 12: 6 (2022).
12. Г. В. Жук, Н. П. Тригуб, В. Н. Замков, *Современная электрометаллургия*, **4**: 20 (2003).
13. С. В. Ахонін, А. Ю.Северин, В. О. Березос, О. М. Пікулін, О. Г. Єрохін, *Сучасна електрометалургія*, **1**: 11 (2022).
14. G. Q. Chen, B. G. Zhang, W. Liu, and J. C. Feng, *Intermetallics*, **19**, Iss. 12:

1857 (2011).
15. M. C. Chaturvedi, Q. Xu, and N. L. Richards, *J. Mater. Process. Technol.*, **118**, No. 1: 74 (2001).
16. U. Reisgen, S. Olschok, and A.Backhaus, *Mater. Werkst*, **41**, Iss. 11: 897 (2010).
17. J. Cao, J. Qi, X. Song, and J. Feng, *Materials*, **7**: 4930 (2014).
18. В. Н. Замков, А. Е. Великоиваненко, В. К. Сабокарь, Э. Л. Вржижевский, *Автоматическая сварка*, **11**: 20 (2001).
19. J. Cao, J. Qi, X. Song, and J. Feng, *Materials*, **7**: 4930 (2014).
20. S. V. Akhonin, V. Y. Belous, and R. V. Selin, *Mater. Sci. Forum*, **1059**: 15 (2022).

REFERENCES

1. F. Appel, J. D. H. Paul, and M. Oehring, *Gamma Titanium Aluminide Alloys – Science and Technology* (Weinheim: Wiley-VCH: 2011).
2. H. Clemens and S. Mayer, *Adv. Eng. Mater.*, **15**: 191 (2013).
3. H. Clemens, M. Schloffer, E. Schwaighofer, R. Werner, A. Gaitzenauer, B. Rashkova, T. Schmoelzer, R. Pippan, and S. Mayer, *MRS Online Proc. Libr.*, **1516**: 3 (2013).
4. B. P. Bewlay, M. Weimer, T. Kelly, A. Suzuki, and P. R. Subramanian, *MRS Online Proc. Libr.*, **1516**: 49 (2013).
5. A. A. Il'in, B. A. Kolachev, and I. S. Pol'kin, *Titanovyye Splavy. Sostav, Struktura, Svoistva: Spravochnik* [Titanium Alloys. Composition, Structure, Properties: Handbook] (Moscow: VILS–MATI: 2009) (in Russian).
6. O. Genc and R. Unal, *J. Alloys and Compd.*, **929**: 167262 (2022).
7. S. V. Ladokhin, *Elektronno-Luchevaya Plavka v Liteynom Proizvodstve* [Electron Beam Melting in Foundries] (Kiev: Stal': 2007) (in Russian).
8. J. C. Williams and R. R. Boyer, *Metals*, **10**, Iss. 6: 705 (2020).
9. H. Mizukami, T. Kitaura, and Y. Shirai, *MATEC Web Conf. The 14th World Conference on Titanium (Ti 2019)*, **321**: 10005 (2020).
10. E. P. Babenko and E. V. Dolzhenkova, *Metallurgicheskaya i Gornorudnaya Promyshlennost'*, **3**: 82 (2014) (in Russian).
11. S. Akhonin, O. Pikulin, V. Berezos, A. Severyn, O. Erokhin, and V. Kryzhanovskyi, *East.-Eur. J. Enterp. Technol.*, **5**, No. 12: 6 (2022).
12. G. V. Zhuk, N. P. Trigub, and V. N. Zamkov, *Sovremennaya Elektrometallurgiya*, **4**: 20 (2003) (in Russian).
13. S. V. Ahonin, A. Yu. Severyn, V. O. Berezos, O. M. Pikulin, and O. G. Jerohin, *Suchasna Elektrometalurgiya*, **1**: 11 (2022) (in Ukrainian).
14. G. Q. Chen, B. G. Zhang, W. Liu, and J. C. Feng, *Intermetallics*, **19**, Iss. 12: 1857 (2011).
15. M. C. Chaturvedi, Q. Xu, and N. L. Richards, *J. Mater. Process. Technol.*, **118**, No. 1: 74 (2001).
16. U. Reisgen, S. Olschok, and A.Backhaus, *Mater. Werkst*, **41**, Iss. 11: 897 (2010).
17. J. Cao, J. Qi, X. Song, and J. Feng, *Materials*, **7**: 4930 (2014).
18. V. N. Zamkov, A. E. Velikoivanenko, V. K. Sabokar', Ye. L. Vrzhyzhevskyy, *Avtomaticheskaya Svarka*, **11**: 20 (2001) (in Russian).
19. J. Cao, J. Qi, X. Song, and J. Feng, *Materials*, **7**: 4930 (2014).
20. S. V. Akhonin, V. Y. Belous, and R. V. Selin, *Mater. Sci. Forum*, **1059**: 15 (2022).

Metallophysics and Advanced Technologies
Металофіз. новітні технол.
Metallofiz. Noveishie Tekhnol.
2024, vol. 46, No. 5, pp. 431–452
https://doi.org/10.15407/mfint.46.05.0431
Reprints available directly from the publisher

PACS numbers: 06.60.Vz, 68.37.Yz, 78.70.En, 81.20.Vj, 81.40.Ef, 81.40.Lm, 81.70.Bt

Study on Normalizing and Tempering Treatment Regime of Homogenization of P92 Weldments

V. K. Pal and L. P. Singh

Department of Mechanical Engineering,
Sam Higginbottom University of Agriculture, Technology and Sciences Allahabad,
IN-211007 Uttar Pradesh, India

The present research work describes the effect of normalizing and tempering (N&T) treatment on microstructure evolution in various zones of gas tungsten arc-welded (GTAW) P92 pipe weldments. For N&T treatment, P92 pipe weldments are subjected to various normalizing (950–1150°C) and tempering (730–800°C) temperatures. The effect of varying heat treatment on tensile properties and hardness of P92 pipe weldments are studied for V-groove and narrow-groove weld designs. The effect of increase in normalizing temperature (at fixed tempering temperature) results in increase in strength and hardness, while increase in tempering temperature (at fixed normalizing temperature) results in the decrease in strength and hardness of P92 steel weldments. Creep strength-enhanced ferritic/martensitic P92 steel is considered as a candidate material for the reactor pressure vessels and reactor internals of Very High Temperature Reactor (VHTR). The heterogeneous microstructure formation across the P92 weldments leads to premature Type IV cracking and makes the weldability of P92 steel as a serious issue. The better combination of strength, ductility and microstructure are obtained for the maximum normalizing temperature of 1050°C and tempering temperature of 760°C. The effect of increase in normalizing temperature (at fixed tempering temperature) results in increase in strength and hardness, while increase in tempering temperature (at fixed normalizing temperature) results in the decrease in strength and hardness of P92 steel weldments.

Key words: normalizing, tempering, P92 pipe weldments, microstructure, mechanical properties.

Corresponding author: Vinay Kumar Pal
E-mail: gaurishankar.vinaypal@gmail.com

Citation: V. K. Pal and L. P. Singh, Study on Normalizing and Tempering Treatment Regime of Homogenization of P92 Weldments, *Metallofiz. Noveishie Tekhnol.*, **46**, No. 5: 431–452 (2024). DOI: 10.15407/mfint.46.05.0431

У цій дослідницькій роботі описано вплив нормалізації та відпуску на еволюцію мікроструктури в різних зонах зварних з'єднань труб P92, зварених газовольфрамовим дуговим зварюванням. Для нормалізації та відпуску зварні з'єднання труб P92 піддавали різним температурам нормалізації (950–1150°C) та відпуску (730–800°C). Вплив різного термічного оброблення на розривні властивості та твердість зварних швів труб P92 вивчали для V-подібних і вузькоканавочних зварних швів. Підвищення температури нормалізації (за фіксованої температури відпуску) привело до збільшення міцности та твердости, тоді як пониження температури відпуску (за фіксованої температури нормалізації) призвело до зменшення міцности та твердости зварних з'єднань із криці P92. Феритно-мартенситна криця P92 з підвищеною міцністю на плазучість розглядається як матеріял-кандидат для корпусів реактора та внутрішніх частин надвисокотемпературного реактора (HBTP). Неоднорідна мікроструктура, що утворюється у зварних швах із криці P92, призводить до передчасного розтріскування IV типу та робить зварюваність криці P92 серйозною проблемою. Найліпше поєднання міцности, пластичности та мікроструктури було одержано за максимальної температури нормалізації у 1050°C та температури відпуску у 760°C. Ефект підвищення температури нормалізації (за фіксованої температури відпуску) призвів до збільшення міцности та твердости, тоді як підвищення температури відпуску (за фіксованої температури нормалізації) призвело до зменшення міцности та твердости зварних з'єднань із криці P92.

Ключові слова: нормалізація, відпуск, P92-трубні зварні вироби, мікроструктура, механічні властивості.

(Received 7 August 2023; in final version, 5 October 2023)

1. INTRODUCTION

P92 steel processed tempered martensitic microstructure obtained by normalizing and tempering treatment (N&T). Normalizing of P91 steel is generally carried out in the austenitizing temperature range of 1040–1060°C for 20–40 min, followed by air-cooling. The subsequent tempering is performed in the temperature range of 730–780°C for 1–2 h, followed by air-cooling. The strength of P92 steel is primarily derived from its stable microstructure. The stability of microstructure is governed by the tempered martensitic lath structure, sub-grain size, prior-austenite grain boundaries (PAGBs), lath width, lath boundaries, precipitate size and their distribution inside the structure, dislocation density, precipitate morphology and their amount [1]. Very High Temperature Reactor (VHTR), Sodium cooled fast reactors (SFRs) are being developed to fulfil the growing energy demand with a view to greater reliability, safety, economy and lesser environmental pollution [2, 3]. 9% Cr CSEF/M steels development started from last few decades, starting from plain 9Cr–1Mo (P9), modified 9Cr–1Mo

(P91) and P92 steel. P91 steel is next version of plain 9Cr–1Mo steel, which was developed in Oak-Ridge National Laboratory (ORNL) by modifying the chemical composition of P9 steel [4, 5]. P92 steel was developed by adding the strong carbide and carbonitride former element such as 0.2 wt.% vanadium, 0.08 wt.% niobium, and 0.05 wt.% nitrogen. El-Azim *et al.* [6] performed a comparative study on creep behaviour of P91 steel joint and base metal. The creep strength of base metal was observed to be superior to weld joint at higher creep exposure temperature about 650°C while at a lower temperature about 600°C, it approached to creep strength of the base metal. Fracture location was observed in the base metal near to HAZ for short-term creep exposure (426 h) at 600°C and high applied stress of 150 MPa. The lower applied stress for same applied temperature was resulted in shifting of fracture location and type IV fracture occurred in FGHAZ of the weld joint. Laha *et al.* [7] reported the soft zone formation in IC-HAZ of P91 joint and type IV fracture was associated with IC-HAZ. Maruyama *et al.* [8] reported that the precipitate remains undissolved are mainly Type I Nb*X*. The undissolved precipitates limit the austenitic grain growth during normalizing treatment. The undissolved MX precipitates provide the pinning effect to grain boundaries and produce a fine-grained structure during normalizing. The modified *Z*-phase comes out after long-term exposure at a temperature about 600–700°C [9]. The dissolution temperature of modified *Z*-phase was reported about 800°C which is much lower than the solution temperature of original *Z*-phase (1200–1250°C) [9]. The heating of creep exposure steel above 800°C resulted in the formation of M*X* nitride from the *Z*-phase [10]. Abd El-Salam *et al.* [11] had incorporated the effect of normalizing/tempering (N&T) treatment on microstructure homogenization of shielded metal arc welded P91 joint and compared it with subsequent PWHT. For N&T treatment, the optimum degree of hominization was observed along the weldments that were attributed due to the recrystallization effect during the normalizing. Manugula *et al.* [12] had performed the N&T and subsequent PWHT for electron-beam welded reduced activated ferritic–martensitic steel. The weld was produced with poor toughness and high hardness due to the presence of δ-ferrite in the martensitic microstructure. Subsequent PWHT resulted in significant reduction in hardness of weld fusion zone but the heterogeneous distribution of hardness across the weldments was still present with δ-ferrite. Albert *et al.* [13] have also studied the effect of PWHT duration on type IV cracking nature in P122 weld joints. The creep test was performed at 650°C for 70 MPa. PWHT duration was varied from 15 min to 4 h, but no any significant change was observed in creep rupture time and fracture behaviour. In all the cases, type IV fracture was observed. Sawada *et al.* [14] have studied the cross-weld long-term creep behaviour of E911 joint at 600°C. The fracture was noticed in

soft FGHAZ. The growth of $M_{23}C_6$ in FGHAZ was observed faster than the base metal. The *Z*-phase formation was observed both in FGHAZ and base metal FGHAZ exhibited higher number density of *Z*-phase than the base metal. For long-term creep exposure at the low level of stress, creep life was observed to be minimum in FGHAZ [15].

A systematic study of different normalizing and tempering temperature combination that leads to the optimum combination of mechanical properties and microstructure stability, considering the necessity of effect of N&T treatment on microstructure stability and mechanical properties of P92 steel weldments, efforts are being made to perform.

2. EXPERIMENTAL DETAILS

2.1. Groove Design and Welding Process Parameters

The base metal used for the experiment was P92 pipe with an outer diameter of 60.3 mm and thickness of 11 mm. Gas tungsten arc welding (GTAW) of P92 pipes was carried out using conventional V-groove and narrow-groove designs. The conventional V-groove and narrow grove pipes and weld design is shown in Fig. 1, *a*–*c*. The conventional V-groove design used for the weld confirms to Section IX of the ASME Boiler and Pressure Vessel Code. Initial groove openings for conventional V-groove and narrow-groove were 14.58 and 9.06 mm, respectively (as measured after groove preparation). The conventional V-grooved and narrow-grooved pipes after the tack welding are shown in Fig. 2, *a*. To weld the P92 pipe joints using the GTAW process, a welding turntable with a rotating three-jaw self-centring chuck was uti-

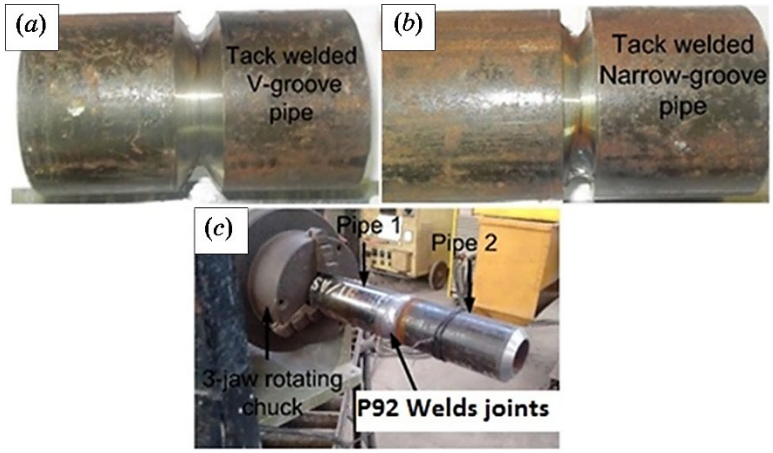

Fig. 1. (*a*) and (*b*) grooved pipe joints with tacking, (*c*) experimental set-up with welded pipe joints.

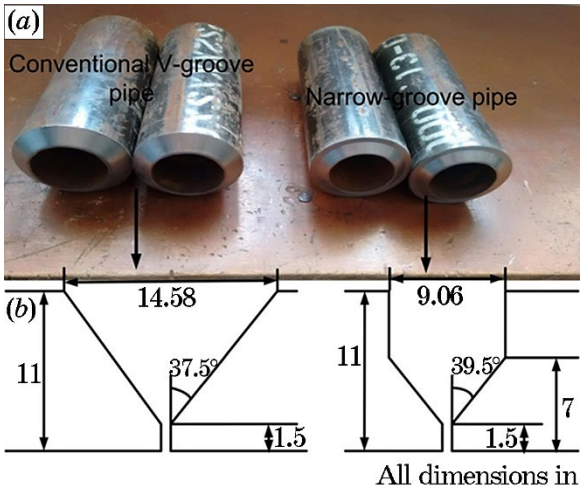

Fig. 2. (*a*) P92 pipe with conventional and narrow weld-groove design (*b*) Conventional V-groove and narrow-groove design.

TABLE 1. Chemical composition of P92 pipe, AWSER90S-B9 (9CrMoV-N) filler wire, and weld metal (wt.%).

Element	C	Mn	Cr	Si	Mo	V	Nb	Ni	S	Ti	W	Cu	Fe
P92 steel	0.12	0.54	8.48	0.28	0.95	0.18	0.05	0.35	0.011	0.012	<0.001	0.06	Rest
Filler metal	0.12	0.50	8.83	0.30	0.90	0.20	0.06	0.50	0.019	0.001	–	–	Rest
Weld metal	0.11	0.52	8.28	0.28	0.87	0.20	0.04	0.44	0.019	<0.002	<0.001	0.05	Rest

lized. P92 pipes of 150 mm length were multipass welded (eight passes for conventional V-groove and seven passes for narrow-groove) at 1-GR position (pipe rolled in flat position), as shown in Fig. 2, *b*. The welded pipe joints with experimental set-up are shown in Fig. 2, *b*.

The AWSER90S-B9 (9CrMoV–N) filler wire with a diameter of 1.6 mm was used for the GTAW purpose. The composition of the as-received material, filler wire and weld metal are given in Table 1. GTAW parameters for the root pass were 110 A DC and 12 V. For subsequent GTAW passes, the filling parameters are given in Table 2. To maintain the linear travel speed of 2.11 mm/s during the filling pass, a motor-controlled fixture was used. The preheat temperature of 250°C was maintained by using the flame heating and interpass temperature was selected in the range of 200–250°C. For the shielding purpose,

TABLE 2. Welding process parameter.

Nos. of passes	Current (amp)	Voltage (V)	Travel speed (mm/sec)	Current (amp)	Voltage (V)	Travel speed (mm/sec)
	Conventional V-groove			Narrow-groove		
Root pass	105–115	12	1.47	105–115	12	1.47
1	110–115	12–14	2.11	110–115	12–15	2.11
2	120–125	12–15	2.11	110–115	12–15	2.11
3	118–124	14–16	2.11	112–120	14–16	2.11
4	120–123	12–14	2.11	118–124	15–18	2.11
5	110–115	18–20	2.11	118–124	14–18	2.11
6	112–120	14–16	2.11	115–120	14–15	2.11
7	120–125	12–14	2.11	114–118	13–16	2.11
8	120–125	12–15	2.11	–	–	–

pure argon gas was used with a flow rate of 15 l/min.

2.2. Heat Treatment of P92 Weldments

After the completion of welding, the weld joints were subjected to three different heat conditions as per given Table 3 One welded pipe joint of each groove type (V-groove and narrow groove) was allowed to cool in air up to room temperature without any heat treatment. The second one from each groove design was subjected to post-weld heating before post weld heat treatment (PWHT). Generally, post-weld heating of P92 weld to 250–300°C for 30 to 60 min followed by air cooling up to 100°C is recommended before PWHT for removing the diffusible hydrogen. The cooling is carried out to ensure the formation of complete martensitic microstructure just before PWHT, as residual austenite does not respond to the PWHT, which leads to the formation of harmful untempered martensite [16]. After the post-weld heating, subsequent PWHT was performed at 760°C for 2 h. The third weld joint was subjected to conventional normalizing and tempering or post weld normalizing and tempering (PWNT) heat treatment. The weld joints were reaustenitized at 1050°C for 40 min and air cooled, then tempered at 760°C for 2 h, and finally air-cooled. The PWHT was performed to homogenize the microstructure and remove the quench stresses by tempering the lath martensite. The PWHT temperature range should be below than the critical temperature (A_{c1}), which mainly depends on the fusion zone composition (Ni + Mn content). Newell [17] had also

TABLE 3. Different heat treatment condition performed just after the welding for V-groove and narrow groove designs.

P92 pipe weldments	Heat treatment condition
1 (as-welded)	After welding, allowed to cool in air up to room temperature
2 (PWHT)	After welding, PWHT in range of 250–300°C for 30 to 60 min and then air cooling up to 100°C followed by PWHT at 760°C for 2 h, followed by air cooling
3 (PWNT)	After welding, normalized at 1040°C for 60 min, and air-cooled and tempered at 760°C for 2 h, followed by air cooling

suggested that for the large size specimens, the PWHT temperature should be lower than A_{c1} by 10 to 20°C. Based on the Ni + Mn content in weld fusion zone, Santella *et al.* [18] had proposed a mathematical equation to calculate the A_{c1} temperature.

The equation is given below:

$$A_{c1}\,(°C) = 854{\cdot}5 \pm 0.6 - 43{\cdot}9 \pm 1 \times (Mn + Ni) - 9 \pm 0.4 \times (Mn + Ni)^2. \quad (1)$$

From this equation and Table 1, the A_{c1} temperature was calculated about 809°C. The PWHT parameter was as per the code recommended following ASME B31.1—760°C for 2 h.

2.3. Mechanical Testing and Characterization

To study the effect of different heat treatments (as-welded and PWHT) on yield strength, ultimate tensile strength, and percentage elongation of P92 steel weld joints, flat tensile test specimen was prepared as per ASTM A370-14 [19]. The room temperature tensile tests were performed on the vertical tensile testing specimen (Instron: 5982) at the constant crosshead speed of 1 mm/min. The gauge length and width of the flat tensile specimen were 50 mm and 11.8 mm, respectively. The microhardness of welded samples before and after PWHT was measured by using a Vickers hardness tester at a load of 500 g and dwell time of 10 s. Cross-sectional samples were prepared from welded pipes for both the conventional and narrow-groove designs in order to measure the hardness in various weld zones and base metal. The through-thickness hardness at the centre of the weld fusion zone was measured. Furthermore, the hardness was also measured across the welds at 4 mm below the weld reinforcement outer surface.

For both the through the thickness and across the weld hardness measurements, indented points were located along a straight line at

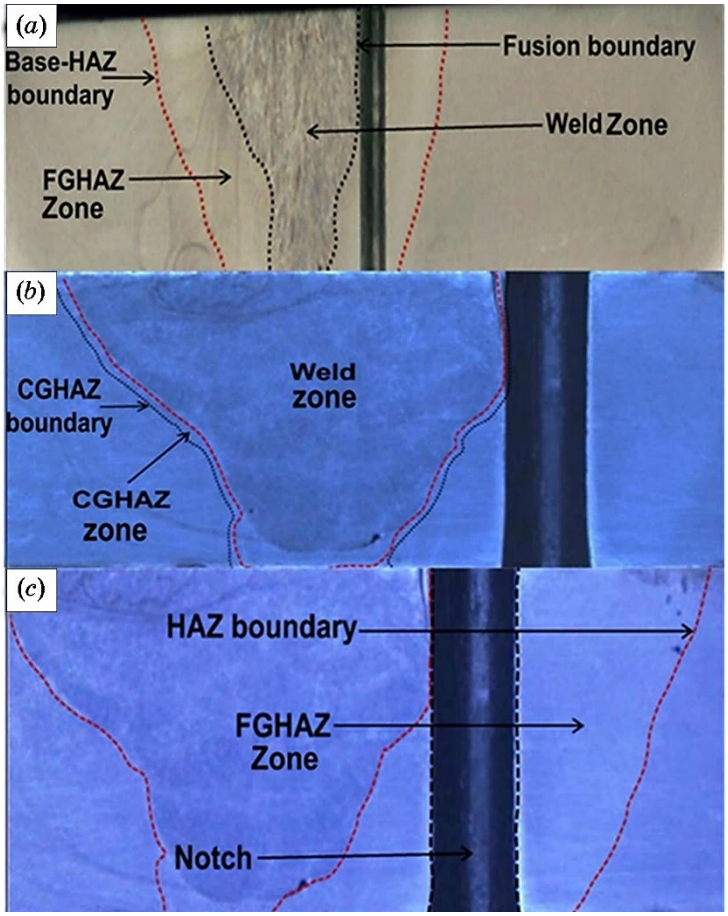

Fig. 3. Macrostructure of impact toughness specimens showing (*a*) weld zone, FGHAZ zone, base-HAZ boundary, fusion zone boundary, (*b*) CGHAZ boundary and CGHAZ zone, and (*c*) a notch adjacent to fusion boundary.

1 mm intervals. To study the impact toughness of P92 base metal in different operating temperature conditions, flat samples of 7.5 mm thickness were prepared from the pipe. Standard sub-size Charpy impact V-notch specimens ($55\times10\times7.5$ mm^3) were prepared according to ASTM A370-14 [19]. Charpy toughness tests were performed in the temperature range of 25–1000°C. For each test, three samples were prepared and an average of three test results has been reported.

To study the Charpy toughness of HAZ, notches were prepared in the HAZ of both conventional V-groove and narrow-groove-welded joints. Weld samples were polished using emery paper up to grit size 600 and then etched with Nital solution (10% nitric acid in methanol) to reveal the fusion boundary, which served as the location for prepa-

TABLE 4. Different operating condition to evaluate the impact toughness of HAZ of P92 steel weldment.

S. No.	Conventional V-groove	Narrow groove
1	Charpy test at room temperature	Charpy test at room temperature
2	Hot Charpy test at 760°C	Hot Charpy test at 760°C
3	Charpy test at room temperature after PWHT at 760°C for 2 h	Charpy test at room temperature after PWHT at 760°C for 2 h
4	Hot Charpy test at 760°C after PWHT at 760°C for 2 h	Hot Charpy test at 760°C after PWHT at 760°C for 2 h

ration of notches as shown in Fig. 3. The different operating conditions considered for Charpy toughness testing of HAZ of P92 steel weldments are stated in Table 4. Charpy toughness tests were also conducted to study the effect of post-weld heating at 280°C for 40 min and 60 min just after welding on the impact toughness of P91 weld fusion zone and HAZ. To study the effect of subsequent PWHT and PWNT heat treatment on tensile properties of different weld groove designs, round subsize tensile-test specimens were prepared as per to ASTM E8-E8M-13a [20] standards with a gauge diameter of 6 mm.

3. RESULTS

3.1. As-Received Materials and Microstructure

The microstructure of weld fusion zone and FGHAZ in as welded condition are presented in Fig. 4, *a*, *b*. The weld fusion zone is characterized with columnar laths in packets form with similar spatial orientation inside the PAGBs with almost negligible precipitates, as shown in Fig. 4, *a*. The precipitates are dissolved at such high temperature and increase the carbon (C) percentage in martensite that makes it brittle with high strength and poor toughness. The heterogeneous microstructure mainly occurred among weld fusion zone, ICHAZ and FGHAZ. In P92 weldments, it is quite difficult to distinguish the FGHAZ and IC-HAZ. The most common type IV failure of P92 weldments are initiated from FGHAZ or IC-HAZ because of soft zone (low hardness). The FGHAZ are partially austenitized during weld thermal cycle because of low temperature as compared to weld fusion zone and CGHAZ. FGHAZ shows a complex structure of newly formed grain and existing grains with coarse undissolved $M_{23}C_6$ precipitates, as shown in Fig. 4, *b*.

After the PWHT, secondary electron micrograph of weld fusion zone and FGHAZ are shown in Fig. 4, *c*, *d*.

In weld fusion zone, a number of particles re-precipitated along the boundaries and inside the matrix region. The columnar laths mainly braked into equiaxed lath and tempered martensitic microstructure along with precipitates have been observed. The size of lath width was measured in the range of 3.74–4.68 μm, as shown in Fig. 4, *c*. The grain coarsening was clearly noticed in the FGHAZ after the PWHT. After

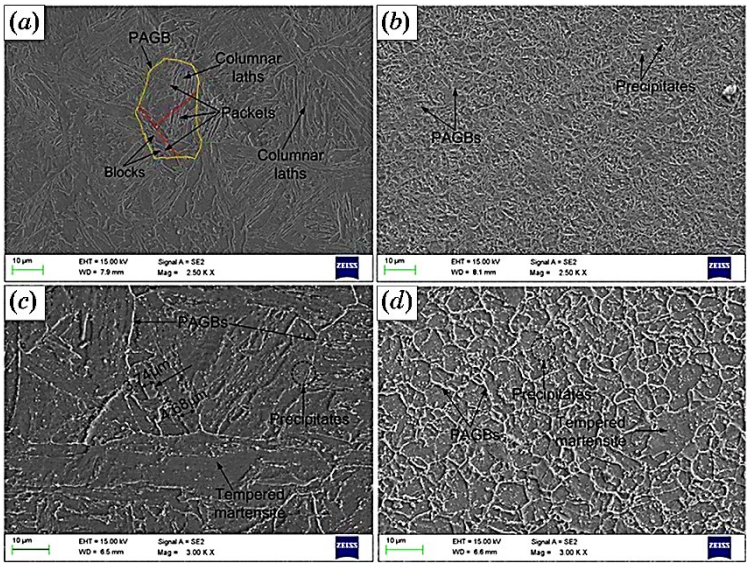

Fig. 4. Microstructure of weld fusion zone and FGHAZ in as-welded condition (*a*) and (*b*); microstructure after the PWHT for weld fusion zone and FAHAZ (*c*) and (*d*).

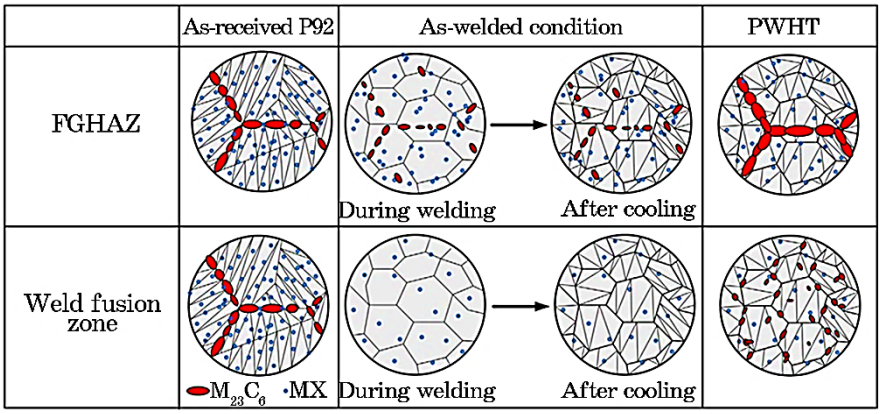

Fig. 5. Characteristic of microstructure in weld zone and FGHAZ in as-welded and PWHT condition.

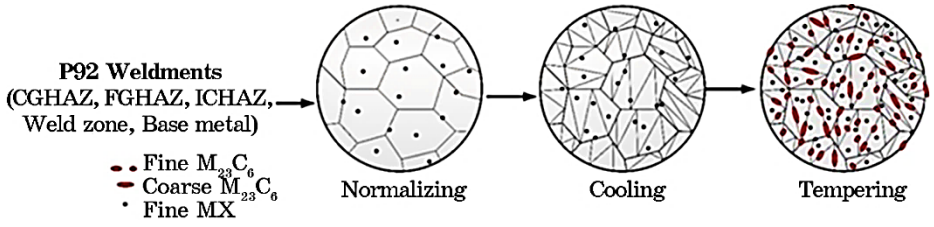

Fig. 6. Schematic of microstructure evolution in subzone of P92 weldments during PWNT treatment.

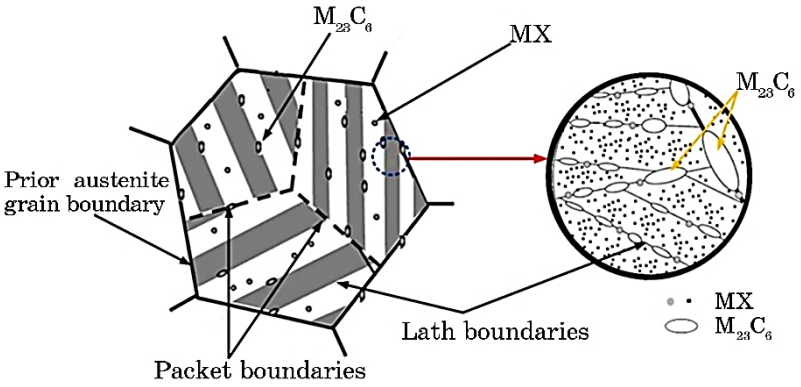

Fig. 7. Schematic evolution of $M_{23}C_6$ and MX precipitates.

PWHT, coarse undissolved $M_{23}C_6$ and newly developed fine MX and $M_{23}C_6$ precipitates are observed in FGHAZ. The PWHT results in the tempered martensitic structure formation with coarse and fine precipitates along the boundaries and grain interior region.

The schematic diagram showing the microstructure evolution in as-welded and PWHT state of weld fusion zone and FGHAZ is depicted in Fig. 5.

After the study of the effect of PWHT, an attempt has been made to perform a comparative study between subsequent PWHT and PWNT heat treatment. In normalizing condition, various zones can be treated as the normalized base metal. Tempering after the normalizing results in the evolution of precipitates along the PAGBs, lath boundaries, packets and inside the intralath region. The subzone of P92 weldments can be treated as the virgin P92 steel.

Schematic of PWNT treatment process and their effect on microstructure evolution is shown in Fig. 6. The study was related to the effect of PWNT heat treatment on microstructure evolution, residual hardness, Charpy toughness and tensile properties of P92 weldment and these results were compared to that of subcritical PWHT.

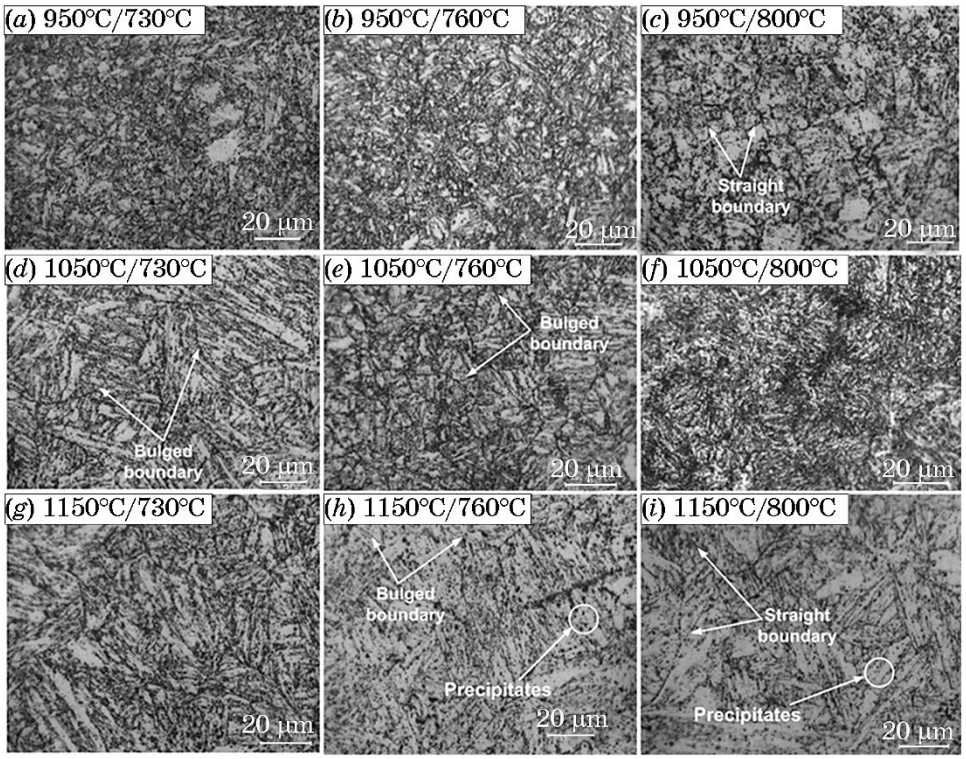

Fig. 8. Optical micrographs of weld fusion zone for different normalized and tempered conditions (*a*) 950°C/730°C, (*b*) 950°C/760°C, (*c*) 950°C/800°C, (*d*) 1050°C/730°C, (*e*) 1050°C/760°C, (*f*) 1050°C/800°C, (*g*) 1150°C/730°C, (*h*) 1150°C/760°C, (*i*) 1150°C/800°C.

Figure 7 shows the schematic diagram of PAGBs, lath boundaries, packet boundaries, lath blocks and precipitates evolution along the boundaries and lath blocks. From Fig. 7, it is clear that the coarse $M_{23}C_6$ precipitates are formed along the PAGBS and lath boundaries while MX precipitates inside the intra-lath region. Hence, area fraction of precipitates mainly depends on the availability of grain boundaries in the microstructure.

3.2. Microstructure Evolution in Weld Zone and FGHAZ for Varying PWNT Conditions

The microstructure of weld fusion zone for different normalized and tempered condition is depicted in Fig. 8, *a*–*i*. The bulged grain boundary at low tempering temperature and straight boundary at higher tempering temperature are shown in Fig. 8, *h* and Fig. 8, *i*. For higher

normalizing and lower tempering temperature, less fraction area of precipitates makes the grain boundaries free from pinning effect that resulted in bulging of the grain boundary. For lower normalizing and higher tempering temperature, the availability of a large number of grain boundaries led to higher fraction area of precipitates. This results in restriction of grain boundary movement leading to straight boundary formation.

The optical micrographs of the fine-grained heat-affected zone (FGHAZ) are shown in Fig. 9, *a–i*. In FGHAZ, the similar pattern of grain structure was noticed as obtained for the weld fusion zone. The grain size is observed to increase with an increase in normalizing temperature (fixed tempering temperature) and decrease with increase in tempering temperature (fixed normalizing temperature), as shown in Fig. 10, *a*. For a normalizing temperature of 1150°C, bigger size grain boundaries are clearly seen in Fig. 9, *h–i*. The microstructure of FGHAZ is characterized by the presence of tempered martensite,

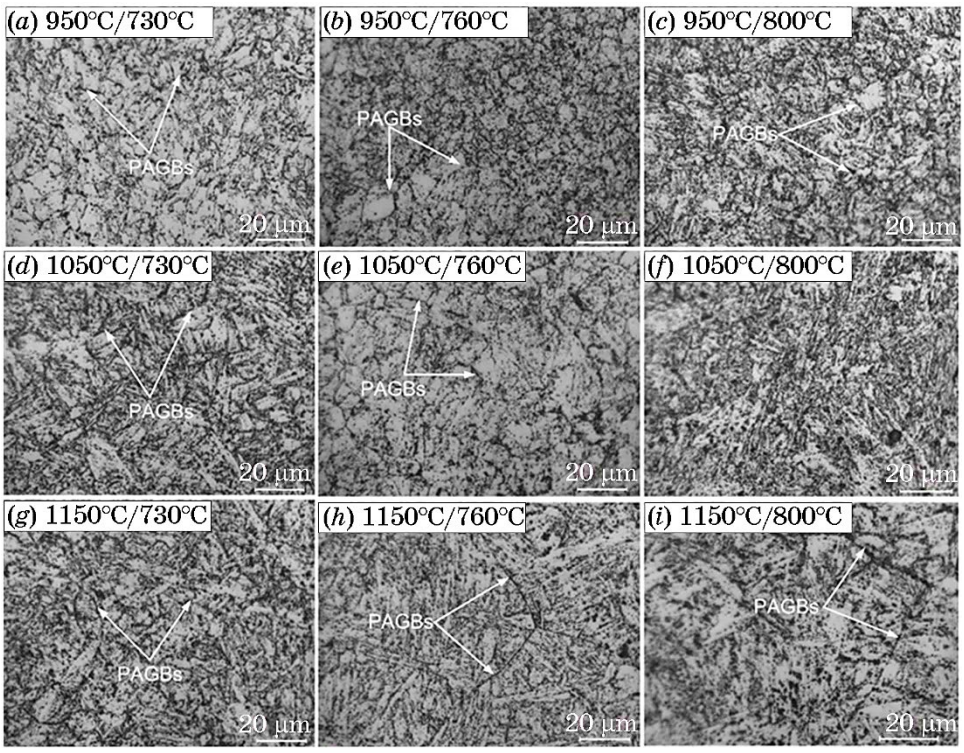

Fig. 9. Optical micrographs of fine-grained heat affected zone for different normalized and tempered conditions (*a*) 950°C/730°C, (*b*) 950°C/760°C, (*c*) 950°C/800°C, (*d*) 1050°C/730°C, (*e*) 1050°C/760°C, (*f*) 1050°C/800°C, (*g*) 1150°C/730°C, (*h*) 1150°C/760°C, (*i*) 1150°C/800°C.

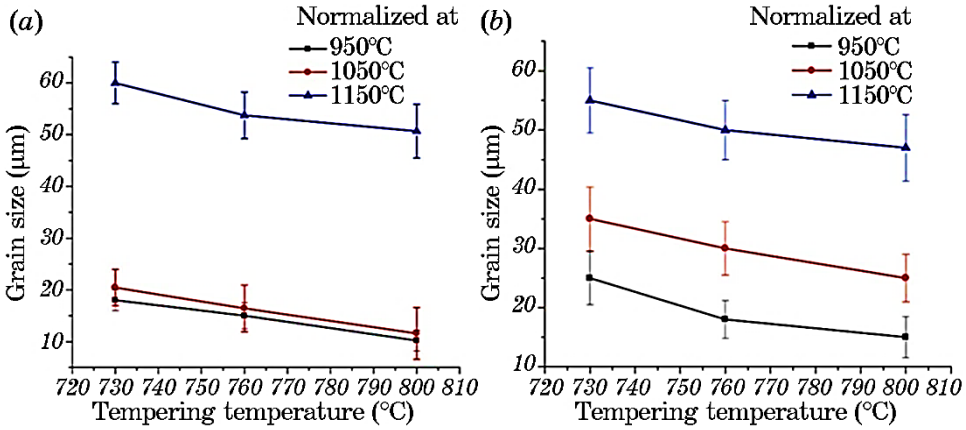

Fig. 10. Variation in grain size with normalizing and tempering temperature (*a*) FGHAZ and (*b*) over-tempered base metal zone.

PAGBs, lath boundaries and packets with $M_{23}C_6$ precipitates along the grain boundaries. The subgrain boundaries are clearly seen in optical micrographs.

The variation in grain size of FGHAZ and over-tempered base zone (OTB) is shown in Fig. 10. For FGHAZ, the grain size increased with an increase in normalizing temperature for a fixed tempering temperature. The grain size decreased with increase in tempering temperature for fixed normalizing temperature. This similar pattern was also observed for the OTB. In FGHAZ, for fixed tempering temperature a negligible change in grain size was observed after increasing the normalizing temperature from 950°C to 1050°C, while a drastic increase was observed after normalizing beyond 1050°C. Grain size plays an important role in determining the strength, hardness and precipitate size distribution. Presence of coarse grain (1150°C/730°C) leads to less availability of grain boundaries, *i.e.*, less fraction area of precipitates. Barbadikar *et al.* [21] had reported that less fraction area of precipitates resulted in the higher availability of C and N in solution matrix that led to solid solution strengthening and ultimately higher strength and hardness.

Secondary electron (SEM) micrograph of weld fusion zones for different normalizing & tempering condition is shown in Fig. 11, *a*–*i*. The distribution of precipitates is clearly seen in SEM micrograph. At low normalizing temperature range (950–1050°C), equiaxed lath morphology is observed while at a higher normalizing temperature of 1150°C lath morphology is observed, and it became difficult to trace the PAGBs. The lath boundaries and packets are clearly seen at a normalizing temperature of 1150°C.

The microstructure of FGHAZ for the different PWNT conditions is

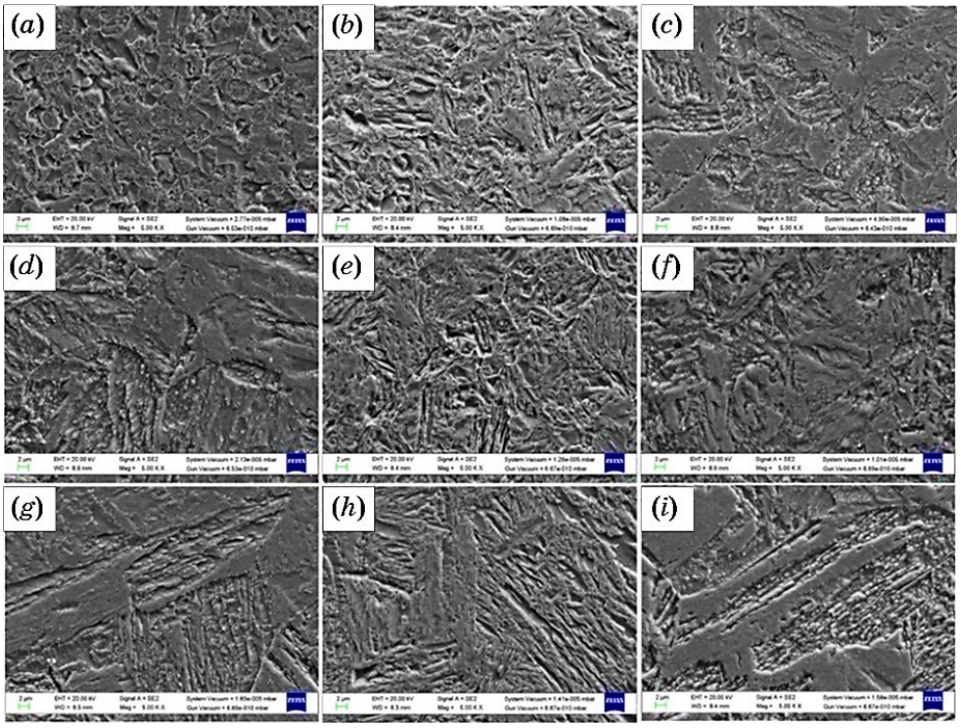

Fig. 11. Secondary electron micrographs of weld fusion zone for different normalized and tempered conditions (*a*) 950°C/730°C, (*b*) 950°C/760°C, (*c*) 950°C/800°C, (*d*) 1050°C/730°C, (*e*) 1050°C/760°C, (*f*) 1050°C/800°C, (*g*) 1150°C/730°C, (*h*) 1150°C/760°C, (*i*) 1150°C/800°C.

shown in Fig. 12, *a–i*. For a low normalizing temperature of 950°C, the microstructure looks similar for each tempering condition except the grain coarsening. For normalizing & tempering of 1050°C/800°C, the microstructure looks different and typical columnar lath morphology is seen, as shown in Fig. 12, *f*. For PWNT of 1150°C/730°C, due to high coarsening rate, the PAGBs disappear and only lath boundaries are observed. With the increase in tempering temperature for a fixed normalizing temperature, continuous reduction in grain size of FGHAZ was predicted (Fig. 10). Due to smaller grain size, the PAGBs are clearly seen in Fig. 12, *a–f*. Initially, the microstructure of weld fusion zone and FGHAZ looks similar up to normalizing & tempering of 1050°C/760°C, after that a drastic change was noticed in the microstructure in terms of PAGBs, lath boundaries and precipitate distribution. At a higher normalizing temperature of 1150°C, columnar lath morphology is clearly seen in micrographs.

The size and distribution of precipitates in FGHAZ were also measured for all the normalizing & tempering conditions, and it is shown in

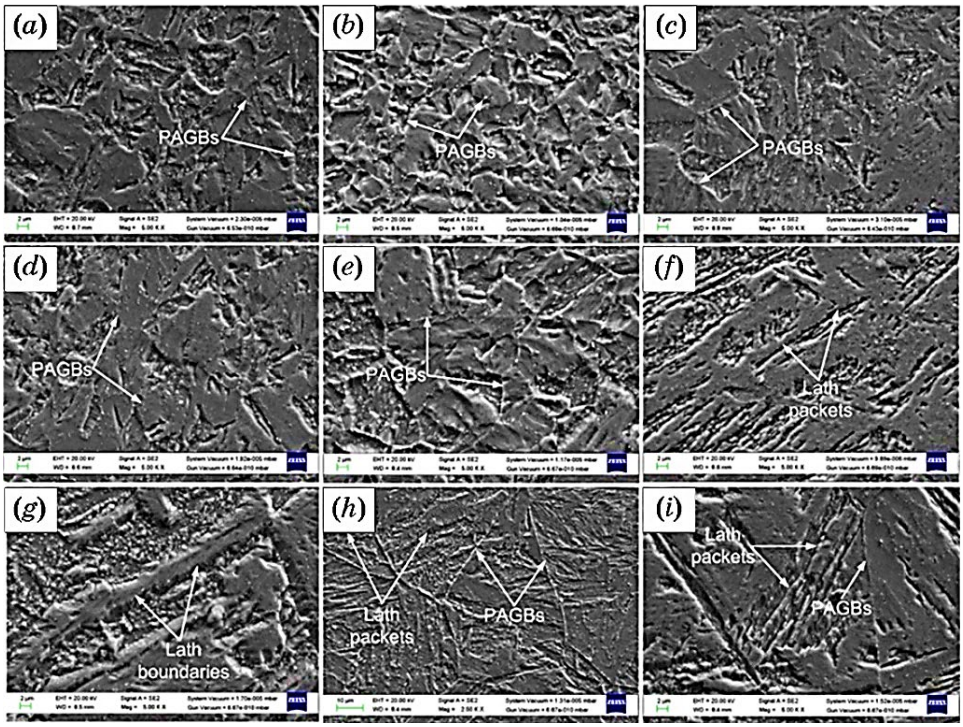

Fig. 12. Secondary electron micrographs of fine-grained heat affected zone for different normalized and tempered conditions (*a*) 950°C/730°C, (*b*) 950°C/760°C, (*c*) 950°C/800°C, (*d*) 1050°C/730°C, (*e*) 1050°C/760°C, (*f*) 1050°C/800°C, (*g*) 1150°C/730°C, (*h*) 1150°C/760°C, (*i*) 1150°C/800°C.

Fig. 13, *a*, *b* for 950°C/730°C and 1150°C/800°C condition. Coarsening of precipitates with an increase in normalizing temperature is clearly noticed in Fig. 13, *a*, *b*. At the initial stage of PWNT process, globular and spherical shape particle are observed, while, at higher PWNT process, mainly cylindrical and needle shaped particles are observed.

The variation in area fraction of precipitates for weld fusion zone and FGHAZ are shown in Fig. 14, *a*, *b*. The area fraction of precipitates increased with increase in tempering temperature (constant normalizing temperature) and decreased with increase in the normalizing temperature (constant tempering temperature) for both weld zone and FGHAZ. The less area fraction of precipitates at low tempering temperature led to the formation of the bulged boundary because of less pinning force from precipitates.

The area fraction of precipitates governs the mechanical properties due to precipitation hardening and solid solution hardening. A higher fraction of precipitates results in a considerable lowering of solid solution hardening due to less availability of C and N in solid solution ma-

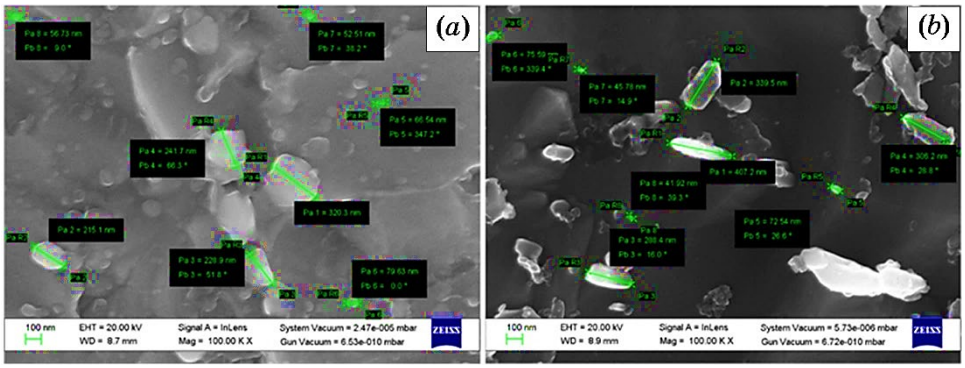

Fig. 13. Size and distribution of element in FGHAZ for different PWNT condition (*a*) 950°C/730°C, (*b*) 1150°C/800°C.

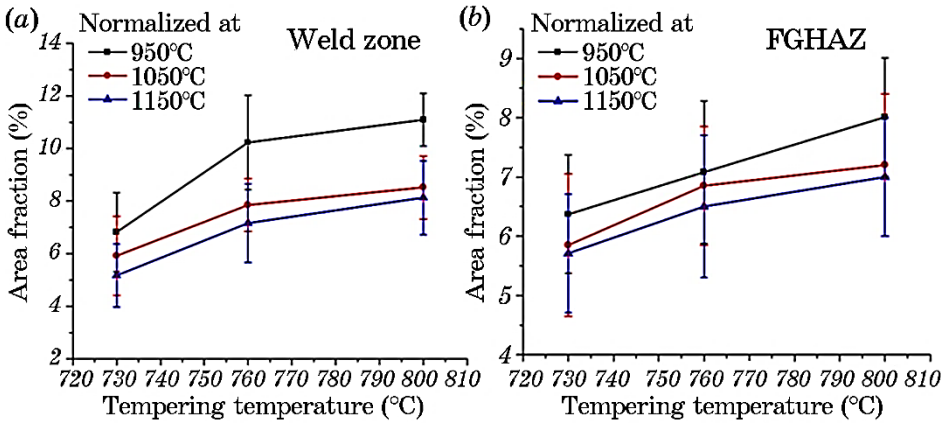

Fig. 14. Variation in area fraction of precipitates (*a*) weld fusion zone and (*b*) FGHAZ.

trix. However, higher fraction area of precipitate might leads to precipitation hardening. Generally, solid solution hardening dominates over the precipitation hardening.

3.3. Hardness Variation

The hardness of weld fusion zone and FGHAZ for different PWNT conditions is given in Table 5. The hardness value increased with increase in normalizing temperature for given tempering temperature while the hardness value decreased with increase in tempering temperature. The extent of increase in hardness in the temperature range of 1050°C–1150°C was found to be more compared to a temperature range

TABLE 5. Hardness variation in weld fusion zone and FGHAZ for different normalizing and tempering condition.

Heat treated condition	Hardness (*HV*)		Heat treated condition	Hardness (*HV*)		Heat treated condition	Hardness (*HV*)	
	Weld zone	FGHAZ		Weld zone	FGHAZ		Weld zone	FGHAZ
950°C/730°C	235 ± 3	235 ± 3	1050°C/730°C	237 ± 2	233 ± 2	1150°C/730°C	238 ± 3	235 ± 3
950°C/760°C	230 ± 3	229 ± 5	1050°C/760°C	232 ± 3	228 ± 4	1150°C/760°C	235 ± 3	231 ± 2
950°C/800°C	232 ± 3	231 ± 3	1050°C/800°C	239 ± 3	233 ± 3	1150°C/800°C	247 ± 2	237 ± 2

of 950°C–1050°. The lower hardness in the temperature range of 950°C–1050°C is attributed to the presence of higher grain boundaries and large fraction area of precipitates. For a normalizing temperature of 1150°C, coarse grain size led to lower precipitation of $M_{23}C_6$ and MX precipitates and ultimately larger presence of carbon and nitrogen in solution matrix that resulted in higher solid solution hardening. Lower precipitate formation resulted in reduced precipitation hardening. Grain coarsening might also lead to poor hardness but higher solid solution hardening dominate over the reduction in precipitation hardening and grain coarsening. This resulted in an increase in hardness value at higher normalizing temperature compared to lower normalizing temperature.

3.4. Tensile Properties

For V-grove and narrow groove weld design, transverse tensile test specimens were tested. The gauge length and width of the flat tensile specimen were 25 mm and 6.25 mm, respectively. For transverse tensile tested specimen, variation in ultimate tensile strength (UTS) and yield strength (YS) with normalizing and tempering are depicted in Fig. 15, *a–d*. In each test, the fracture location was noticed in the OTB. For a fixed tempering temperature, the YS and UTS were increased with an increase in normalizing temperature for both the groove designs. For V-groove design, UTS increased from 705 MPa to 730 MPa with an increase in normalizing temperature from 950°C to 1150°C (tempering temperature 730°C), while, for narrow groove design, it increased from 683 MPa to 712 MPa. The minimum UTS and YS were measured for sample normalized at 950°C and tempered at 800°C for both groove designs. The sample normalized at 1150°C led to coarse grain and higher lath width. This resulted in less availability of grains

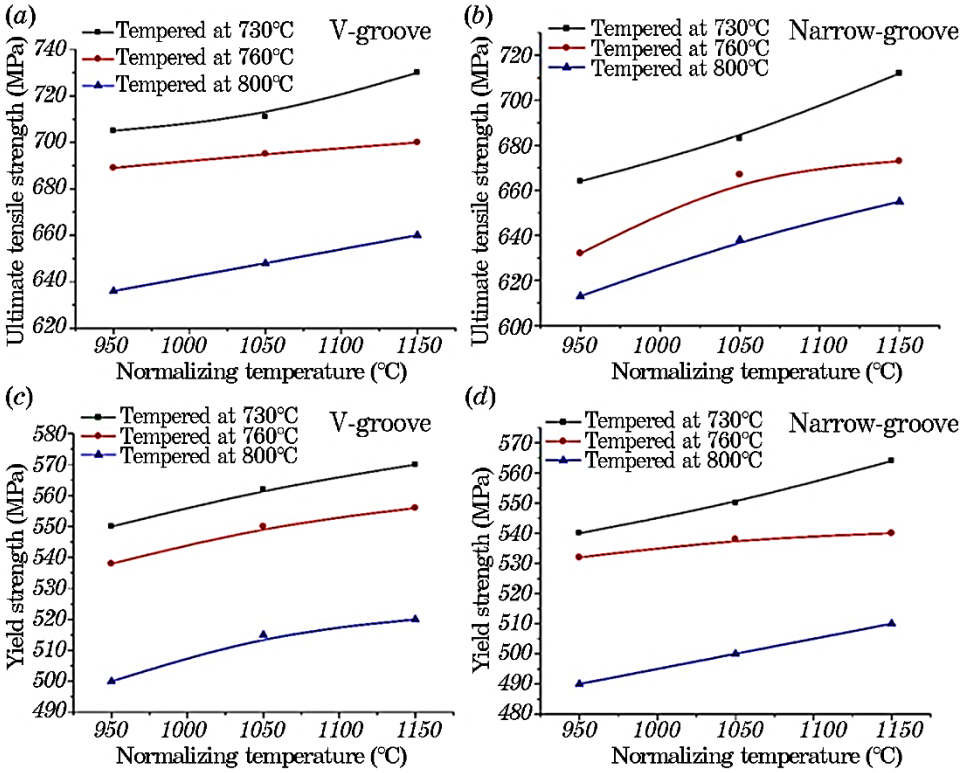

Fig. 15. Variation in tensile properties for V-groove and narrow-groove design with varying normalizing and tempering temperature: (*a*), (*b*) UTS; (*c*), (*d*) YS.

and grain boundaries per unit area and reduced the fraction area of precipitates. The lower availability of carbide precipitates led to solid solution strengthening and resulting in an increase in strength of steel for sample normalized at 1150°C compared to the sample normalized at 950°C and 1050°C. For narrow groove design, similar behaviour was noticed in UTS and YS variation. However, the UTS and YS measured for the narrow groove weld design was found to be less corresponding to V-groove designs.

For a given normalizing temperature, the YS and UTS decreased with increase in tempering temperature. For V-groove design and fixed normalizing temperature of 1150°C, the maximum UTS and YS were measured to be 730 MPa and 570 MPa respectively for tempering temperature of 730°C, while minimum UTS and YS were measured to be 660 MPa and 520 MPa respectively for tempering temperature of 800°C. For V-groove design, the rate of decrease in UTS was found to be lower up to tempering temperature of 760°C and beyond that, a

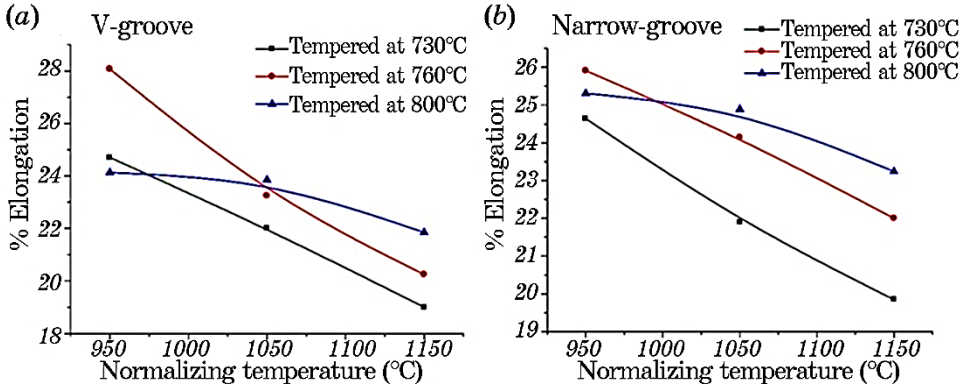

Fig. 16. Variation in % elongation (*a*) V-groove and (*b*) narrow-groove design.

drastic decrease was noticed in the UTS value. For narrow-groove design, a near uniform decreasing trend was observed for given tempering temperature range. The variation in YS and UTS value of P92 steel weldments for different PWNT conditions were strongly affected by the solid solution hardening and precipitate hardening. The coarse precipitates at higher tempering temperature were also responsible for the strength and hardness degradation. The coarse precipitates have poor tendency to act as the dislocation barrier resulting in poor strength and hardness. The increase in tempering temperature led to consumption of C and N from the matrix for higher carbide and carbonitrides precipitation. The reduction of C and N from the matrix resulted in poor solid solution hardening. The formation of precipitate might lead to precipitation hardening but the reduction in solid solution hardening dominates over the increase in precipitate hardening. This resulted in a reduction in strength value of P92 steel at higher tempering temperature. A good agreement was also observed in hardness and strength relationship.

Figures 16, *a*, *b* show the variation [in %] elongation for transverse tensile tested weld specimens in different normalizing and tempering temperature range. The percentage elongation increased with increase in tempering temperature for normalizing temperature range of 1050–1150°C. For V-groove weld design, maximum percentage elongation was measured to be 24.7% for sample normalized at 950°C and tempered at 730°C, while a minimum of 24.13% was for sample tempered at 800°C for same normalizing temperature. The similar pattern of percentage elongation was also measured for narrow-groove design as shown in Fig. 16, *b*. The percentage elongation decreased with increase in normalizing temperature. For tempering temperature of 730°C and normalizing temperature of 1150°C, the percentage elongation was observed to be less than 20% for both the groove designs.

4. CONCLUSIONS

1. The normalizing and tempering treatment, recovery processes leads to the refinement of grain structure. This resulted in higher Charpy toughness value in weld zone than as-received P92 steel.
2. The normalizing and tempering treatment of P92 weldments produced uniformed hardness measured in weld zone and the fine-grained heat affected zone was found to be very much similar to that recorded in as-received P92 steel.
3. The ultimate tensile strength and yield strength value of V-groove weld design were measured to be higher than narrow-groove design while Charpy toughness value of narrow-groove weld design was measured to be superior to V-groove weld design.
4. The final fracture zone of tensile fracture surface revealed the mixed mode of failure for all normalizing and tempering action.
5. The normalizing at 1050°C and 760°C is recommended for P92 weldments for the optimum combination of strength and ductility.

REFERENCES

1. S. L. Mannan, S. C. Chetal, B. Raj, and S. B. Bhoje, *Trans. Indian Inst. Met.*, **35**: 1 (2003).
2. C. Pandey, M. M. Mahapatra, P. Kumar, and N. Saini, *J. Nucl. Mater.*, **498**: 176 (2018).
3. K. L. Murty and I. Charit, *J. Nucl. Mater.*, **383**: 189 (2008).
4. M. Marietta and E. Systems, Ornl/tm—9045 de85 012618 (1984).
5. C. Pandey and M. M. Mahapatra, *J. Mater. Eng. Perform.*, **25**: 2761 (2016).
6. M. E. Abd El-Azim, O. E. El-Desoky, H. Ruoff, F. Kauffmann, and E. Roos, *Mater. Sci. Technol.*, **29**: 1027 (2013).
7. K. Laha, K. S. Chandravathi, P. Parameswaran, K. B. S. Rao, and S. L. Mannan, *Metall. Mater. Trans. A*, **38**: 58 (2007).
8. K. Maruyama, K. Sawada, and J. Koike, *ISIJ Int.*, **41**: 641 (2001).
9. H. K. Danielsen and J. Hald, *Comput. Coupling Phase Diagrams Thermochem.*, **31**: 505 (2007).
10. H. K. Danielsen and J. Hald, *Mater. Sci. Eng. A*, **505**: 169 (2009).
11. M. Abd El-Rahman Abd El-Salam, I. El-Mahallawi, and M. R. El-Koussy, *Int. Heat Treat. Surf. Eng.*, **7**: 23 (2013).
12. V. L. Manugula, K. V. Rajulapati, G. M. Reddy, and K. B. S. Rao, *Mater. Sci. Eng. A*, **698**: 36 (2017).
13. S. K. Albert, M. Matsui, T. Watanabe, H. Hongo, K. Kubo, and M. Tabuchi, *Int. J. Press. Vessel. Pip.*, **80**: 405 (2003).
14. K. Sawada, M. Bauer, F. Kauffmann, P. Mayr, and A. Klenk, *Mater. Sci. Eng. A*, **527**: 1417 (2010).
15. J. A. Francis, W. Mazur, and H. K. D. H. Bhadeshia, *ISIJ Int.*, **44**: 1966 (2004).
16. D. Dean and M. Hidekazu, *Comput. Mater. Sci.*, **37**: 209 (2006).
17. F. William and Jr. Newell, *Weld. J.*, **89**: 33 (2010).

18. M. L. Santella, R. W. Swindeman, R. W. Reed, and J. M. Tanzosh, *EPRI Conf. 9Cr Mater. Fabr. Join. Technol.* (2001).
19. ASTM A370–14, *Standard Test Methods and Definitions for Mechanical Testing of Steel Products* (2014).
20. ASTM E8/E8M–13a, *Standard Test Methods for Tension Testing of Metallic Materials* (2009).
21. D. R. Barbadikar, G. S. Deshmukh, L. Maddi, K. Laha, P. Parameswaran, A. R. Ballal, D. R. Peshwe, R. K. Paretkar, M. Nandagopal, and M. D. Mathew, *Int. J. Press. Vessel. Pip.*, **132–133**: 97–105 (2015).

Metallophysics and Advanced Technologies
Металофіз. новітні технол.
Metallofiz. Noveishie Tekhnol.
2024, vol. 46, No. 5, pp. 453–465
https://doi.org/10.15407/mfint.46.05.0453
Reprints available directly from the publisher

PACS numbers: 07.05.Fb, 62.20.Qp, 68.37.Hk, 81.05.ue, 81.40.Pq, 82.80.Ej

Optimization of Multiresponse Process Parameters in Friction Stir Processing of AA6063/*n*-Graphene Composites by Taguchi's Grey Relational Analysis

E. Jenson Joseph, D. Muthukrishnan[*], G. R. Raghav, K. J. Nagarajan[**], and R. Ashok Kumar[***]

SCMS School of Engineering and Technology,
Vidya Nagar, Palissery, Karukutty, Ernakulam,
683582 Kerala, India
[*]*K.L.N. College of Engineering,*
630612 Pottapalayam, Sivagangai District,
Tamil Nadu, India
[**]*Thiagarajar College of Engineering,*
TCE Avaniyapuram Road,
625015 Madurai, Tamil Nadu, India
[***]*SRM Madurai College for Engineering & Technology,*
Nedungulam Main Road,
630611 Madurai, Tamil Nadu, India

The aim of this study is to focus on the multiresponse-process optimization of friction stir processing of AA6063/*n*-graphene-based surface composites to obtain enhanced mechanical properties using Taguchi's technique combined with grey relational analysis (GRA) technique. The parameters of the process selected for this study are tool rotation speed (rpm), tool traverse speed (mm/min), and tilt angle (°). Commonly followed mechanical characterization, namely, hardness and tensile strength are considered as the output performances. The experiments are conducted with a minimal run designed by Taguchi's L_9 orthogonal array factorial design of experiments. GRA is used to optimize the multiresponse-process parameters. In accordance with the analysis, it is found that the specimen synthesized with the tool rotation

Corresponding author: E. Jenson Joseph
E-mail: jenson@scmsgroup.org

Citation: E. Jenson Joseph, D. Muthukrishnan, G. R. Raghav, K. J. Nagarajan, and R. Ashok Kumar, Optimization of Multi Response Process Parameters in Friction Stir Processing of AA6063/*n*-Graphene Composites by Taguchi's Grey Relational Analysis, *Metallofiz. Noveishie Tekhnol.*, **46**, No. 5: 453–465 (2024).
DOI: 10.15407/mfint.46.05.0453

speed of 1200 rpm, traverse speed of 40 mm/min, and 1.5° tilt angle exhibits superior mechanical properties. Analysis of the variance is done to study the dominant factor affecting the strength of the processed composites. SEM analysis with EDX spectrum is done to study the morphological characterization of the prepared composites.

Key words: surface composites, Taguchi's grey relational analysis, friction stir processing, AA6063, *n*-graphene.

Метою даної роботи було проведення оптимізації процесу оброблення тертям з перемішуванням поверхневих композитів на основі AA6063/*n*-графену для одержання поліпшених механічних властивостей за допомогою методики Тагучі в поєднанні з сірою реляційною аналізою (СРА). Параметрами процесу, обраними для цього дослідження, є швидкість обертання інструменту (об./хв.), швидкість переміщення інструменту (мм/хв.) і кут нахилу (°). Загальновідомі механічні характеристики, а саме, твердість і міцність на розрив, вважаються вихідними характеристиками. Експерименти проводилися для мінімальної серії, розробленої за факторіяльною схемою ортогональної матриці Тагучі L_9. СРА використовувалася для оптимізації параметрів процесу з багаторазовим відгуком. Встановлено, що зразок, синтезований зі швидкістю обертання інструменту у 1200 об./хв., швидкістю ходу у 40 мм/хв. і кутом нахилу у 1,5°, демонструє виняткові механічні властивості. Дисперсійну аналізу виконано для вивчення домінувального чинника, що впливає на міцність оброблених композитів. Аналіза скануваною електронною мікроскопією із енергодиперсійним рентґенівським спектром проводиться для вивчення морфологічних характеристик одержаних композитів.

Ключові слова: поверхневі композити, сіра реляційна аналіза за Тагучі, оброблення тертям, AA6063, *n*-графен.

(Received 10 October, 2023; in final version, 10 December, 2023)

1. INTRODUCTION

Aluminium alloys gained much industrial significance due to their unique lightweight properties. Many industries especially automotive and aerospace are concerned the curb weight of the product is a critical factor deciding the fuel efficiency and it could be resolved by employing such lightweight alloys. Composites made of aluminium alloy have significant applications in automobile fields and aerospace due to its lightweight, lesser wear rates, and other enhanced mechanical and thermal properties as compared to the virgin materials [1–8].

Composites based on aluminium matrix can be useful only if it is reinforced with suitable materials that will enhance its properties. Among all the other reinforcements are considered, the carbon-rich reinforcements like carbon nanotubes, graphite, and graphene have unique electrical, mechanical, and thermal properties. Researchers gain the ad-

vantage of the lubricous nature of such carbon materials and taken efforts to synthesize self-lubricating lesser-weight composites that will withstand extreme wear and tear and hence these materials could be employed in automotive and aerospace industries [9–13]. Among these carbon reinforcements, graphene is found to have a cutting-edge advantage over the other materials because to its outstanding optical, mechanical, electrical and thermal properties for varied potential applications. In addition, the honeycomb lattice of single sheet structure in graphene found it to be superior to the other materials [14–16]. Further, the high mechanical strength and high modulus of graphene have gained significant attention in the fabrication of composites.

There are many traditional methods like melting and solidification for fabricating metal matrix composites. However, there are challenges in using the melting and solidification technique for fabricating graphene-reinforced composites. However, graphene has a large surface area, with a lower mass density, which leads to agglomeration during fabrication, and is destroyed by molten metals upon melting. Thus, in order to improve the dispersion of graphene particles, solid-state stirring has been used to fabricate the composite plates.

In the fabrication of aluminium matrix composites, the fabrication methods play a vital role in establishing bonding strength between matrix medium and reinforcement. Hence, selection of fabrication methods is extremely important in determining the mechanical strength of the developed composites. Several fabrication methods are available in the literatures for developing aluminium matrix composites. In recent days, eco-friendly fabrication techniques such as friction stir processing (FSP) have gained much attention among researchers in developing aluminium matrix composites. In FSP, process parameters selection plays a critical role in determining the mechanical strength of the developed composites. The main parameters involved in FSP are tool rotation speed, traverse speed, tool profile and axial load. The impact of these parameters critically affects the properties of metal matrix composites as reported by researchers [12, 17].

The effect of process parameters, on the properties of the developed composites, could be studied by applying a suitable multiresponse optimization tool. The grey relational analysis (GRA) is a suitable multiresponse optimization tool. Aydin *et al.* [18] studied the impact of process parameters on friction welding of AA1050 plates and optimised the process responses using the Taguchi-based GRA. Many researchers used the parametric conventional time-consuming technique where one of the parameters will be varied and all other parameters are kept constant. Hence, to analyse the impact of these parameters by limiting the numbers of experiment runs, a statistical-technique for Taguchi design of experiments could be used. Taguchi's S/N and orthogonal array (OA) are very popular and mostly used for optimization of single response

factor.

Recently, the Taguchi methodology has been integrated with grey relational analysis to solve multiresponse-optimization problems as in the case of friction welding and friction stir processes. Studies conducted by Sureshet *et al.* [19] analysed the effect of tool pin profiles in friction stir welding using Taguchi analysis method, and found that tool rotation speed has more impact on the tensile strength as compared to welding speed and plunging depth.

Pravinet *et al.* [20] investigated the effect of processing parameters on yield strength and tensile strength of friction stir processing of AA606I aluminium alloys and found that titanium carbide shows superior quality of welding at the tool rotation speed of 1500 rpm, tool traverse speed of 25 mm/s and with a square pin profile. Using the Taguchi L_{16} orthogonal design, Koilraj *et al.* [17] conducted FSW studies to optimize process parameters such as tool transverse speed, tool pin shape, rotational speed and D/d ratio.

Vijayan *et al.* [21] investigated the optimization of the FSW process parameters for AA5083 using a L_9 orthogonal array with multiple responses and studied the effect of welding parameters on tensile strength and power with using Taguchi grey relational techniques. Jenson *et al.* [22] used Taguchi combined with grey relational analysis to study the wear characteristics of high-density polyethylene composites with tungsten reinforcement and found that filler content is the dominant factor affecting the wear characteristics of the composites. Hence, Taguchi combined with grey relational analysis will be the suitable tool for the optimization of multiresponse problems.

In this present research, nanographene particles are reinforced into the AA 6063 alloy to form the composite layer. DOE was applied to investigate the effect of process parameters on the mechanical characteristics of the AA6063/n-graphene composites fabricated by friction stir processing. An orthogonal array of L_9 is adopted to find out the impact of process parameters, namely, tool rotational speed, tool traverse speed (mm/min) and tool tilt angle (°) on the hardness and tensile behaviour of AA6063/nanographene composites.

2. MATERIALS AND METHODS

Aluminium AA6063 was selected as the matrix medium, which contains Al–Si–Mg as major composition. The chemical composition of

TABLE 1. Details of the chemical composition of AA6063.

Al	Si	Mg	Mn	Cu	Fe	Zn	Cr	Ni
97.68	0.68	0.88	0.20	0.014	0.30	0.03	0.05	0.007

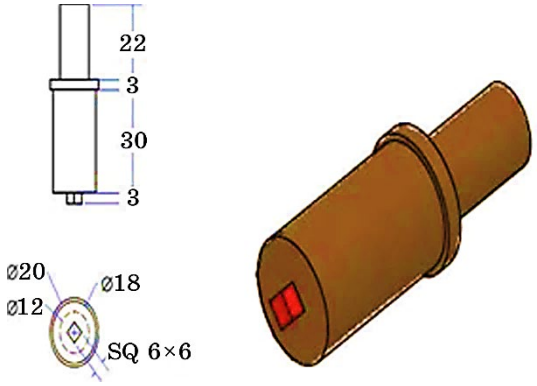

Fig. 1. FSP tool.

AA6063 is derived from XRD analysis shown in the Table 1. The matrix material AA6063 is procured as plates of 6 mm thickness. The specimens were cut by wire cut using electric discharge machining to rectangular sheets of size, 150×50×6 mm. Further, graphene particles of diameter 10 to 15 nm with 10 to 15 layers were purchased from Techinstro, PVT Ltd., Nagpur, were used as reinforcement particles. The tool was fabricated by using a surface grinding and lathe machine. The tool is made of high carbon high chromium (HCHR) of a shoulder diameter 18 mm and attached with a square pin profile of size 6×6 mm and height 3 mm was selected as FSP tool. Square grooves were machined in the centre of the AA6063 specimens (see Fig. 1). The graphene particles are then were filled in the groove. FSP experimentation was conducted using a milling machine with special attachments.

3. RESULTS AND DISCUSSIONS

3.1 Design of Experiments

Friction stir processing of materials were performed with the parameters mentioned in Table 2. Friction stir processing was done with a pinless tool to prevent powder dispersing from the groove during processing. Taguchi L_9 OA designed for this experiment is shown in the Table 3. For each parameter, the plates were rotated 180° to improve powder dispersion and prevent aggregation of powders on the advancing side. The specimens were then machined as per ASTM E8 standards for tensile strength and were tested in universal testing machine and the results are displayed in Table 3. Main effects plot of data mean *vs.* tensile strength and data means *vs.* hardness are plotted using Minitab 16.0 and the results are shown in Figs. 2 and 3.

From Figure 2, it is clear that the tensile strength increases with in-

TABLE 2. FSP parameters.

Parameters	Units	Levels			DOF
		I	II	III	
Tool rotational speed	rpm	900	1200	1500	2
Tool traverse speed	mm/min	20	30	40	2
Tilt angle	Degree	1	1.5	2	2
Total					6

TABLE 3. Experimental results for tensile strength and hardness as per Taguchi L_9 OA.

No.	Process parameters			Processing responses	
	Rotation speed, rpm	Traverse speed, mm/min	Tilt angle, °	Tensile strength, MPa	Hardness
1	900	20	1	179.5	95.7
2	900	30	1.5	183.6	95.2
3	900	40	2	187.3	92.3
4	1200	20	1.5	212.3	123.4
5	1200	30	2	203.45	124.56
6	1200	40	1	215.56	122.45
7	1500	20	2	195.56	117.8
8	1500	30	1	189.67	113.2
9	1500	40	1.5	191.23	110.5

crease in tool rotation speed till 1200 rpm, and then, it decreases and this is because with increase in tool rotation speed the heat generated also increases, which in turn melts a large pool of material and hence a better distribution is possible. Whereas beyond 1200 rpm because of this high heat generation, more metal pool is generated, and hence, the particles are freely movable and so, it will be thrown out due to centrifugal force, and they are clogged in outer area, which causes agglomeration, which causes decreases in the strength of the material.

The tensile strength decreases with the increases in traverse speed and it increases. It is because, initially at less traverse speed, the friction is minimal, and hence, the heat generated will be minimal, which is not sufficient for better distribution of particles. When the traverse speed increases, then, the heat generated also increases which in turn gives a better distribution, which increases the tensile strength. The tensile strength shows only slight variation with the change in tool tilt angle and this is because tool tilt angle do not play significant role in increasing heat generation during processing.

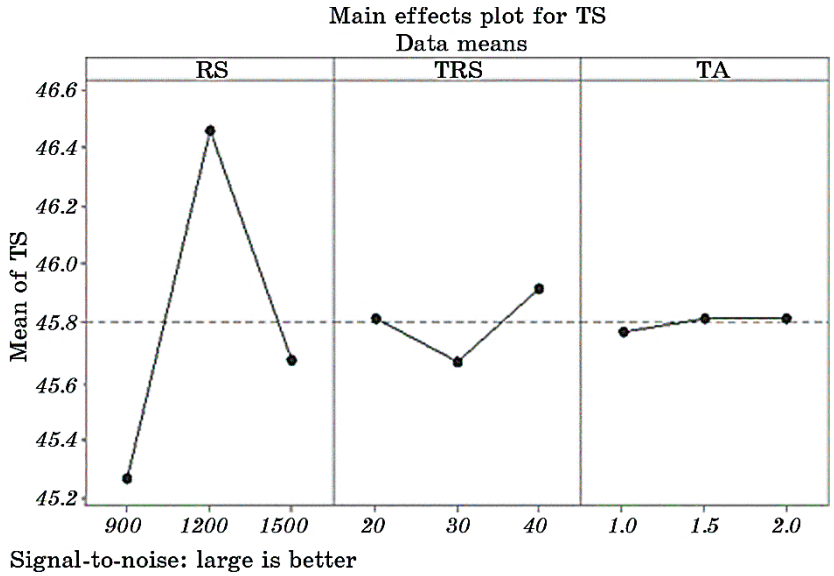

Fig. 2. Main effects plot for tensile strength.

Figure 3 shows that the hardness of the material increases with increase in tool rotation speed till 1200 rpm and beyond that the hardness decreases and it is due to the fact that hardness mainly depends on

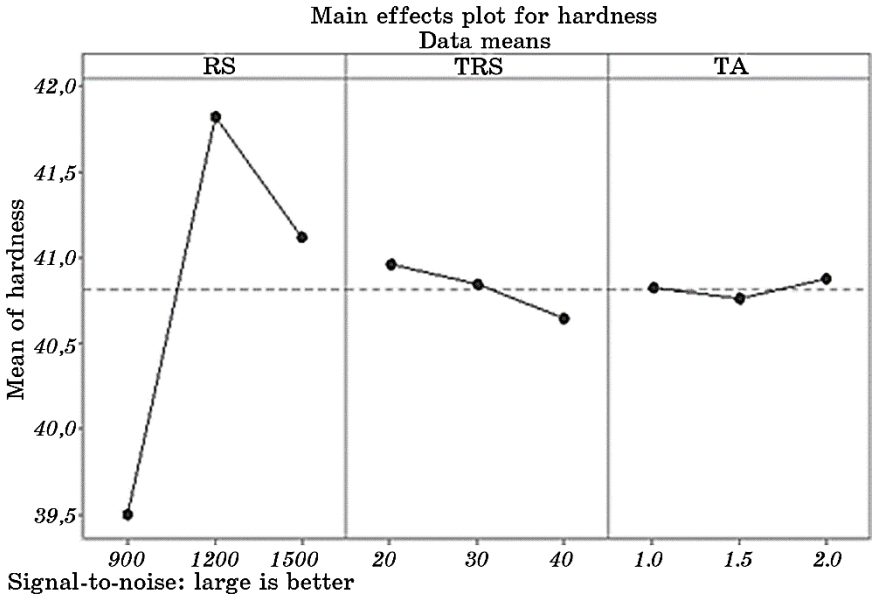

Fig. 3. The main effect plot for hardness.

uniform distribution of reinforcement in matrix medium. With increase in tool rotation speed at 1200 rpm, the distribution is uniform as shown in Fig. 3, and hence, the hardness is high. With increasing the tool rotation speed, the uniform distribution gets affected, and in turn, hardness decreases. Hardness gradually decreases with increase in tool traverse speed, and it is because traverse speed highly affects the uniform distribution of reinforcement and which in turn affects the hardness of the manufactured specimen. Hardness shows only slight variation with tool tilt angle because tool tilt angle do not have much influence on the distribution of reinforcement.

3.2. Grey Relational Analysis

Grey relational analysis is one of the most suitable tools to analyse multiresponse optimization problems. In this study, the optimization of multiple responses is mandatory and hence GRA is adopted. In GRA initially, the data is normalized between 0 and 1 using Eqs. (1) and (2):

$$X_i^* = \frac{\max x_i(k) - x_i(k)}{\max x_i(k) - \min x_i(k)}, \tag{1}$$

$$X_i^* = \frac{x_i(k) - \min x_i(k)}{\max x_i(k) - \min x_i(k)}. \tag{2}$$

Tensile strength and hardness follow the larger the better criteria, hence, Eq. (2) is applied to normalize the data. The normalized values are listed in Table 4. Then, deviation sequence is calculated for the normalized values using Eq. (3):

$$\Delta_{oi}(k) = \left| x_o^*(k) - x_i^*(k) \right|. \tag{3}$$

TABLE 4. Normalised values.

No.	Tensile strength, MPa	Hardness
1	0.000	0.105
2	0.114	0.090
3	0.216	0.000
4	0.910	0.964
5	0.664	1.000
6	1.000	0.935
7	0.445	0.790
8	0.282	0.648
9	0.325	0.564

TABLE 5. Calculated deviation sequence, GRC and GRG.

No.	Deviation sequence		GRC		GRG	RANK
Ideal sequence	Tensile strength	Hardness	Tensile strength	Hardness		
1	1.000	0.895	0.333	0.359	0.346	9
2	0.886	0.910	0.361	0.355	0.358	8
3	0.784	1.000	0.390	0.333	0.361	7
4	0.090	0.036	0.847	0.933	0.890	2
5	0.336	0.000	0.598	1.000	0.799	3
6	0.000	0.065	1.000	0.884	0.919	1
7	0.555	0.210	0.474	0.705	0.589	4
8	0.718	0.352	0.411	0.587	0.499	5
9	0.675	0.436	0.426	0.534	0.480	6

The sequence of deviation calculated using Eq. (3) is displayed in Table 5. The grey relational coefficient (GRC) depicts the relationship between reference and normalised values. GRC is calculated using Eq. (4):

$$\xi_i(k) = \frac{\Delta_{\min} + \xi\Delta_{\max}}{\Delta_{oi}(k) + \xi\Delta_{\max}}. \tag{4}$$

Grey relational grade (GRG) is the mean of GRC and can be calculated using Eq. (5). It provides information on the relationships between the sequences. The range of GRC lies between 0 and 1:

$$\gamma_i = \frac{1}{n}\sum_{k=1}^{n} \xi_i(k). \tag{5}$$

From Table 5, it is evident that experiment number 1 has the highest GRG, and therefore, the optimal sequence to obtain maximum tensile strength and hardness is $A_2B_3C_1$, *i.e.*, with tool rotation speed at 1200 rpm, tool traverse speed at 40 mm/min and tool tilt angle at 1°, it is possible to obtain maximum tensile strength and hardness of the specimen.

Average grey relational grade value for three levels is mentioned in Table 6. From Table 6, it is clear that tool rotation speed of 0.5231 is the most significant factor affecting the strength of the specimen followed by tool traverse speed of 0.0896 and tool tilt angle of 0.0394.

3.3. Analysis of Variance (ANOVA)

For GRG, the sum of squares and all other factors are listed in Table 7. It

TABLE 6. Main effects on mean GRG.

Level	Tool rotation speed (*A*)	Traverse speed (*B*)	Tilt angle (*C*)
1	0.3553	0.6248	0.6083
2	0.8784	0.5353	0.5892
3	0.5327	0.6062	0.5689
Delta	0.5231	0.0896	0.0394
Rank	1	2	3

TABLE 7. ANOVA results on grey relational grade.

Source	Degrees of freedom	Sequence sum of squares	Adjusted sum of squares	Adjusted MS	*F*-value	*P*-value	P.C., %
Tool rotation speed	2	0.424664	0.424664	0.212332	19.28	0.049	91.8
Traverse speed	2	0.013401	0.013401	0.006701	0.61	0.622	2.89
Tilt angle	2	0.002328	0.002328	0.001164	0.11	0.904	0.50
Error	2	0.022022	0.022022	0.011011			4.76
Total	8	0.462415					

is clearly evident from Table 7 that tool rotation speed has a significant contribution of 91.8% affecting the strength of the specimen. Therefore, tool rotation speed is the dominant factor affecting the strength of the specimen. The other factors have only minimal contribution.

3.4. Confirmation Experiment

The results are confirmed by conducting a confirmation test. The optimal value of the multiple factors is predicted using Eq. (6):

$$\gamma = \gamma_{\mathrm{m}} + \sum_{i=1}^{q} (\gamma_i - \gamma_{\mathrm{m}}) . \tag{6}$$

The predicted value and experimental value of GRG is displayed in Table 8. From Table 8, it is found that the predicted value is in line

TABLE 8. Confirmation experiment results.

	Predicted (A2B1C1)	Experiment (A2B1C1)
GRG	0.9341	0.9852

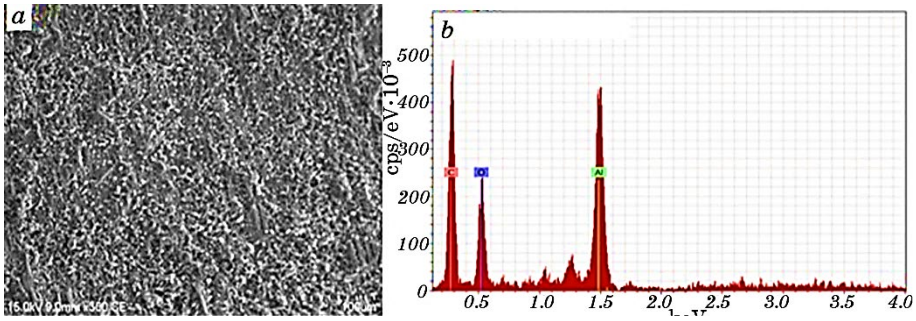

Fig. 4. SEM image (*a*) and EDX spectrum (*b*) of AA6063/*n*-graphene composite, 1200 rpm.

with the experimental value.

3.5. Microstructural Studies

The SEM images of the fabricated AA6063/*n*-graphene surface composites are shown in Fig. 4, *a*. The typical SEM images of AA6063/*n*-graphene surface composites, which are fabricated at the rotational speed of 1200 rpm, is shown in Fig. 4, *a*, which shows the uniform distribution of graphene particles in the matrix.

EDX also confirmed the existence of graphene particles, which are securely fixed within the aluminium matrix to produce a vast interface area. The secure attachment and higher uniformity of graphene particles in the matrix are thought to help the composites' tribological performance due to stress dissipation.

3.6. Microhardness Evaluation

Figure 5 displays the microhardness readings of the specimens processed (FSP) with graphene particles under different rotational speeds (900 rpm, 1200 rpm, and 1500 rpm) at a traverse speed of 20 mm/min. The microhardness of the processed zones is found to be much higher than that of the aluminium matrix AA6063, and the values are rather uniform throughout the processed zones, indicating good graphene particle dispersion in the aluminium matrix. Even though the particles are well dispersed in the matrix after two passes of FSP, the amount of increasing trend is highly minimal, while compared with base metal and processed (FSP) base metal. The value of friction stir processed specimens with particles under three different speeds (900 rpm, 1200 rpm, and 1500 rpm) attained the values of 90 *HV*, 96 *HV*, 125 *HV*, respectively.

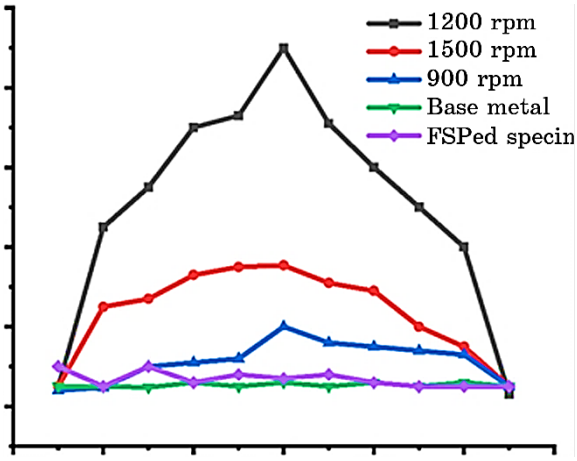

Fig. 5. Microhardness profiles.

The presence of soft graphite phase in all reinforced composites might have resulted in lower hardness values. Further, in this current investigation, processed (FSP) AA6063/nanographene composite under the rotational speed of 1200 rpm showed higher hardness, which is 50% higher than the base metal.

4. CONCLUSION

Friction stir processing of AA6063/*n*-graphene was done successfully. Based on the analysis, following conclusions are drawn. The input parameters were optimized using GRA for getting highest tensile strength and hardness of the specimen. The obtained results are summarized below.

L_9 OA was successfully combined with GRA to optimize the multiple factors.

Observation concludes that the optimal settings to obtain high tensile strength and hardness is A2–B1–C1, *i.e.*, tool rotation speed of 1200 rpm, traverse speed of 20 mm/min and tilt angle of 1° respectively.

From the ANOVA table, it was found that tool rotation is the dominant factor with 95% confidence level affecting the process followed by tool traverse speed and tool tilt angle.

Confirmation experiment shows that the predicted GRG value is in good agreement with the experimental GRG value.

EDX spectrum reveals the presence of AA6063 and *n*-graphene in the composites

SEM analysis shows uniform distribution of *n*-graphene in the matrix of AA6063.

REFERENCES

1. T. Albert, J. Sunil, A. S. Christopher, R. Jegan, P. A. Prabhu, and M. Selvaganesan, *Mater. Today Proc.*, **37**: 1558 (2021).
2. S. Gopinath, M. Prince, and G. R. Raghav, *Mater. Res. Express.*, **7**: 016582 (2020).
3. S. J. Abraham, S. C. R. Madane, I. Dinaharan, and L. J. Baruch, *J. Asian Ceram. Soc.*, **4**, Iss. 4: 381 (2016).
4. N. Karthikeyan, B. R. Krishnan, A. Vembathu Rajesh, and V. Vijayan, *Mater. Today Proc.*, **37**: 2770 (2021).
5. G. Kasirajan, Sathish Rengarajan, R. Ashok Kumar, G. R. Raghav, V. S. Rao, and K. J. Nagarajan, *Met. Res. Technol.*, **117**, No. 4: 405 (2020).
6. F. Khodabakhshi, S. M. Arab, P. Švec, and A. P. Gerlich, *Mater. Charact.*, **132**: 92 (2017).
7. V. Msomi, S. Mabuwa, O. Muribwathoho, and S. S. Motshwanedi, *Mater. Today Proc.*, **46**: 638 (2021).
8. Z. Y. Ma, *Metall. Mater. Trans. A*, **39**: 642 (2008).
9. V. Khanna, V. Kumar, and S. A. Bansal, *Mater. Res. Bull.*, **138**: 111224 (2021).
10. S. M. A. K. Mohammed, D. L. Chen, Z. Y. Liu, D. R. Ni, Q. Z. Wang, B. L. Xiao, and Z. Y. Ma, *Mater. Sci. Eng. A*, **817**: 141370 (2021).
11. K. G. Thirugnanasambantham, T. Sankaramoorthy, M. Vaysakh, S. Y. Nadish, and D. Nilesh Sabarinath, *Mater. Today Proc.*, **45**: 2606 (2021).
12. M. Wang, Y. Li, B. Chen, D. Shi, J. Umeda, K. Kondoh, and J. Shen, *Mater. Sci. Eng. A*, **808**: 140893 (2021).
13. V. S. Aigbodion, *Chem. Data Collect.*, **33**: 100707 (2021).
14. A. Radha and K. R. Vijayakumar, *Mater. Today Proc.*, **3**: 2247 (2016).
15. S. Stankovich, D. A. Dikin, G. H. B. Dommett, K. M. Kohlhaas, E. J. Zimney, E. A. Stach, R. D. Piner, S. T. Nguyen, and R. S. Ruoff, *Nature*, **442**: 282 (2006).
16. R. Sadri, M. Hosseini, S. N. Kazi, S. Bagheri, S. M. Ahmed, G. Ahmadi, N. Zubir, M. Sayuti, and M. Dahari, *Energy Convers. Manag.*, **150**: 26 (2017).
17. M. Koilraj, V. Sundareswaran, S. Vijayan, and S. R. Koteswara Rao, *Mater. Des.*, **42**: 1 (2012).
18. H. Aydin, A. Bayram, U. Esme, Y. Kazancoglu, and O. Guven, *Mater. Tehnol.*, **44**, No. 4: 205 (2010).
19. S. Ko, H. Park, Y.-H. Lee, S. Shin, I. Jo, J. Kim, S.-B. Lee, Y. Kim, S.-K. Lee, and S. Cho, *Mater.*, **13**, Iss. 7: 1588 (2020).
20. T. Pravin, C. Somu, R. Rajavel, M. Subramanian, and P. Prince Reynold, *Mater. Today Proc.*, **33**: 5156 (2020).
21. S. Vijayan, R. Raju, and S. R. K. Rao, *Mater. Manuf. Process.*, **25**, Iss. 11: 1206 (2010).
22. E. J. Joseph and K. Panneerselvam, *Mater. Today Proc.*, **46**: 9150 (2021).

Metallophysics and Advanced Technologies
Металофіз. новітні технол.
Metallofiz. Noveishie Tekhnol.
2024, vol. 46, No. 5, pp. 467–477
https://doi.org/10.15407/mfint.46.05.0467
Reprints available directly from the publisher

PACS numbers: 06.60.Vz, 81.05.Lg, 81.05.U-, 81.07.De, 81.20.Vj, 82.30.Lp, 88.20.mt

Influence of Pyrolysis Products on the Formation of a Joint During Pressure Welding Through a Layer of Hydrocarbon Substance

O. V. Jartovsky

Donbass State Engineering Academy,
72 Akademichna Str.,
UA-84313 Kramatorsk, Ukraine

The work is concerned with the study of the process of joint formation during pressure welding by pulse current through a layer of hydrocarbon substance. During the development of this welding method, there was no necessary amount of scientific knowledge about concomitant physicochemical processes. Interdisciplinary experimental studies performed by different authors have allowed establishing scientific facts necessary for the formation of a hypothesis about the mechanism of formation of a welded joint. Carbon nanoformations are found and their properties are studied. The phenomena accompanying the passage of pulse electric current through them are studied. The phenomena of anomalous mass transfer under the action of shock loading during diffusion welding of dissimilar materials are studied. It is experimentally proved that electroexplosive and electromagnetic phenomena as well as shock waves activate diffusion processes, when applied to the surface layers of metal. The hypothesis assumes that, when a pulsed electric current of constant polarity is passed, an electrical explosion of contacting metallic microblasts occurs. The formation and subsequent microexplosions of conductive carbon particles occur. Microexplosions and shock waves activate diffusion processes on the surfaces to be joined. The process is completed after the 'Coulomb explosion' and the release of pyrolysis products from the central part of the joint of the welded surfaces. It is experimentally proved that the formation of the joint occurs at temperatures below the melting point of the materials to be welded. The time of joint formation at the same

Corresponding author: Oleksandr Volodymyrovych Jartovsky
E-mail: avpivras@gmail.com

Citation: O. V. Jartovsky, Influence of Pyrolysis Products on the Formation of a Joint During Pressure Welding Through a Layer of Hydrocarbon Substance, *Metallofiz. Noveishie Tekhnol.*, **46**, No. 5: 467–477 (2024).
DOI: 10.15407/mfint.46.05.0467

temperature is much shorter than during diffusion welding in vacuum. The structure of the welded joint is similar to the structure obtained by diffusion welding in vacuum. The methodology is developed, and experimental studies are carried out. The obtained results confirm the put forward hypothesis and correspond to the previously performed interdisciplinary studies of specialists.

Key words: pressure welding, hydrocarbon substances, electric explosion, electric current, nanotubes, diffusion.

Робота стосується дослідження процесу формування з'єднання під час зварювання тиском імпульсним струмом через шар вуглеводневої речовини. На момент розробки цього способу зварювання не було необхідного обсягу наукових знань про фізико-хемічні процеси, що перебігають водночас. Міждисциплінарні експериментальні дослідження різних авторів дали змогу встановити наукові факти, необхідні для формування гіпотези про механізм утворення зварного з'єднання. Виявлено вуглецеві наноутворення та вивчено їхні властивості. Вивчено явища, що супроводжують проходження через них імпульсного електричного струму. Досліджено явища аномального масопереносу під дією ударного навантаження під час дифузійного зварювання різнорідних матеріялів. Експериментально доведено, що електровибухові й електромагнетні явища, а також ударні хвилі активізують дифузійні процеси під час дії на поверхневі шари металу. Гіпотеза припускає, що під час проходження імпульсного електричного струму постійної полярности відбувається електричний вибух контактувальних металевих мікровибухів. Відбувається утворення та подальші мікровибухи струмопровідних частинок вуглецю. Мікровибухи й ударні хвилі активують дифузійні процеси на поверхнях, що з'єднуються. Процес завершується після «Кулонового вибуху» та виділення продуктів піролізи з центральної частини стику зварюваних поверхонь. Експериментально доведено, що формування з'єднання відбувається за температур нижче температури топлення матеріялів, що зварюються. Час формування з'єднання за тієї ж температури значно коротший, аніж за дифузійного зварювання у вакуумі. Структура зварного з'єднання подібна до структури, одержаної за дифузійного зварювання у вакуумі. Розроблено методику та проведено експериментальні дослідження. Одержані результати підтверджують висунуту гіпотезу та відповідають раніше виконаним міждисциплінарним дослідженням фахівців.

Ключові слова: зварювання тиском, вуглеводневі речовини, електричний вибух, електричний струм, нанотрубки, дифузія.

(Received 18 January, 2024; in final version, 11 March, 2024)

1. INTRODUCTION

Pressure welding is widely used in industry. One of the types of pressure welding is vacuum diffusion welding. In vacuum diffusion welding, the joint is formed because of deformation effect on the surfaces

of the materials being welded to be joined. Joint formation occurs with the formation of a transition zone and joint grains at the contact points. There is a model for the formation of a diffusion compound [1]. It involves three stages. First, physical contact is formed based on interatomic interaction. Further, the contact surfaces are activated with the formation of active centres on the surface of the harder of the metals to be joined. After that, volumetric interaction takes place on the active centres. This is accompanied by stress relaxation. The formation of a joint with minimal deformation in the welding zone with high productivity is an urgent task and is solved in different technological processes in different ways. One of the methods for intensifying the diffusion welding process is the use of intermediate layers. Known technologies [2–5], which use various kinds of tapes and foils, powder layers. The processes occurring during the formation of 'material–layer–material' contacts are determined by the properties of all substances in the contact zone. The use of intermediate layers [4, 6–8] of submicron and nanosize powders makes it possible to exclude macroplastic deformations in the zone of the welded joint. The use of an activating Ni sublayer and a powder layer of submicron Ni powder made it possible [6] to obtain a high-quality diffusion joint of steel samples at temperatures of 0.5–0.6 of the melting temperature of the material being welded. Researchers have carried out work to study the factors that accelerate diffusion processes in the zone of formation of a welded joint. The phenomenon of anomalous mass transfer under shock loading of dissimilar materials during welding has been experimentally proved [9]. The method of radioactive isotopes on commercially pure metals (Fe, Ni, Cu) and steels (steel3, 12Kh18N10T) was used to study diffusion processes during high-speed plastic deformation of metals [10–16].

The occurrence of an electric current pulse during high-speed plastic deformation of metals has been established. There is a dependence of the current strength on the nature of the material and the rate of deformation of the metal. Electric potential and anomalous mass transfer are observed only because of pulsed plastic deformation. The phenomena are interconnected and occur simultaneously. Experimental studies were carried out [17] to study the simultaneous effects of double and triple effects. Three processing schemes were investigated. According to the first scheme, alternating deformations with an ultrasonic frequency were used at elevated temperatures. The second scheme involved the use of ultrasonic shock treatment together with pulsed plastic deformation. According to the third scheme, ultrasonic vibrations, a constant magnetic field and quasi-static deformation were simultaneously applied without heating. The results of experimental studies [17] indicate that the use of double and triple effects is promising for obtaining diffusion layers on metals and alloys. Experi-

mental studies [18] on welding metals in the solid phase using high-density current pulses have shown the possibility of high-quality welding with various pulse shapes. The authors of [19] presented an analysis of the mechanism of interaction of two dissimilar materials under the influence of plastic deformation and high-density pulsed current for assessing the strength and quality of metal joining. An assessment of the energy interaction of two metals under the influence of a pulsed current and plastic deformation is carried out. The studies carried out confirm the effect of pulsed current on diffusion processes. The presented works confirm the possibility of stimulating diffuse processes by pulsed electric current, pulsed plastic deformation and combined action. There are data on the study of the influence of elastic waves on the rate of chemical transformations in a solid. The work [20] describes low-temperature solid-phase detonation. The author has proposed a probable mechanism for this phenomenon. The initiator and driving force of ultrafast low-temperature chemical transformations in solids is an elastic wave. The authors of Ref. [20] argue that from a combination of compressive, tensile, and shear deformations, shear deformations are more effective. They are primarily responsible for superfast conversions in the system.

The authors of works [21, 22] proposed to introduce hydrocarbon substances into the space between the surfaces to be welded, and to carry out heating by passing a pulsed electric current. The introduction of a hydrocarbon substance into the space between the surfaces to be welded when heated by a pulsed electric current makes it possible to accelerate the formation of a joint. The literary sources do not describe the processes occurring during the formation of welded joint using interlayers of hydrocarbon substances. The task is urgent and of great practical importance. The previously described studies by various authors suggest a special role for a number of factors affecting the acceleration of diffusion processes. These factors include the dispersion of substances in microvolumes between the contacting surfaces [4, 6–8], the electromagnetic effect of a pulsed electric current [17–19], a pulsed force [9–16, 20] on the surfaces of materials to be welded.

When a pulsed electric current of constant polarity is flowing, local overheating occurs at the contact points of the metal surfaces in contact with each other and electrical explosions occur. In the space between the surfaces to be welded, pyrolysis of hydrocarbon substance occurs with the formation of nanosize carbon formations. The resulting conductive carbon particles explode to form a multitude of micropinches. Shock waves activate diffusion processes on the surfaces to be joined. The proposed hypothesis is based on a large number of interdisciplinary experimental studies. In the literature, there is no model of joint formation in pressure welding through a hydrocarbon layer.

The aim of this paper is experimental verification of the provisions

of the proposed hypothesis.

The objectives of this work are to develop an experimental technique to prove the formation of carbon structures in the microvolumes between the surfaces to be welded, to show experimentally the presence of electric charge of carbon structures, to show experimentally their movement to the centre of the cross-section of the welded surfaces under the action of the magnetic field of the pulse electric current of constant polarity. An accumulation of charged carbon structures is formed there. When a critical mass of charged particles accumulates, a 'Coulomb explosion' occurs.

2. METHODS, EXPERIMENTAL RESULTS AND DISCUSSION

To accomplish the set task, an experimental setup was developed and used, consisting of a power supply with a pulsed electric current of constant polarity, devices for fastening samples and longitudinal compression. Experiments were carried out to isolate the substance formed during the pyrolysis of the hydrocarbon substance. Cylindrical specimens with an axial circular cylindrical hole were used. The surfaces were coated with a hydrocarbon material (uncured epoxy) prior to welding. Welding temperature was of 1180–1200°C. The heating rate of the welded joint did not exceed 120–200°C/sec. The duration of the welding process did not exceed 10–12 seconds. The nature of the destruction of the samples was studied during mechanical tests of the welded joint. The structure of the welded joint was investigated by metallography methods. The nature of the release of the substance from the welded joint was studied visually.

In pressure welding with the use of hydrocarbon interlayers of homogeneous and dissimilar steels, the process always ended with the release of a substance from the joint zone with a specific sound and flash. This allowed us to assume the nature of the movement of the substance at the junction between the surfaces to be joined.

First, the pyrolysis products moved to the central part of the joint. Then, because of the 'Coulomb explosion', the substance was ejected. Figure 1, *a* show a diagram of the movement of products during heating of the welded surfaces and pyrolysis of hydrocarbon layers. Figure 1, *b* shows a diagram of the movement of products during an explosion of a substance.

Such motion of substance in the joint is possible at formation of charged particles because of explosion of metal in the contact points and microexplosions in products of pyrolysis of hydrocarbon material. This does not contradict the known data [23]. Pressure welding using hydrocarbon interlayers is characterized by the movement of pyrolysis products into the central part of the joint. This assumption was confirmed by physical experiment. A special sample design was used to

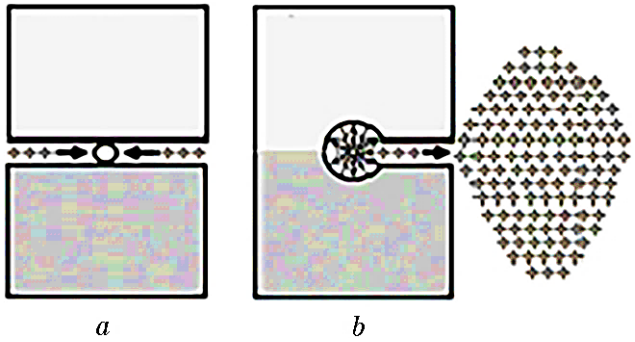

Fig. 1. Diagram of the movement of products at the joint during welding.

isolate the formed substances. Cylindrical samples with an axial round cylindrical hole were prepared. The ends of the samples were coated with the hydrocarbon substance under study. They were placed in a fixation device, subjected to compression and passed a pulsed current of constant polarity. The scheme of the experiment is shown in Fig. 2.

The experiment was conducted according to two schemes. According to the first scheme, the surfaces of the samples to be joined were coated with a hydrocarbon substance. The samples were placed in a fixing device, subjected to longitudinal compression. The joint was heated to the welding temperature and was welded. Then, the specimens were opened by milling parallel to the specimen axis. The nature of the release of the substance from the welded joint was studied visually. There were studied the structure of the substance inside the sample chamber. The substance inside the sample is shown in Fig. 3.

According to the second scheme, the samples were placed in a fixing device. The surfaces to be joined were coated with a hydrocarbon mate-

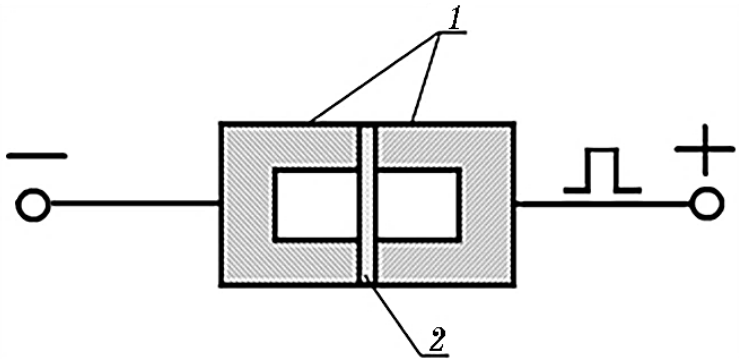

Fig. 2. Scheme of the experiment: steel cylinders with holes (*1*), hydrocarbon substance (*2*).

Fig. 3. Carbon layers inside the sample chamber.

rial. By passing a current, they were heated to the welding temperature. The samples were not subjected to longitudinal compression. After heating to the welding temperature, the samples were opened perpendicular to the axis at the place of heating. The placement of the products of pyrolysis of the hydrocarbon substance inside the sample chamber was studied. The effectiveness of the effect of pyrolysis products of the investigated hydrocarbon substance during welding was checked. The results of displacement of carbon structures are shown in Fig. 4. This figure shows the uneven distribution of carbon particles.

The matter inside the chamber is represented by carbon structures. Both parts of the chamber have different amounts of carbon on the walls. Part of sample 1 has a thin layer on the surface. Part of the layer is missing. Part of sample 2 contains dense deposits of carbon particles. The presented experimental results confirm the presence of charged particles in the space between the surfaces to be joined. Charged carbon particles under the pinch effect move deep into the sample. There they settle on the sample walls. The distribution of the particles is not uniform. The particles settle on the surface with opposite electrode charge. This confirms the presence of electric charge on

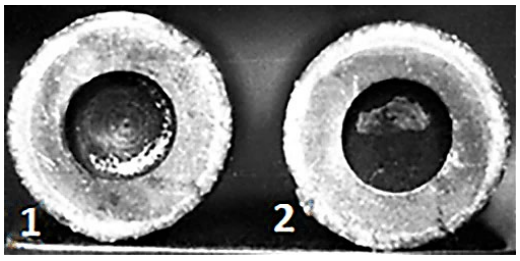

Fig. 4. Uneven distribution of carbon formations in different parts of the sample.

the carbon particles. Cylindrical steel specimens without cavities were welded. When opening the solid cylindrical welded specimens without internal cavities, capsules were found, in which carbon particles accumulated during welding according to the scheme in Fig. 1, *a*. As a result of a 'Coulomb explosion', these carbon particles are ejected from the weld and are visually observed as a flash in Fig. 1, *b*. Figure 5 shows a fragment of a capsule with a product exit channel.

Obtained experimental results are in agreement with the available experimental data [24] on the synthesis of carbon nanotubes at high pressures and temperatures. The experimental results also confirm the presence of high pressure and temperatures in the space between the surfaces to be welded. The creation of high pressure occurs due to multiple micro explosions. The source of this kind of explosion is the contact points of the surfaces to be welded. During passing an electric current through the surfaces to be welded, its value in the initial period of the process is 10^3–10^4 times higher than the nominal value due to the fact that the contact area is from 0.01% to 0.1% of its nominal value [25]. The explosion time is about 120–300 ns [26]. The pinch effect is a factor contributing to multiple manifestations of the 'Coulomb explosion' in the environment of carbon nanoformations between the surfaces to be welded. The existence of both the 'Coulomb explosion' and the charge of carbon nanoparticles coincide with the conclusions in [27, 28]. Shock waves increase diffusion activity on the surfaces to be welded. Due to the electromagnetic effect and the action of shock waves, diffusion processes are accelerated. The increase in the diameter of the cylindrical specimens at the point of formation of the joint after welding did not exceed 0.5%.

Mechanical tensile and toughness tests of homogeneous steels showed characteristics that did not differ from those of the base metal.

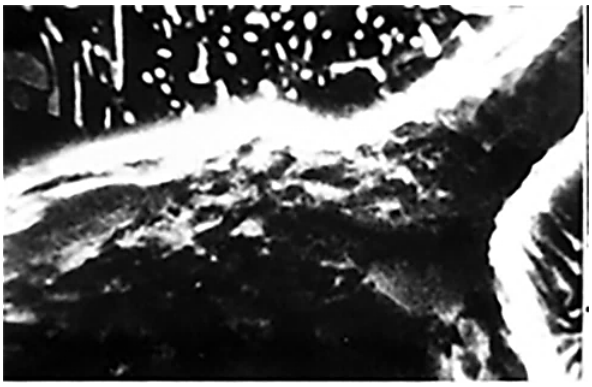

Fig. 5. Fragment of the image of the capsule with the product outlet channel (increase of 5000).

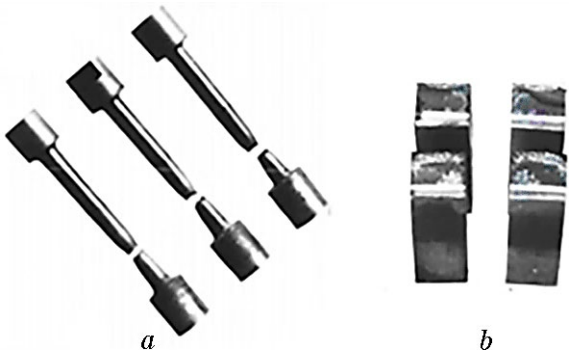

Fig. 6. The nature of the fracture of the sample during tensile tests (*a*) and the impact toughness of the KCU joint (*b*) according to GOST 6996-80 of R6M5 steel with steel 45 of the welded joint obtained by pressure welding through hydrocarbon interlayers.

In tensile tests of a welded joint of dissimilar metals, fracture occurred on a less strong material. Specimens for impact toughness fractured in brittle material. The nature of the destruction is shown in Fig. 6.

The microstructure of the welded joint of steel R6M5K5 with steel 45 is shown in Fig. 7.

The structure of the welded joint obtained by the investigated method is similar to the structure of the joint by diffusion welding in vacuum. The duration of the process of formation of a joint in vacuum without the use of intermediate layers and during welding by the investigated method was compared. According to Ref. [29], diffusion welding in vacuum under various conditions can be from 20 to 60 minutes. During welding with pressure through a layer of hydro-

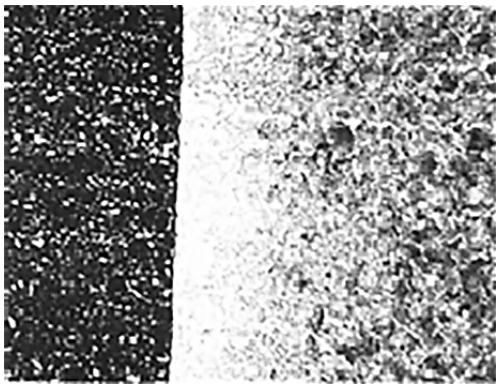

Fig. 7. Microstructure of welded joint of steel R6M5K5 with steel 45 (increase of 200).

carbon substance for welding samples with a diameter of 16 mm, it takes 10–12 sec.

3. CONCLUSION

Based on the results of a large number of interdisciplinary experimental studies, the hypothesis [1] about the influence of hydrocarbon interlayers on the formation of a welded joint was first put forward and experimentally confirmed. When passing a pulsed electric current of constant polarity, an electric explosion occurs at the contact points of the welded metal surfaces. In the space between the welded surfaces, pyrolysis of hydrocarbon substance occurs. This is accompanied by multifactor pulse force and electromagnetic impact. These impacts contribute to the activation of diffusion processes.

The methodology of experimental studies has been developed and realized. The experiment confirmed the formation of carbon structures in the microvolumes between the surfaces to be welded. The formation of charged particles from hydrocarbon pyrolysis products has been proved. It is proved that, under the action of magnetic field, the charged particles move to the central part and a critical mass of charged particles is formed there. This leads to a powerful 'Coulomb explosion' with the release of pyrolysis products into the surrounding space. The mechanical properties and structure of the welded joint of steel billets have been investigated. The structure of the welded joint is similar to the structure of the joint obtained by diffusion welding in vacuum.

REFERENCES

1. O. V. Jartovsky and O. V. Larichkin, *Prog. Phys. Met.*, **22**, No. 3: 440 (2021) (in Ukrainian).
2. N. F. Kazakov, *Diffuzionnaya Svarka Materialov* [Diffusion Welding of Material] (Moskva: Mashinostroenie: 1976) (in Russian).
3. E. S. Karakozov, *Svarka Metallov Davleniem* [Metal Pressure Welding] (Moskva: Mashinostroenie: 1986) (in Russian).
4. A. V. Lyushinskiy, *Diffuzionnaya Svarka Raznorodnykh Materialov* [Diffusion Welding of Dissimilar Materials] (Moscow: Izdat. Tsentr Akademiya: 2006) (in Russian).
5. A. K. Bulkov, V. V. Peshkov, V. R. Petrenko, D. N. Balbekov, and A. I. Strygin, *Svarochnoye Proizvodstvo*, **3** :15 (2013) (in Russian).
6. G. M. Zeer, E. G. Zelenkova, O. V. Belousov, Yu. P. Koroleva, E. N. Fedorova, and A. A. Mikheev, *Zhurnal Tekhnicheskoy Fiziki*, **85**, No. 4:46 (2015) (in Russian).
7. V. V. Peshkov, V. R. Petrenko, A. B. Bulkov, and D. N. Balbekov, *Vestnik Voronezhskogo Gosudarstvennogo Tekhnicheskogo Universiteta*, **7**, No. 10: 13 (2011) (in Russian).

8. E. V. Valitova, A. Kh. Akhunova, V. A. Valitov, R. Ya. Lutfullin, S. V. Dmitriev, and M. Kh. Mukhametrakhimov, *Pis'ma o Materialakh*, **4**, No. 3: 19 (2014) (in Russian).
9. L. N. Larikov, V. F. Mazanko, and V. V. Nemoshkalenko, *Fizika i Khimiya Obrabotki Materialov*, **4**: 20 (1981) (in Russian).
10. V. P. Bevz, V. F. Mazanko, A. V. Filatov, and S. P. Vorona, *Metallofiz. Noveishie Tekhnol.*, **28**, Special Issue: 271 (2006) (in Russian).
11. V. F. Mazanko, V. S. Mikhalenkov, E. A. Tsapko, E. I. Bogdanov, V. P. Bevz, and S. P. Vorona, *Doklady NAN Ukrainy*, **29**, No. 4: 471 (2007) (in Ukrainian).
12. V. F. Mazanko, D. V. Mironov, D. Gertsriken, A. A. Mironova, and V. P. Bevz, *Metallofiz. Noveishie Tekhnol.*, **29**, No. 2: 173 (2007) (in Russian).
13. V. S. Mikhalenkov, A. V. Obil'nyy, E. A. Tsapko, V. P. Bevz, E. I. Bogdanov, and A. N. Yaremenko, *Metallofiz. Noveishie Tekhnol.*, **29**, No. 4: 471 (2007) (in Russian).
14. V. F. Mazanko, D. V. Mironov, D. S. Gertsriken, and V. P. Bevz, *Metallofiz. Noveishie Tekhnol.*, **29**, No. 4: 483 (2007) (in Russian).
15. V. F. Mazanko, V. P. Bevz, S. P. Vorona, K. Kharchenko, T. R. Ganeev, and Yu. V. Fal'chenko, *Vestnik Chernigovskogo Gosudarstvennogo Tekhnicheskogo Universiteta*, **34**: 125 (2008) (in Russian).
16. V. Bevz, D. Gercryken, N. Zajceva, and V. Mazanko, *Visnyk L'viv. Un-tu*, **41**: 216 (2008) (in Ukrainian).
17. D. V. Mironov, V. F. Mazanko, G. I. Prokopenko, B. N. Mordyuk, D. S. Gertsriken, S. E. Bogdanov, E. N. Khranovskaya, and T. V. Mironova, *Izvestiya Samarskogo Nauchnogo Tsentra Rossiyskoy Akademii Nauk*, **14**, No. 4: 74 (2012) (in Russian).
18. V. D. Polovinko and E. S. Yurchenko, *Ehlektronnaya Obrabotka Materialov*: 93 (2008) (in Russian).
19. S. P. Moskvitin and S. N. Barshutin, *Vestnik TGTU*, **22**, No. 4: 694 (2016) (in Russian).
20. A. A. Mkhitaryan, *Khimicheskiy Zhurnal Armenii*, **1**: 42 (2006) (in Russian).
21. M. L. Finkel'shtein, *Diffuzionnaya Svarka v Zhidkikh Sredakh* [Diffusion Welding in Liquids] (Moskva: Metallurgiya: 1978) (in Russian).
22. S. P. Kocharmin, A. P. Semenov, and N. V. Guzev, *Sposob Svarki Davleniem i Mashina dlya Ego Osushchestvleniya* [Pressure Welding Method and Machine for Its Implementation], Avtorskoe Svidetel'stvo SSSR 4975280, kl. V23K 11/02 (1979) (in Russian).
23. V. V. Vladimirov, *Usp. Fiz. Nauk*, **117**, No. 1: 79 (1975) (in Russian).
24. Yu. S. Buranova, *Trudy MFTI*, **3**, No. 3: 30 (2011) (in Russian).
25. N. B. Demkin, *Kontaktirovanie Sherokhovatykh Poverkhnostey* [Contacting Rough Surfaces] (Moskva: Nauka: 1970) (in Russian).
26. A. E. Borisevich and S. L. Cherkas, *Zhurnal Tekhnicheskoy Fiziki*, **82**, No. 10: 58 (2012) (in Russian).
27. A. N. Dolgov, N. A. Klyachin, and D. E. Prokhorovich, *Prikl. Fiz.*, **3**: 10 (2019) (in Russian).
28. V. V. Komarov, A. M. Popova, I. O. Stureyko, L. Shmidt, and Kh. Yungklas, *VMU. Seriya 3. Fizika. Astronomiya*, **13**: 2 (2013) (in Russian).
29. V. V. Peshkov, A. B. Bulkov, A. A. Batishchev, A. V. Bashkatov, and V. R. Petrenko, *Svarochnoye Proizvodstvo*, **9**: 18 (2004) (in Russian).

Metallophysics and Advanced Technologies
Металофіз. новітні технол.
Metallofiz. Noveishie Tekhnol.
2024, vol. 46, No. 6, pp. 479–490
https://doi.org/10.15407/mfint.46.05.0479
Reprints available directly from the publisher

PACS numbers: 68.37.-d, 68.60.Dv, 81.15.-z, 81.65.Kn, 81.65.Mq, 82.30.-b, 82.33.Pt

Development of Heat-Resistant Coatings for Protection of Niobium and Tantalum from the Oxidizing Effect of Air at Temperatures 1700–1900°C

S. G. Rudenkyi, V. I. Zmii, R. V. Kryvoshapka, M. F. Kartsev, O. O. Kornieiev, O. V. Kunchenko, Y. V. Kunchenko, T. P. Ryzhova, I. A. Liashenko, and M. Y. Bredikhin

National Science Centre 'Kharkiv Institute of Physics and Technology', N.A.S. of Ukraine,
1 Akademichna Str.,
UA-61108 Kharkiv, Ukraine

The paper presents the results of creating protective coatings on niobium and tantalum samples. These coated samples are tested for heat resistance in air in the temperature range of 1700–1900°C. The coating is formed by the method of activated vacuum diffusion saturation at temperatures of 1150–1310°C. When forming a part of the protective coatings, a layer of slurry is applied to the surface of the samples, followed by chemical and thermal treatment in a vacuum in the presence of NaCl vapours. A thermodynamic analysis of possible chemical reactions taking place in the process of formation of protective coatings is carried out. The developed heat-resistant coatings provide protection of niobium samples from air oxidation at a temperature of 1700°C from 8 to 13.5 hours. Heat-resistant coatings created on samples with Nb and Ta protect them from exposure to an oxidizing environment from 3 to 6.3 hours at a temperature of 1800°C and for 0.5 hours at a temperature of 1900°C.

Key words: protective layer, activated vacuum diffusion saturation, solid non-porous coatings, refractory metals, heat-resistant.

У роботі представлено результати створення захисних покриттів на зразках

Corresponding author: Ruslan V. Kryvoshapka
E-mail: kryvoshapkarv@gmail.com

Citation: S. G. Rudenkyi, V. I. Zmii, R. V. Kryvoshapka, M. F. Kartsev, O. O. Kornieiev, O. V. Kunchenko, Y. V. Kunchenko, T. P. Ryzhova, I. A. Liashenko, and M. Y. Bredikhin, Development of Heat-Resistant Coatings for Protection of Niobium and Tantalum from the Oxidizing Effect of Air at Temperatures 1700–1900°C, *Metallofiz. Noveishie Tekhnol.*, **46**, No. 5: 479–490 (2024). DOI: 10.15407/mfint.46.05.0479

з ніобію та танталу. Ці зразки з покриттями випробовували на жаротривкість на повітрі в інтервалі температур 1700–1900°C. Покриття формували методом активованого вакуумного дифузійного насичення за температур у 1150–1310°C. Для формування частини захисних покриттів на поверхню зразків наносили шар шлікеру з подальшим хеміко-термічним обробленням у вакуумі за присутности парів NaCl. Було проведено термодинамічну аналізу можливих хемічних реакцій, що мають місце у процесі утворення захисних покриттів. Розроблені жаротривкі покриття забезпечують захист зразків з ніобію від окиснення на повітрі за температури у 1700°C від 8 до 13,5 годин. Жаротривкі покриття, створені на зразках з Nb і Ta, захищають їх від впливу окисного середовища від 3 до 6,3 годин за температури у 1800°C та протягом 0,5 години за температури у 1900°C.

Ключові слова: захисний шар, активоване вакуумне дифузійне насичення, суцільні непористі покриття, тяжкотопкі метали, термостійкість.

(Received 13 November, 2023; in final version, 15 December, 2023)

1. INTRODUCTION

The problem of protecting refractory metals (niobium and tantalum) from the influence of oxidizing environments at elevated temperatures remains relevant today. Previously, they tried to create a protective layer on the surface of these metals with the help of silicification and the introduction of refractory components into it. Another method was preliminary boron saturation of the niobium surface with subsequent silicification. This method makes it possible to reduce the rate of degradation of the heat-resistant layer on the refractory metal. Currently, one of the most high-quality methods of protecting niobium from the influence of an oxidizing environment is a heat-resistant coating, which is formed using a two-stage technology.

At the first stage, a layer of molybdenum is applied to the niobium surface, and then the silicification process is carried out. This stage forms a layer of molybdenum disilicide on niobium. The first stage of creating this coating—applying a layer of molybdenum is carried out by the method of ion bombardment condensation (IBO). In the case of protection of a complex-shaped niobium product, the process of molybdenum deposition is carried out by gradually applying a layer of metal to separate areas of the surface of the part. Direct silicification of niobium does not provide protection of this metal against the influence of oxidizing environments at temperatures above 1000°C. When the niobium surface is saturated with silicon, a coating is formed, which can consist of 3 layers. These are layers consisting of niobium silicides $NbSi_2$, Nb_5Si_3, Nb_3Si, respectively. All these compounds form silicon oxide SiO_2 and niobium oxide Nb_2O_5, when exposed to oxidizing media. Niobium oxide Nb_2O_5 has a powdery structure and does not al-

low creating a continuous non-porous coating on the metal surface. Such a coating does not prevent the penetration of oxygen to niobium and the oxidation of this metal will continue.

One of the ways to eliminate this problem is to saturate the niobium surface with several refractory metals. When the surface is further saturated with silicon, a layer consisting of several refractory silicides is formed on the niobium. Under the action of oxidizing media, a layer consisting of several oxides is formed on such a surface. Depending on the goal, the content of niobium oxide in this surface layer will not be the main one. This can make it possible to form a continuous heat-resistant layer on the surface of niobium, which prevents the penetration of oxygen to the metal. The method of activated vacuum diffusion saturation allows introducing such metals as Ti, Cr, V, Hf, Zr and others into the treated surface. The use of sodium chloride as an activator in this method makes it environmentally friendly [1, 2]. It makes it possible to form uniform diffuse layers even on products with holes of small diameter [3].

The purpose of this work is to create heat-resistant coatings to protect niobium and tantalum from the effects of oxidizing environments at temperatures $T = 1700–1900$°C by the method of vacuum activated diffusion saturation.

2. MATERIALS AND METHODS

In this paper, the main method of forming heat-resistant coatings on niobium and tantalum was the vacuum diffusion saturation method. An activator (sodium chloride) was used to speed up the processing process. Niobium and tantalum samples had a cylindrical shape with a diameter of 2 mm and a length of 80 mm. This form of samples allows them to be tested for heat resistance on a special stand. On this device, the samples are heated by direct passage of electric current to a given temperature. The temperature of the samples is determined by an optical pyrometer. The measure of heat resistance of the samples is the duration of their work in the air until complete destruction.

Powders of various elements and compounds were used during the chemical and thermal treatment of the samples. Silicon powder of semiconductor purity was used for silicification. When carrying out the process of vacuum activated diffusion borosilication, a powder mixture of the composition Si (95–97) + B (3–5) % wt. was used. In addition, to speed up the process of formation of the protective coating, slurry was used. Slurry was created on the basis of a powder mixture with the addition of a liquid binder. Tsapon-lacquer КО-85 was used as such a substance. Slurry was applied to the surface of the sample before its chemical and thermal treatment. X-ray fluorescence analysis was used to measure the surface composition during the formation of

coatings. For this purpose, flat witness samples were used. These samples were usually used for metallographic research. In this way, the structure and structure of the surface layers on the samples were studied. Another way to conduct research on the process of forming heat-resistant coatings was to use calculations to determine thermodynamically possible chemical reactions that take place in the reaction space during activated vacuum diffusion saturation. The analysis of possible chemical reactions allows us to make assumptions about the mechanism of the transfer of saturating elements and the formation of the surface layer and its composition.

3. RESULTS AND DISCUSSION

To create a heat-resistant coating on niobium and tantalum, it is necessary to create a layer on their surface consisting of several refractory metals. These should be such metals as chromium, zirconium, hafnium, titanium, vanadium, molybdenum, tungsten. Silicon and boron must be introduced into this layer. Due to its physical properties, boron is a component that inhibits the processes of destruction of heat-resistant coatings at elevated temperatures. We have tested various options of protective coatings, which are presented below in Table 1. Under point 1 of this table, a comprehensive protective coating is given. Niobium samples were processed in chromium powder in the presence of NaCl vapours and reduced pressure at a temperature of 1150°C for 6 hours.

During the interaction of NaCl vapours with chromium, 5 chromium chlorides can be formed. In Table 2, column 1 is the reaction number, column 2 is the chemical reaction equation, next column 3 is the reaction temperature, and columns 4 and 5 are the degree of reaction at the specified pressure. The degree of progress of a chemical reaction α is the proportion of starting substances that have reacted according to the reaction. The flow of the activator (sodium chloride) was set by its temperature. During the processes of vacuum diffusion saturation, the temperature of NaCl was maintained in the range of 790–810°C. At these temperature values, the pressure of saturated NaCl vapour varies in the range from 1 to 10^2 Pa. The design of the container is analogous to a Knudsen cell; so, the vapour pressure and composition of the gas medium will be the same throughout the reaction space [4–6]. The process of vacuum activated diffusion chrome plating was carried out at a temperature of $T = 1423$ K and a gas pressure in the reaction space in the range of $1–10^2$ Pa. Under these conditions, the main components of the gas saturation medium will be the lower chromium chlorides CrCl and $CrCl_2$ (reactions 1, 2, Table 2). These compounds interact with the niobium surface according to reactions 3, 4 (Table 2). Chromium plating led to the formation of a surface layer with a composition of

27.9 Nb + 72.1 Cr % wt. Then, a layer of 70 Mo + 20 Ni + 5.4 Ti + 2.8 Si + + 1 B + 0.8 Al % wt. slurry was applied to the surface of these samples and borosilication was carried out.

The composition of the slurry includes titanium, silicon, nickel, boron and aluminium. As thermodynamic analysis shows, when these components interact with NaCl sodium chloride vapours, according to reactions 5–15 (Table 2), chlorides of titanium, silicon, and boron are formed. Therefore, after chemical and thermal treatment, the surface layer has the following composition: 15.75 Si + 8.65 Ti + 28.05 Cr + + 0.25 Ni + 34.3 Nb + 18.8 Mo % wt. This coating provides protection against air oxidation for 8 hours. After chromium plating of niobium samples, a layer containing 72% Cr is formed on the surface. When chrome-plating low-carbon steels, a layer is formed on their surface, the concentration of chromium in which is about 90%. Therefore, it is possible to try to achieve an even higher content of this element on the surface of the sample by varying the niobium chroming regimes.

TABLE 1. Results of comparative heat resistance test of niobium and tantalum samples with protective coatings.

No.	Substrate	The process of forming a heat-resistant coating on the sample	Heat resistance test temperature, °C	Heat resistance, h
1	2	3	4	5
1	Nb	The samples were chrome-plated at a temperature of 1150°C for 6 hours, then a layer of 70 Mo + 20 Ni + + 5.4 Ti + 2.8 Si + 1 B + 0.8Al % wt. was applied to them and borosilicated at T = 1280°C for 6 hours	1700	8
2	Nb	A layer of 35 $MoSi_2$ + 20 HfB_2 + 10 $ZrSi_2$ + 20 VSi_2 + + 9 Al + 6 B % wt. was applied to the samples and borosilicated in a mixture of 97 Si + 3 B % wt. at T = 1300°C for 7 hours	1700 1800	9 3
3	Nb	A layer of 80 Mo + 13.5 Ni + 6.5 Sn % wt. slurry was applied to the samples and titanated at T = 1150°C for 7 hours. After that, the samples were borosilicated at a temperature of T = 1300°C for 7 hours	1700	9
4	Nb	The samples were hafniated at a temperature of 1300°C for 6 hours using NaCl vapours. After that, a slurry of the composition 35 HfB_2 + 20 $ZrSi_2$ + 20 $MoSi_2$ + + 10 TiB_2 + 6.5 Ni + 6.5 Zr + 2 B was applied to the surface of the samples and processed in a mixture of powders 22 Si + 22 $ZrSi_2$ + 22 HfB_2 + 31 $MoSi_2$ % wt. at temperature T = 1300°C for 7 hours. NaCl was used to speed up the process	1700	9–13.5

Continuation of Table 1.

1	2	3	4	5
5	Nb	The samples were processed in a powder mixture of 40 $MoSi_2$ + 20 HfB_2 + 20 VSi_2 + 20 Si % wt. in the presence of NaCl steam at a temperature of T = 1310°C for 7 hours	1800	5–6.3
6	Ta	The samples were processed in a powder mixture of 40 $MoSi_2$ + 20 HfB_2 + 20 VSi_2 + 20 Si % wt. in the presence of NaCl steam at a temperature of T = 1310°C for 7 hours	1800	5–6.3
7	Nb	The samples were annealed in a mixture of composition 40 Si + 30 HfB_2 + 30 $ZrSi_2$ % wt. in NaCl vapours at a temperature of T = 1300°C for 7 hours	1900	0.5
8	Ta	The samples were annealed in a mixture of composition 40 Si + 30 HfB_2 + 30 $ZrSi_2$ % wt. in NaCl vapours at a temperature of T = 1300°C for 7 hours	1900	0.5

Table 1, point 2 shows the method of obtaining a heat-resistant layer on a niobium sample. A layer of 35 $MoSi_2$ + 20 HfB_2 + 10 $ZrSi_2$ + 20 VSi_2 + + 9 Al + 6 B % wt. was applied to this sample, and then borosilication was carried out at a temperature of T = 1573 K. During borosilication, the interaction of sodium chloride NaCl vapours with the components of the slurry, as well as silicon and boron, occurs in the reaction space. The aluminium present in the slurry is in a liquid state at the temperature of the chemical and thermal treatment. It acts as a liquid layer on the surface of the sample and facilitates the process of forming a diffusion layer. When NaCl vapours are exposed to boron B [4] present in the slurry, boron chlorides BCl, BCl_3 are formed in reactions 12, 13 (Table 2).

The interaction of NaCl steam with molybdenum disilicide $MoSi_2$ leads to the formation of molybdenum dichloride $MoCl_2$ and silicon dichloride $SiCl_2$, reaction 14. The effect of NaCl steam on the slurry component—HfB_2, at the appropriate temperature and pressure, leads to the formation of boron chlorides BCl, BCl_3 and hafnium chlorides $HfCl_2$, $HfCl_3$, $HfCl_4$, points 15–18 (Table 2). The zirconium disilicide $ZrSi_2$ introduced into the slurry under the influence of NaCl steam forms zirconium chlorides ZrCl–$ZrCl_4$ and silicon chlorides SiCl–$SiCl_4$, points 19–30 (Table 2).

Another component of the slurry is VSi_2. When NaCl vapour is exposed to VSi_2, vanadium chlorides and silicon chlorides are formed (points 31–41, Table 2).

The formation of the coating according to point 2 occurs by means of processing in a saturating gas environment consisting of molybdenum

dichloride, boron chlorides, hafnium chlorides, zirconium chlorides, vanadium chlorides, and silicon chlorides. The process also involves borosilication of the niobium surface.

As a result of this chemical-thermal treatment, a diffusion layer is formed on the sample, consisting of molybdenum silicides, hafnium silicides, zirconium silicides, vanadium silicides, and it contains boron in the form of a compound. The heat-resistant layer created by this

TABLE 2. The degree of progress of chemical reactions in the reaction space at temperature T and pressure P.

No.	The equation of a chemical reaction	T, K	Degree of conversion α at pressure $P \cdot 10^2$, Pa	
1	2	3	4	5
1	$NaCl\,(g) + Cr\,(s) = CrCl\,(g) + Na\,(g)$	1423	$1 \cdot 10^{-3}$	$1 \cdot 10^{-2}$
2	$NaCl\,(g) + 1/2Cr\,(s) = 1/2CrCl_2\,(g) + Na\,(g)$	1423	$4 \cdot 10^{-3}$	$1.8 \cdot 10^{-2}$
3	$CrCl\,(g) + 3/8Nb\,(s) = 3/8Cr_2Nb\,(s) + 1/4CrCl_4\,(g)$	1423	1	1
4	$CrCl_2\,(g) + 1/4Nb\,(s) = 1/4Cr_2Nb\,(s) + 1/2CrCl_4\,(g)$	1423	0.87	0.20
5	$NaCl\,(g) + Ti\,(s) = TiCl\,(g) + Na\,(g)$	1553	$4.5 \cdot 10^{-2}$	0.41
6	$NaCl\,(g) + 1/2Ti\,(s) = 1/2TiCl_2\,(g) + Na\,(g)$	1553	$7.6 \cdot 10^{-2}$	0.30
7	$NaCl\,(g) + 1/3Ti\,(s) = 1/3TiCl_3\,(g) + Na\,(g)$	1553	$6.6 \cdot 10^{-2}$	0.19
8	$NaCl\,(g) + 1/4Ti\,(s) = 1/4TiCl_4\,(g) + Na\,(g)$	1553	$1.8 \cdot 10^{-2}$	$4.4 \cdot 10^{-2}$
9	$NaCl\,(g) + Si\,(s) = SiCl\,(g) + Na\,(g)$	1523	$6 \cdot 10^{-3}$	$6 \cdot 10^{-2}$
10	$NaCl\,(g) + 1/2Si\,(s) = 1/2SiCl_2\,(g) + Na\,(g)$	1523	$1.7 \cdot 10^{-2}$	$7.7 \cdot 10^{-2}$
11	$NaCl\,(g) + 1/3Si\,(s) = 1/3SiCl_3\,(g) + Na\,(g)$	1523	$5 \cdot 10^{-3}$	$1.6 \cdot 10^{-2}$
12	$NaCl\,(g) + B\,(s) = BCl\,(g) + Na\,(g)$	1573	$1.5 \cdot 10^{-2}$	0.15
13	$NaCl\,(g) + 1/3B\,(s) = 1/3BCl_3\,(g) + Na\,(g)$	1573	$5 \cdot 10^{-3}$	$1.6 \cdot 10^{-2}$
14	$NaCl\,(g) + 1/6MoSi_2\,(s) = 1/6MoCl_2\,(g) + 1/3SiCl_2\,(g) + Na\,(g)$	1573	$2.3 \cdot 10^{-3}$	$1 \cdot 10^{-2}$
15	$NaCl\,(g) + 1/4HfB_2\,(s) = 1/2BCl\,(g) + 1/4HfCl_2\,(g) + Na\,(g)$	1573	$2 \cdot 10^{-3}$	$1.5 \cdot 10^{-2}$
16	$NaCl\,(g) + 1/5HfB_2\,(s) = 2/5BCl\,(g) + 1/5HfCl_3\,(g) + Na\,(g)$	1573	$5.4 \cdot 10^{-3}$	$3 \cdot 10^{-2}$
17	$NaCl\,(g) + 1/6HfB_2\,(s) = 1/3BCl\,(g) + 1/6HfCl_4\,(g) + Na\,(g)$	1573	$3.2 \cdot 10^{-3}$	$1.4 \cdot 10^{-2}$
18	$NaCl\,(g) + 1/9HfB_2\,(s) = 2/9BCl_3\,(g) + 1/9HfCl_3\,(g) + Na\,(g)$	1573	$3.6 \cdot 10^{-3}$	$1.1 \cdot 10^{-2}$
19	$NaCl\,(g) + 1/5ZrSi_2\,(s) = 1/5ZrCl\,(g) + 2/5SiCl_2\,(g) + Na\,(g)$	1573	$3 \cdot 10^{-3}$	$1.6 \cdot 10^{-2}$
20	$NaCl\,(g) + 1/4ZrSi_2\,(s) = 1/4ZrCl_2\,(g) + 1/2SiCl\,(g) + Na\,(g)$	1573	$3 \cdot 10^{-3}$	$2.4 \cdot 10^{-2}$
21	$NaCl\,(g) + 1/6ZrSi_2\,(s) = 1/6ZrCl_2\,(g) + 1/3SiCl_2\,(g) + Na\,(g)$	1573	$8 \cdot 10^{-3}$	$3.5 \cdot 10^{-2}$
22	$NaCl\,(g) + 1/8ZrSi_2\,(s) = 1/8ZrCl_2\,(g) + 1/4SiCl_3\,(g) + Na\,(g)$	1573	$4 \cdot 10^{-3}$	$1.3 \cdot 10^{-2}$
23	$NaCl\,(g) + 1/5ZrSi_2\,(s) = 1/5ZrCl_3\,(g) + 2/5SiCl\,(g) + Na\,(g)$	1573	$9 \cdot 10^{-3}$	$5 \cdot 10^{-2}$

Continuation of Table 2.

1	2	3	4	5
24	$NaCl\,(g) + 1/7ZrSi_2\,(s) = 1/7ZrCl_3\,(g) + 2/7SiCl_2\,(g) + Na\,(g)$	1573	$1.5\cdot10^{-2}$	$5.9\cdot10^{-2}$
25	$NaCl\,(g) + 1/9ZrSi_2\,(s) = 1/9ZrCl_3\,(g) + 2/9SiCl_3\,(g) + Na\,(g)$	1573	$7\cdot10^{-3}$	$2.2\cdot10^{-2}$
26	$NaCl\,(g) + 1/11ZrSi_2\,(s) = 1/11ZrCl_3\,(g) + 2/11SiCl_4\,(g) + Na\,(g)$	1573	$4\cdot10^{-3}$	$1.1\cdot10^{-2}$
27	$NaCl\,(g) + 1/6ZrSi_2\,(s) = 1/6ZrCl_4\,(g) + 1/3SiCl\,(g) + Na\,(g)$	1573	$1.3\cdot10^{-2}$	$6\cdot10^{-2}$
28	$NaCl\,(g) + 1/8ZrSi_2\,(s) = 1/8ZrCl_4\,(g) + 1/4SiCl_2\,(g) + Na\,(g)$	1573	$1.9\cdot10^{-2}$	$6.6\cdot10^{-2}$
29	$NaCl\,(g) + 1/10ZrSi_2\,(s) = 1/10ZrCl_4\,(g) + 1/5SiCl_3\,(g) + Na\,(g)$	1573	$9.1\cdot10^{-3}$	$2.6\cdot10^{-2}$
30	$NaCl\,(g) + 1/12ZrSi_2\,(s) = 1/12ZrCl_4\,(g) + 1/6SiCl_4\,(g) + Na\,(g)$	1573	$5.2\cdot10^{-3}$	$1.3\cdot10^{-2}$
31	$NaCl\,(g) + 1/3VSi_2\,(s) = 1/3VCl\,(g) + 2/3SiCl\,(g) + Na(g)$	1573	$1.7\cdot10^{-3}$	$1.7\cdot10^{-2}$
32	$NaCl\,(g) + 1/5VSi_2\,(s) = 1/5VCl\,(g) + 2/5SiCl_2\,(g) + Na\,(g)$	1573	$5\cdot10^{-3}$	$2.9\cdot10^{-2}$
33	$NaCl\,(g) + 1/7VSi_2\,(s) = 1/7VCl\,(g) + 2/7SiCl_3\,(g) + Na\,(g)$	1573	$2.6\cdot10^{-3}$	$1\cdot10^{-2}$
34	$NaCl\,(g) + 1/7VSi_2\,(s) = 1/7VCl\,(g) + 2/7SiCl_3\,(g) + Na\,(g)$	1573	$2.6\cdot10^{-3}$	$1\cdot10^{-2}$
35	$NaCl\,(g) + 1/4VSi_2\,(s) = 1/4VCl_2\,(g) + 1/2SiCl\,(g) + Na\,(g)$	1573	$3\cdot10^{-3}$	$2.3\cdot10^{-2}$
36	$NaCl\,(g) + 1/6VSi_2\,(s) = 1/6VCl_2\,(g) + 1/3SiCl_2\,(g) + Na\,(g)$	1573	$1.6\cdot10^{-2}$	$7.4\cdot10^{-2}$
37	$NaCl\,(g) + 1/8VSi_2\,(s) = 1/8VCl_2\,(g) + 1/4SiCl_3\,(g) + Na\,(g)$	1573	$6\cdot10^{-3}$	$2.1\cdot10^{-2}$
38	$NaCl\,(g) + 1/10VSi_2\,(s) = 1/10VCl_2\,(g) + 1/5SiCl_4\,(g) + Na\,(g)$	1573	$4\cdot10^{-3}$	$1\cdot10^{-2}$
39	$NaCl\,(g) + 1/5VSi_2\,(s) = 1/5VCl_3\,(g) + 2/5SiCl\,(g) + Na\,(g)$	1573	$4\cdot10^{-3}$	0.20
40	$NaCl\,(g) + 1/7VSi_2\,(s) = 1/7VCl_3\,(g) + 2/7SiCl_2\,(g) + Na\,(g)$	1573	$7\cdot10^{-3}$	$2.6\cdot10^{-2}$
41	$NaCl\,(g) + 1/9VSi_2\,(s) = 1/9VCl_3\,(g) + 2/9SiCl_3\,(g) + Na\,(g)$	1573	$3.5\cdot10^{-3}$	$1.1\cdot10^{-2}$

method protects the surface of the niobium sample from oxidation in the air for 3 to 9 hours, depending on the test temperature.

Point 3 of Table 1 shows the result of creating a heat-resistant coating by applying a layer of slip on a sample made of niobium and subsequent titanation. Slurry has a composition of 80 Mo + 13.5 Ni + 6.5 Sn % wt. The tin present in the slicker will be in liquid form during the chemical and thermal treatment. Tin at the processing temperature $T = 1150$°C will cover the niobium surface with a thin layer.

In this case, molybdenum and nickel will dissolve in it. During titanation in NaCl vapours, according to reactions 5–8 (Table 2), chlorides of this element are formed. Exposure to this gaseous saturation medium will lead to saturation of the niobium surface with molybdenum and titanium. After that, the samples were borosilicated at a temperature of $T = 1300$°C for 7 hours. As a result of such chemical and thermal treatment of samples, a surface layer consisting of silicides of titanium, molybdenum, nickel and niobium is formed on their surface. Such a coating provides protection of niobium from oxidation in air at a temperature of $T = 1700$°C for 9 hours.

Point 4 of Table 1 presents another option for creating a heat-resistant coating on niobium. The niobium samples were previously hafniated at a temperature of $T = 1300$°C for 7 hours. Hafnium powder was used as a saturating mixture, and to accelerate the rate of diffusion saturation, the process was carried out using sodium chloride vapour. This treatment usually results in the formation of a surface layer containing more than 50% wt. hafnium on the niobium sample. A layer of 35 HfB_2 + 20 $ZrSi_2$ + 20 $MoSi_2$ + 10 TiB_2 + 6.5 Ni + 6.5 Zr + 2 B % wt. was applied to the hafniated surface of the samples, and these samples were placed in a powder mixture of the composition 22 Si + 22 $ZrSi_2$ + + 22 HfB_2 + 31 $MoSi_2$ % wt. After that, the process of chemical-thermal treatment of the samples was carried out in NaCl sodium chloride vapours at a temperature of $T = 1300$°C for 7 hours. Such substances as Si, Zr, HfB2, $ZrSi_2$, $MoSi_2$, and TiB_2 are involved in the process of chemical and thermal treatment. Ni and B components, which are part of the slicker, form a liquid medium on the surface of the sample at the saturation temperature. When the NaCl vapour affects the components involved in the chemical-thermal treatment, a gas-saturated environment is formed. According to points 9–30 of Table 2, its main components will be silicon chlorides, boron chlorides, zirconium chlorides, hafnium chlorides and molybdenum dichloride. This chemical action on the niobium surface will lead to the formation of a diffusion layer. This layer will consist of niobium silicides, zirconium silicides, hafnium silicides, molybdenum silicides, and will contain boron too. Depending on the thermodynamic characteristics of compounds, it is possible to form not only silicides, but also zirconium borides and hafnium borides. This coating provides protection of niobium from exposure to an oxidizing environment at temperature $T = 1700$°C from 9 to 13.5 hours. Figure 1 shows the structure of the heat-resistant layer on the niobium sample. It was also established that re-forming the surface layer provides an increase in the thickness of the protective layer and slightly increases heat resistance.

Heat-resistant coatings were created on niobium and tantalum samples in accordance with points 5 and 6 of Table 1. These samples were chemically and thermally treated in a powder mixture with a composition of 40 $MoSi_2$ + 20 HfB_2 + 20 VSi_2 + 20 Si in the presence of NaCl vapour at a temperature of $T = 1310$°C during 7 hours. According to Table 2, at this temperature, silicon chlorides, hafnium chlorides and boron chlorides, vanadium chlorides and molybdenum dichloride will be present in the reaction space; these are reactions 9–11, 14–18, 31–41, respectively.

The influence of the gaseous components of the saturating medium listed above on the niobium surface will lead to the formation of a protective layer consisting of a number of components. These will be niobium silicides, hafnium silicides, vanadium silicides, molybdenum sil-

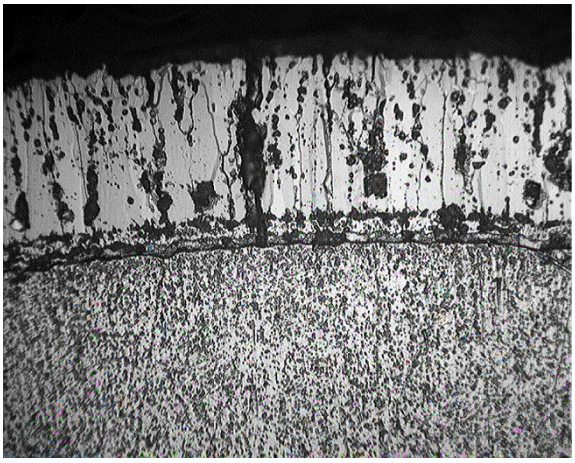

Fig. 1. Image of a cross-section of a niobium sample with a heat-resistant coating obtained according to point 4, Table 1 (×400).

icides, and some boron-based compounds. As you know, each of these metals (niobium, hafnium, vanadium, and molybdenum) has several silicides. If we also take into account possible borides, then, the total number of components of the surface layer turns out to be significant. When the gaseous oxidizing medium acts on this treated niobium surface, a film is formed consisting of oxides of niobium, hafnium, vanadium, and silicon. When creating a protective coating on tantalum, point 6 (Table 1), the picture will be similar. Such coatings provide protection of niobium and tantalum from oxidation in air at a temperature of 1800°C. The conducted studies showed that repeating the process of forming the surface layer leads to an increase in the thickness of the protective coating and, thus, it is possible to increase the heat resistance of the samples to the maximum value.

In Table 1, points 7 and 8 present the method of creating a heat-resistant coating on niobium and tantalum samples. These samples were placed in a powder filling with a composition of 40 Si + 30 HfB_2 + 30 $ZrSi_2$ % wt. After that, the samples were chemically and thermally treated in the presence of NaCl vapours at a temperature of $T = 1300$°C for 7 hours. During this process, a gaseous saturating medium is formed. Silicon, hafnium diboride and zirconium disilicide are included in the powder filling. These components under the influence of NaCl steam at a process temperature $T = 1300$°C and a pressure of 1 to 10^2 Pa form silicon chlorides, hafnium chlorides and boron chlorides, zirconium chlorides, these are reactions 9–11, 15–18, 19–30 presented in Table 2, respectively. The effect of this gaseous saturation medium on the surface of niobium or tantalum will lead to the formation of a diffusion layer consisting of a large number of compounds. The diffusion

layer on niobium will consist of niobium silicides, hafnium silicides, zirconium silicides, as well as the possible presence of compounds of these metals with boron. A tantalum sample will have a layer of tantalum silicides and components similar to those present on the surface of a niobium sample. Such a complex coating provides protection of niobium and tantalum samples from oxidation in air at a temperature of $T = 1900°C$ for 30 minutes.

Table 2 shows the results of calculations of the possibility of chemical reactions taking place in the reaction space, allowing a deeper understanding of the essence of the process of formation of a protective coating. All reactions describing the interaction of NaCl vapour with the components of the powder saturating mixture proceed with an increase in volume. In this case, they will be better implemented with a decrease in pressure. In addition, with a decrease in pressure, the share of lower chlorides will increase. On the other hand, the reactions describing the interaction of the gaseous saturated medium with the treated surface proceed with a decrease in volume. For example, these are reactions 3, 4 (Table 2). Therefore, when the treated surface is saturated, an increase in pressure will contribute to an increase in the concentration of the injected substance. The composition of the gas saturation medium and the pressure in the reaction space will affect the process of chemical and thermal treatment of samples. The flow of the activator and its pressure in the reaction space depend on the partial pressure of NaCl, which is determined by its temperature. On the other hand, this value is affected by the pumping speed of the vacuum system, which removes the gas mixture from the reaction container. The speed of pumping from the reaction volume depends primarily on the particle size of the powder filler used to saturate the samples. As follows from the above, it is necessary to create optimal conditions to achieve the maximum results of the formation of a diffusion layer on the surface of the samples.

4. CONCLUSIONS

1. The method of vacuum activated diffusion saturation with the use of a preliminary application of a slicker layer on the surface of niobium and tantalum samples allows you to create continuous non-porous coatings on their surface.
2. It was established that repeated application of the surface layer on niobium and tantalum samples leads to an increase in the thickness of the protective coating and helps to increase its heat resistance.
3. Pre-saturation of the niobium surface with such metals as chromium, titanium, hafnium followed by chemical and thermal treatment of the samples helped to increase the heat resistance of the overall coating.
4. As follows from the analysis of the obtained results, it was estab-

lished that preliminary saturation of the niobium surface with refractory metals followed by silicification improves the heat resistance of the coating with an increase in the heat resistance of silicides—chromium, titanium, and hafnium.

REFERENCES

1. V. I. Zmiy, H. M. Kartmazov, and S. H. Ruden'kyy, *Sposib Dyfuziynoho Nasychennya Poverkhon' Vyrobiv* [The Method of Diffusion Saturation of Product Surfaces], Patent of Ukraine No. 98074 (Published April 10, 2012) (in Ukrainian).
2. V. I. Zmiy, H. M. Kartmazov, and S. H. Ruden'kyy, *Prystriy dlya Dyfuziynoho Nasychennya Poverkhon' Vyrobiv u Vakuumi* [Device for Diffusion Saturation of Product Surfaces in a Vacuum], Patent of Ukraine No. 98087 (Published April 10, 2012) (in Ukrainian).
3. V. I. Zmiy, S. H. Ruden'kyy, Ye. V. Tymofyeyeva, A. A. Kornyeyev, V. V. Kunchenko, Yu. V. Kunchenko, T. P. Ryzhova, and M. Yu. Bredykhin, *Poroshkova Metalurgiya*, No. 7/8: 151 (2015) (in Ukrainian).
4. V. I. Zmiy and S. G. Ruden'kiy, *Reaktsionno-Aktivirovannaya Diffuziya i Vakuumnyye Pokrytiya* [Reaction-Activated Diffusion and Vacuum Coatings] (Kharkiv: NSC 'KhIPT', N.A.S. of Ukraine: 2010) (in Russian).
5. S. G. Ruden'kiy, *Fiziko-Khimicheskie Osnovy Aktivirovannogo Vakuumnogo Metoda Formirovaniya Mnogofunktsional'nykh Pokrytiy na Metallicheskikh i Uglerodnykh Materialakh* [Physico-Chemical Foundations of the Activated Vacuum Method for the Formation of Multifunctional Coatings on Metal and Carbon Materials] (Thesis of Disser. for Dr. Sci.) (Kharkiv: Institute of Electrophysics and Radiation Technologies, N.A.S. of Ukraine: 2014) (in Russian).
6. S. Rudenkyj and V. Zmij, *Multipurpose Vacuum-Diffusion Protective Coatings on Metallic and Carbon Base Materials* (LAP Lambert Academic Publishing: 2017).

Metallophysics and Advanced Technologies
Металофіз. новітні технол.
Metallofiz. Noveishie Tekhnol.
2024, vol. 46, No. 5, pp. 491–505
https://doi.org/10.15407/mfint.46.05.0491
Reprints available directly from the publisher

PACS numbers: 68.55.J-, 81.15.Pq, 81.65.Kn, 82.45.Bb, 82.45.Hk, 82.45.Jn, 82.45.Qr

Electrocatalytic and Corrosion Properties of CoWRe Alloys Electrodeposited from a Citrate-Pyrophosphate Electrolyte

Yu. S. Yapontseva, T. V. Maltseva, and V. S. Kublanovsky

V. I. Vernadsky Institute of General and Inorganic Chemistry, N.A.S. of Ukraine,
32/34 Academician Palladin Ave.,
UA-03142 Kyiv, Ukraine

This work presents studies of the electrocatalytic properties of ternary CoWRe alloys during the hydrogen-evolution reaction in KOH solution and their corrosion properties in KOH, H_2SO_4 and NaCl solutions. These alloys are electrodeposited from a citrate-pyrophosphate electrolyte with potassium-perrhenate concentrations of 0.01, 0.03, and 0.05 mol·l^{-1}. As shown, the use of such alloys makes it possible to increase the exchange current density by an order of magnitude and reduce the hydrogen overvoltage by 150 mV compared to electrolytic cobalt. An increase in the content of rhenium in the alloy leads to an increase in the overvoltage of hydrogen evolution in alkaline solutions: both in the KOH solution and in the electrolyte for the deposition of the alloy that explains the high current efficiency when obtaining alloys' coatings. As shown, the highest corrosion resistance of such coatings with the ratio Re:W = 2:4 reaches 8.9 kΩ·cm^2 in NaCl solution, and in KOH solution, it is of 3.1 kΩ·cm^2, and corrosion resistance increases in time.

Key words: cobalt, tungsten, rhenium, electrodeposition, corrosion, electrocatalysis.

У роботі представлено дослідження електрокаталітичних властивостей потрійних стопів CoWRe у реакції виділення Гідроґену в розчині KOH та корозійних властивостей цих стопів у розчинах KOH, H_2SO_4 та NaCl. Стопи електроосаджували з цитратно-пірофосфатного електроліту з концентрацією перренату Калію у 0,01, 0,03 і 0,05 моль·л$^{-1}$. Показано, що використання таких стопів дає змогу на порядок збільшити густину струму

Corresponding author: Yuliya Serhiyivna Yapontseva
E-mail: juliya yap@ukr.net

Citation: Yu. S. Yapontseva, T. V. Maltseva, and V. S. Kublanovsky, Electrocatalytic and Corrosion Properties of CoWRe Alloys Electrodeposited from a Citrate-Pyrophosphate Electrolyte, *Metallofiz. Noveishie Tekhnol.*, **46**, No. 5: 491–505 (2024).
DOI: 10.15407/mfint.46.05.0491

обміну Гідроґену та зменшити перенапругу Гідроґену на 150 мВ порівняно з електролітичним Кобальтом. Збільшення вмісту Ренію у стопі приводить до збільшення перенапруги виділення Гідроґену в лужних розчинах — як в розчині KOH, так і в електроліті для осадження стопу, що пояснює високі значення виходу за струмом під час одержання покриттів з таких стопів. Показано, що корозійна стійкість покриттів є найбільшою за співвідношення Re:W = 2:4; опір корозії сягає 8,9 кОм·см^2 у розчині NaCl, а у розчині KOH — 3,1 кОм·см^2 та з часом зростає.

Ключові слова: Кобальт, Вольфрам, Реній, електроосадження, корозія, електрокаталіза.

(Received 5 October, 2023; in final version, 10 January, 2024)

1. INTRODUCTION

The modern development of hydrogen fuel cell and internal contribution engine technologies creates good prospects for the development of method for the production, storage and use of eco-friendly hydrogen fuel. As was pointed out in [1–3], the increase in power consumption in the world and striving for using renewable power sources put pure hydrogen production among important and urgent tasks. The electrolytic method of hydrogen production is a highly efficient, but expensive method because of the cost of electrocatalysts based on platinum metals. Thin-layer coatings of base metal alloys can solve this problem thanks to deposition onto a cheaper metallic substrate and modifying the surface to impart the required functional properties to it.

Among the various methods of applying protective functional coatings, such as chemical deposition, thermal spraying and vapour deposition, the galvanic method occupies a special place, since it allows one to obtain coatings of a given composition and structure.

It is known that electrolytic binary refractory metals alloys with iron subgroup metals (including CoW and CoRe) exhibit electrocatalytic properties in the hydrogen evolution reaction (HER) in acidic and alkaline solutions [4–9]. The difference between rhenium alloys and alloys of other refractory metals (molybdenum and tungsten) is that the rhenium content in coatings can be varied over a very wide range (11–80 at.%), while, for tungsten alloys [9], the concentration of the refractory component at electrodeposition from similar solutions does not exceed 30 at.%. It was shown in [8] that CoRe alloys exhibit the highest electrocatalytic activity (EA) at low (20–30 at.%) and high (> 60 at.%) concentrations of refractory metal.

Ternary CoWRe alloys deposited from an acidic citrate electrolyte also exhibit electrocatalytic activity in HER [10, 11]. The use of ternary alloys makes it possible to arise significantly the exchange current density of hydrogen and to reduce hydrogen evolution overvoltage

compared to binary alloys. In [10, 11], the concentration of perrhenate ions was 0.01 mol/l, and the concentration of rhenium in the ternary alloy did not exceed 40%. In the present work, the concentration range of potassium perrhenate in the electrolyte for the deposition of alloys was extended in comparison with [10, 11] and amounted to 0.01–0.05 mol/l. The aim of our work was to study the electrocatalytic properties of CoWRe ternary alloys deposited from a citrate-pyrophosphate electrolyte, the use of which makes it possible to increase the rate of the electrodeposition process and obtain high-quality uniform coatings with a higher current efficiency relative to the citrate deposition electrolyte and with a high content of rhenium and tungsten in the coatings.

A technical characteristic required for the use of new electrocatalysts is their stability in aggressive medium. Therefore, it is necessary to investigate the corrosion properties of coatings in solutions, which are used to produce electrolytic hydrogen, *i.e.* KOH and H_2SO_4, and in a simulated corrosive NaCl solution in order that the characteristics of the materials obtained can be compared with literature data on similar materials.

Corrosion properties of electrolytic alloys Co–W in solutions of H_2SO_4 and NaCl were studied in [12–14]. It is shown that coatings containing 17–24 at.% W have the highest corrosion resistance, which practically correspond to the composition of the Co_3W intermetallic phase, as well as to the transition from the polycrystalline to amorphous structure of the coatings. It was found that the resistance of the coatings significantly changes with prolonged exposure of the sample in a NaCl solution, so after 12 hours it decreases from 7.12 $k\Omega/cm^2$ to 0.97 $k\Omega/cm^2$.

One of the ways to increase the corrosion resistance of electrolytic coatings with alloys of refractory metals is the electrodeposition of ternary alloys containing two refractory metals (tungsten and molybdenum) [15, 16] with a total content for ones of 15–20 at.%. Improvement of the mechanical and electrochemical properties of such alloys in comparison with binary ones can be achieved using the pulsed electrolysis mode. It is shown that with an increase in the total content of refractory metals in CoMoW coatings, the corrosion rate decreases in an acidic medium in comparison with alloys containing only one of the refractory metals and increases in an alkaline medium due to the instability of molybdenum and tungsten oxide.

We have investigated [17] electrodeposition of ternary cobalt alloys also containing two refractory metals: tungsten and rhenium. The paper shows the dependence of the chemical and phase composition, current efficiency and microhardness of ternary CoWRe alloys on the concentration of the components of deposition electrolytes and the electrolysis mode. Since tungsten and rhenium are corrosion-resistant metals, it can be expected that electrolytic coatings with alloys of these metals will exhibit significant corrosion resistance in corrosive envi-

ronments. This work presents a study of the electrocatalytic activity and corrosion resistance of coatings obtained under the same conditions. We assume that the coprecipitation of rhenium into the ternary CoWRe alloy will improve the functional characteristics of coatings, as we showed for the CoMoRe alloy in [18].

2. EXPERIMENTAL DETAILS

2.1. Materials and Synthesis

The electrodeposition of CoWRe alloys was carried out from citrate-pyrophosphate electrolytes containing (mol/l): $CoSO_4 \cdot 7H_2O$—0.1, $Na_2WO_4 \cdot 2H_2O$—0.2, $Na_3C_6H_5O_7 \cdot 7H_2O$—0.2, $K_4P_2O_7$—0.2, $Na_2SO_4 \cdot 10H_2O$—0.3 and $KReO_4$ for electrolyte No. 1—0.01, No. 2—0.03 and No. 3—0.05 at pH 9.0.

Deposition was carried out in a thermostated cell at a temperature of 50°C in a galvanostatic mode using a LIPS-35 direct current source under forced convection at a magnetic stirrer rotation speed of 300 rpm. As a working electrode, a copper plate with an area of 0.25 cm^2 was used, on the surface of which a layer of electrolytic cobalt was deposited from an acidic sulphate-chloride electrolyte of the following composition, g/l: $CoSO_4 \cdot 7H_2O$—504, NaCl—17, H_3BO_3—45 [19] at a current density of 3 mA/cm^2 for an hour. The anode was a platinum wire.

2.2. Study of Chemical Composition and Morphology

The morphology and chemical composition of samples were studied by using a JSM-6700F field emission scanning electron microscope equipped with a JED-2300 energy-dispersive spectrometer (JEOL). Operating conditions were as follows: 20 kV accelerating voltage, 0.75 nA beam current, 1 μm beam size. Counting time for EDS analyses was 60 s. Pure W and Re were used as standards. Raw counts were corrected for matrix effects with the ZAF algorithm implemented by JEOL. Three to five spots per each sample were analysed.

2.3. Study of the Alloys Properties in the Hydrogen Evolution Reaction

Voltammetric measurements of the electrocatalytic properties of alloys in the hydrogen evolution reaction were carried out in a solution of 1.0 mol/l KOH under natural convection conditions in a thermostated cell with separated cathode and anode spaces at a temperature of 20°C. To obtain the j–E dependences, a ПИ-50-1.1 potentiostat and a ПР-8 programmer were used. Stationary polarization curves were obtained in potentiostatic mode with a step of 20 mV.

2.4. Corrosion Measurements

The study of corrosion was carried out by impedance spectroscopy and voltammetry using the AUTOLAB system (GPSTAT 20 + FRA) with the GPES 4.9 software in solutions, mol/l: 0.01—H_2SO_4, 3.5% NaCl, 1.0—KOH; at a temperature of 20 ± 1°C in a cell assembled according to a three-electrode circuit with a saturated silver-chloride reference electrode and an auxiliary electrode in the form of a platinum grid. All potentials in this work are given relative to a saturated hydrogen electrode. Cathodic and anodic polarization curves were obtained with a potential task rate of 1.0 mV/s. Analysing the data of polarization measurements in the stationary potential region (± 100 mV), the resistances and corrosion currents were calculated. The electrochemical impedance spectra were recorded after keeping the sample in a corrosive solution for 10 minutes for the potential to reach a steady—state value. The voltage was applied sinusoidally with amplitude of 5 mV. The spectra have been obtained in a frequency range of 5.0 kHz–20 MHz. The parameters of the corrosion process have been determined from an analysis of the spectra obtained.

3. RESULTS AND DISCUSSION

3.1. Chemical Composition and Morphology

Figure 1 shows the effect of the deposition current density and rhenium ion concentration in the solution on the rhenium and tungsten content of alloys (the residue is cobalt). It can be seen that the amount of refractory metals in coatings under experimental conditions is not over 47 at.%, *i.e.*, the basic metal in the alloy is cobalt. The rhenium content of the coating increases with current density and potassium perrhenate concentration from 13 at.% to 44 at.%, and the tungsten content decreases from 11 at.% to 3 at.%.

The electrolysis conditions and electrolyte composition have the same synchronous effect on the morphology of coatings, *i.e.*, when the deposition current density and rhenium ion concentration in the solution are increased, the size of surface agglomerates increases by two orders of magnitude from 0.1 μm to 10 μm. Figure 2 shows micrographs of coatings having the greatest differences: minimum rhenium content and a current density of 5 mA/cm^2 (*a*) and high rhenium content and a current density of 30 mA/cm^2 (*b*).

3.2. Properties of Alloys in the Hydrogen Evolution Reaction

Figure 3 shows the voltammetric dependences of hydrogen evolution in

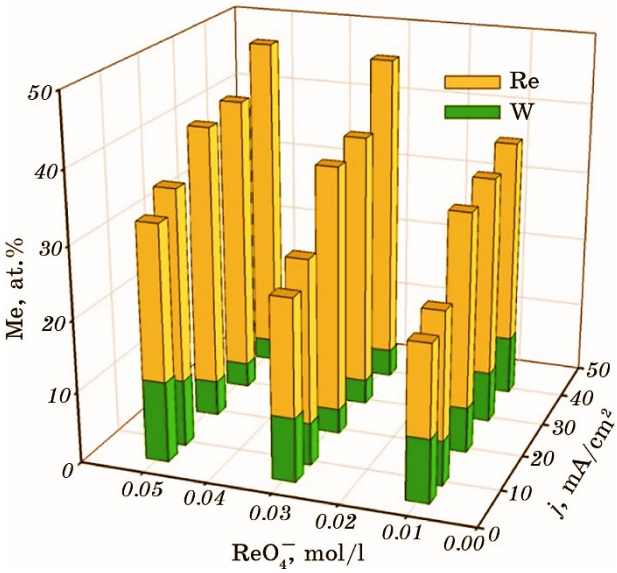

Fig. 1. Dependence of the percentage of refractory metals in CoWRe alloys on the deposition current density and potassium perrhenate concentration in the electrolyte.

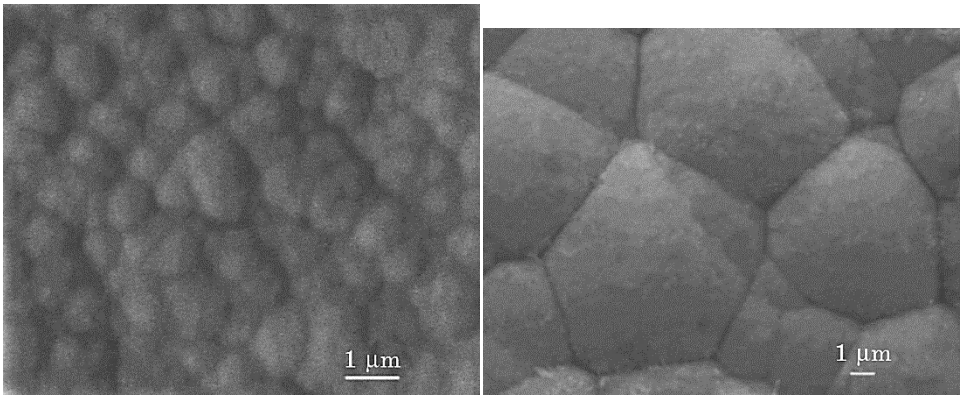

a *b*

Fig. 2. Surface morphology of CoWRe alloys electrodeposited from electrolyte No. 1 at current densities of 5.0 mA/cm² (*a*) and No. 3 at 30.0 mA/cm² (*b*) (reprint from [17]).

a KOH solution on CoWRe alloys electrodeposited from electrolytes Nos. 1–3 in the current density range of 5–30 mA/cm².

To compare the effect of the chemical composition of coatings on their electrocatalytic properties, the figure shows the voltammetric

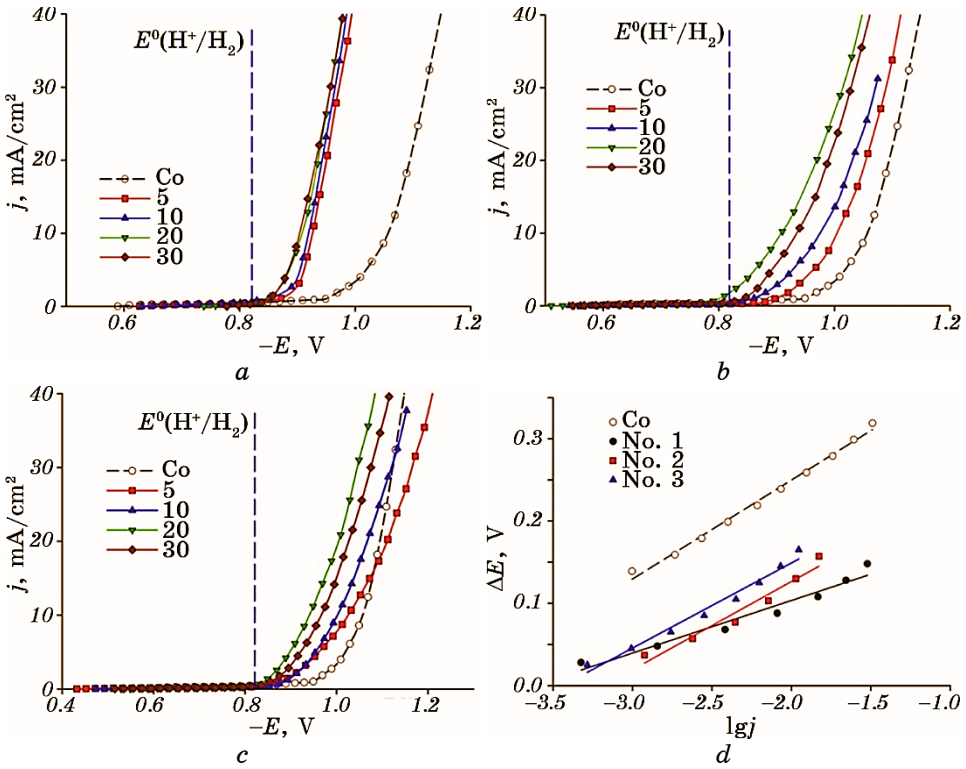

Fig. 3. Voltammetric curves of hydrogen electroreduction on CoWRe alloys electrodeposited from electrolytes No. 1 (*a*), No. 2 (*b*), No. 3 (*c*) and the Tafel section for Co and alloys deposited at 20 mA/cm^2 (*d*).

characteristic for a pure electrolytic cobalt cathode deposited from an acidic sulphate electrolyte.

The presented dependences show that an increase in the electrodeposition of potassium perrhenate in the solution, and, consequently, the amount of rhenium in the alloy, leads to a significant change in the properties of the coatings. Thus, in comparison with pure cobalt, the coatings obtained from electrolyte No. 1 exhibit good electrocatalytic properties; the coatings deposited from electrolyte No. 2 only slightly reduce the overvoltage of hydrogen evolution, and the properties of the coatings obtained from electrolyte No. 3 are comparable to those of cobalt. The figure also shows that the best electrocatalytic properties are exhibited by coatings deposited at 20 mA/cm^2. For these alloys Fig. 3, *d* shows the Tafel sections, and it can be seen from data the best catalyser is alloy, deposited from electrolyte No. 1.

To determine the kinetic parameters of the hydrogen evolution reaction, all experimental dependences were rearranged in semi-logarithmic

coordinates. Previously, we found significant differences in the value of the hydrogen exchange current density on the surface of electrolytic cobalt [20, 21]. Under the conditions of our experiment for cobalt, the Tafel slope is 120 mV, which indicates that the limiting stage of sum reaction is the transfer of the first electron, *i.e.*, the Volmer reaction, and the logarithm of the hydrogen exchange current density is of –4.08.

In the case of ternary alloys, a much more complex picture is observed. Based on the Sabatier principle and volcano-like dependence, rhenium is the closest metal to platinum in terms of the Me–H bond energy and hydrogen exchange current density, and also belongs to the group of metals that are characterized by the limiting stage of electrochemical desorption (Heyrovsky reaction), as well as for platinum [22]. In the presence of rhenium, the coefficient *b* changes significantly and for alloys deposited from electrolyte No. 1 is 78–72 mV, for coatings deposited from electrolyte No. 2 is 107–96 mV, and for No. 3 is 129–103 mV with increasing current density of alloy deposition.

When analysing the experimental data, several factors should be taken into account: an increase in the degree of surface coverage with atomic hydrogen as the cathodic polarization increases; oxides of tungsten and rhenium are always present on the surface of alloys of these metals, formed as a result of contact with air, as well as in case of incomplete electroreduction of salts of these metals in solution, while part of the formed hydrogen atoms can be spent on the reduction of these oxides; the ability of rhenium to absorb hydrogen. These factors contribute to a change in the surface of the alloys and the experimental results obtained. The authors of [23] performed calculations of the kinetic parameters of different stages of hydrogen electroreduction taking into account such changes and came to the conclusion that a high content of rhenium on the surface can lead to the fact that the Volmer and Heyrovsky reactions can proceed with comparable rates, which is why Tafel slope is 60–80 mV. The authors of [24] came to a similar conclusion. However, the value of the coefficient b in our case cannot serve as an unambiguous proof of a change in the reaction mechanism; the changes can also indicate that the experimental data are distorted precisely due to the mentioned changes in the alloy surface.

If we assume that the mechanism of hydrogen electroreduction does not change, then the Volmer reaction, which is the limiting stage for metals of the iron group (including cobalt), occurs quickly and reversibly on the surface of tungsten and rhenium, and the reaction of electrochemical desorption, on the contrary, is limiting for refractory metals and reversible for cobalt. Thus, to create effective electrocatalysts, it is necessary to take into account that there should be metal atoms on the surface, on which an electrochemical reaction occurs at a high rate (refractory metals W, Re, Mo) and the amount of these atoms should be sufficient for the possibility of surface diffusion of hydrogen

adatoms (spill over effect). However, a large number of refractory metal atoms leads to a decrease in the number of cobalt atoms, on which the stage of electrochemical desorption rapidly occurs to remove hydrogen from the surface and the rate of the entire process decreases.

Despite the generality of the mechanism of hydrogen evolution, the refractory metals W, Re, and Mo differ significantly in their properties, while the common thing is that to achieve the electrocatalytic effect, the amount of refractory metals (one or two at the same time) must be in the range of 10–30 at.%.

The dependence of the exchange current density for cobalt and CoWRe alloys (Fig. 4, *a*) shows that the use of ternary alloys makes it possible to reduce $j_0(H_2)$ by an order of magnitude compared to pure cobalt when the rhenium content in the alloy is 6–10 times more than the content of tungsten. However, in this case, it is necessary to take into account the differences in the value of the coefficient *b* for different coatings. Regardless of the reasons for these differences (change in the mechanism or change in surface properties), the exchange current density calculated for different values of *b* cannot be compared with each other and unambiguously judge the magnitude of the electrocatalytic effect; therefore, Fig. 4, *b* shows a similar dependence for hydrogen overvoltage. This dependence shows that the use of alloys deposited from electrolyte No. 1 can reduce the hydrogen overvoltage by 150 mV and the more rhenium is in the deposition electrolyte and in the coating, the less this effect becomes.

When comparing the dependences of the electrocatalytic properties of coatings in a KOH solution and the current efficiency of alloys during their electrodeposition from a citrate-pyrophosphate electrolyte [14] on their chemical composition, it can be seen that during the ca-

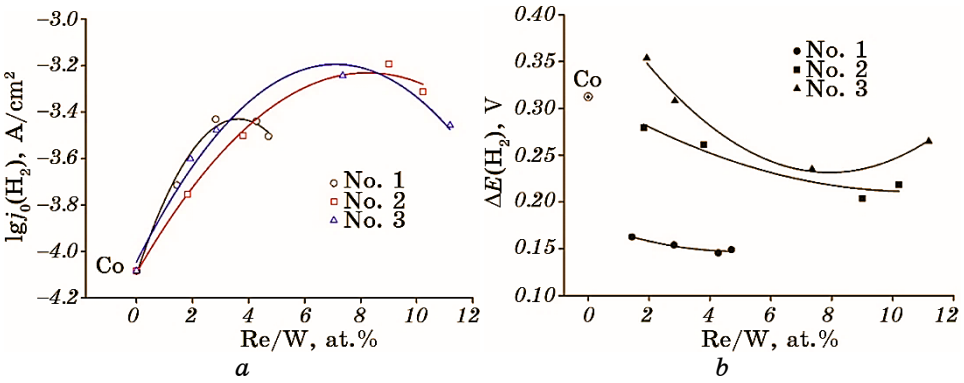

Fig. 4. Dependence of the hydrogen exchange current on CoWRe alloys deposited from electrolytes 1–3, respectively (*a*) and hydrogen overvoltage at 30 mA/cm^2 (*b*) on the ratio of refractory metals in the alloy.

thodic process on the alloy surface in an alkaline medium, these dependences have opposite tendencies. That is, the ability of the coating to reduce the hydrogen evolution overpotential is manifested not only in the KOH solution, but also in the process of the formation of the alloy itself in a weakly alkaline deposition electrolyte. With an increase in the concentration of potassium perrhenate in the electrolyte, and hence an increase in the amount of rhenium in the coating (electrolytes Nos. 1–3), the value of the current efficiency, and, consequently, the rate of deposition of alloys, increases markedly and at a rhenium content of 35–45 at.% reaches the maximum value under experimental conditions 93%. This value of the current efficiency of the CoWRe ternary alloy is not typical for the electrodeposition of alloys of refractory metals with metals of the iron subgroup and can be explained precisely by the properties of ternary alloys in the hydrogen evolution reaction, which is a side and undesirable reaction during alloy electrodeposition, and a target reaction in a KOH solution. Thus, the formation and growth of an alloy capable of electrocatalysis of a hydrogen reaction leads to a significant decrease in the current efficiency during its production, which is observed for coatings deposited from electrolyte No. 1. On the contrary, the alloys deposited from electrolyte No. 3 have a high overvoltage of hydrogen evolution and therefore they themselves are released with the highest current efficiency up to 93%.

3.3. Corrosion Studies

It is known that each of the refractory metals (tungsten and rhenium) has a high corrosion resistance. In this case, as was shown in Ref. [8], the corrosion resistance of a binary electrolytic alloy is an intermediate value between the corrosion resistances of pure metals. For ternary alloys [11], a difference was shown in the corrosion resistance of crystalline and x-ray amorphous coatings. So, crystalline coatings are formed at a low content of rhenium in the alloy (up to 20–25 at.%). As the rhenium content increases, a transition to x-ray amorphous (nanocrystalline) alloys is observed. During electrodeposition from acidic citrate solutions [11], crystalline coatings are formed at deposition current densities of 20–40 mA/cm^2 and have the highest corrosion resistance. Nanocrystalline coatings demonstrate lower corrosion resistance in all studied corrosive solutions. In this work, we studied the influence of the chemical composition and conditions of electrodeposition from polyligand electrolytes of the CoWRe ternary alloy on the corrosion resistance of coatings in media with different pH. The study of the corrosion properties of alloys of refractory metals in a KOH solution is of great importance, since these materials are considered by modern researchers as the most promising electrocatalysts for producing pure hydrogen. In electrolysers, both acidic and alkaline electrolytes are used to produce

hydrogen, but the use of KOH solutions has become more widespread precisely because of the greater corrosion resistance of the electrodes.

The current–voltage curves of corrosion of CoWRe alloys (deposited at the same current density of 10 mA/cm^2) in a solution of KOH, NaCl, H_2SO_4 and the dependence of the specific corrosion resistance on the ratio of rhenium and tungsten concentrations in coatings during corrosion in a NaCl solution are shown in Fig. 5. Figure 5, *a* shows the difference in potentials and corrosion currents in various corrosion solutions, as well as in the behaviour of alloys during anodic polarization. This deposition current density was chosen because the coatings obtained under these conditions have the most corrosion resistant. Experimental current–voltage dependences for samples obtained at other current densities have a similar form and therefore are not shown in the figure.

A feature of corrosion of coatings in an alkaline solution is the presence of a dissolution peak before reaching the limiting current. This behaviour is associated with the dissolution of one of the phases on the alloy surface, which begins at anodic polarization of ≅ 300 mV from the corrosion potential and is probably related to the dissolution of the component that is least stable in an alkaline environment, namely, cobalt. The current–voltage curves show that the potential of the corrosion process shifts to the negative side with an increase in the current density of the deposition of coatings, which is explained by a change in their chemical composition, in particular, an increase in the amount of rhenium in the alloy. The corrosion resistance of the studied coatings is quite high, more than 3 kΩ·cm^2 (Table 1), and the optimal ratio of refractory metals for corrosion protection in an alkaline environment is Re:W = 3–4. Obviously, the corrosion characteristics depend not only on the chemical, but also on the phase composition.

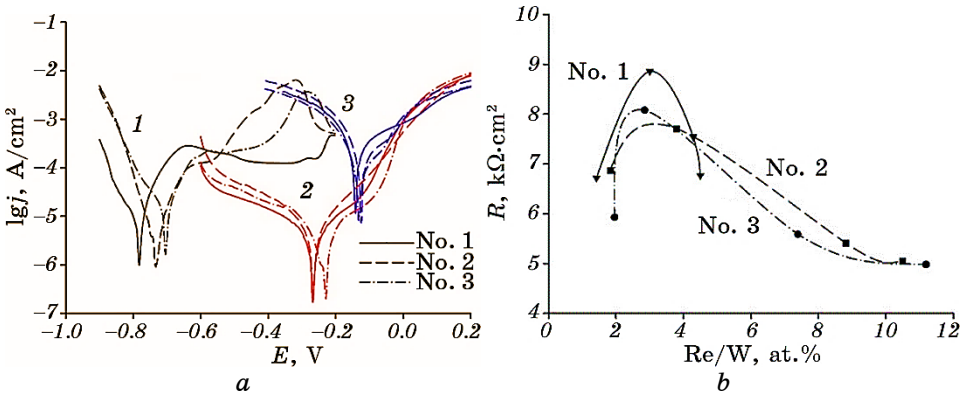

Fig. 5. Voltammetric curves of corrosion of CoWRe alloys, deposited at 10 mA/cm^2, in a KOH (*1*), NaCl (*2*), H_2SO_4 (*3*) solution (*a*) and dependencies of corrosion resistance on Re/W concentration ratio.

TABLE 1. Potential (E), current (j) and resistance (R) of corrosion represented for alloys deposited at 10 mA/cm^2.

Electrolyte/Alloy	Corrosion media	E_{corr}, V	$j_{corr}\cdot10^5$, A/cm^2	R, kΩ·cm^2
No. 1/76Co18Re6W	1 M KOH	–0.783	1.6	3.14
No. 2/71Co23Re6W	1 M KOH	–0.734	2.0	2.49
No. 3/64Co27Re9W	1 M KOH	–0.705	2.7	1.35
No. 1/76Co18Re6W	3.5% NaCl	–0.267	0.6	8.86
No. 2/71Co23Re6W	3.5% NaCl	–0.266	0.8	7.71
No. 3/64Co27Re9W	3.5% NaCl	–0.228	0.7	8.08
No. 1/76Co18Re6W	0.01 M H_2SO_4	–0.142	20.0	0.29
No. 2/71Co23Re6W	0.01 M H_2SO_4	–0.125	18.3	0.32
No. 3/64Co27Re9W	0.01 M H_2SO_4	–0.131	15.9	0.37

In our work [17], the results of x-ray phase analysis of alloys deposited from electrolyte No. 2 at various current densities were presented, and it was shown that the peak of the crystalline phase is observed only in the case of deposition at a low current density of 5 mA/cm^2, *i.e.*, with a low content of rhenium in the alloy. This peak was attributed to the $W_{0.8}Re_{0.2}$ intermetallic compound. Our further studies show that the peak at the same values of Θ also corresponds to a solid solution of rhenium in cobalt; the value of Θ is due to the deformation of the crystal lattice of cobalt during the formation of a solid solution, since the radius of the rhenium atom is larger than that of cobalt. Thus, the high values of the corrosion resistance of coatings deposited at low current densities can be due to the formation of a solid solution of rhenium in cobalt and a tungsten-rhenium intermetallic compound during electrodeposition. Alloys obtained at current densities > 10 mA/cm^2 are x-ray amorphous and it is not possible to determine their exact phase composition by this method.

A study of the corrosion of CoWRe alloys in sulfuric acid shows that, regardless of the chemical composition of the coatings and the electrolysis mode, the current–voltage curves for all the obtained samples practically coincide. The corrosion potential of all samples varies in a narrow range of 40 mV and shifts to the positive side with an increase in the rhenium content. Studies show that the obtained coatings have the least resistance in sulfuric acid, which is explained by the ability of refractory metals, which should provide corrosion resistance, to dissolve in an acidic environment with the formation of tungstic and perrhenic acids. The highest corrosion resistance under these conditions was obtained up to 370 Ω·cm^2.

During corrosion in a NaCl solution, two regions of limiting currents are observed on the anodic branch of the polarization curves, and

the potential for reaching the second limiting current ($E \approx 0.2$ V) does not depend on the composition of the alloy and the corrosion potential. Therefore, it can be assumed that the first limiting current is of a diffusion nature and is associated either with the delivery of a depolarizer or with the removal of reaction products from the surface, and the second is with the formation of oxide compounds on the surface. However, the oxide film is not dense and cannot protect the coating due to surface activation in the chloride solution, so further dissolution occurs at a constant rate, the same for all coatings. In Figure 5, *b*, it can be seen that there is an area of optimal ratio of components, at which the highest corrosion resistance is observed. Therefore, to protect against corrosion in a chloride solution, the content of rhenium in the coating should be 2–4 times higher than that of tungsten. Such a ratio of refractory components is formed during electrodeposition at low current densities of 5–10 mA/cm^2. Similar results were obtained both in alkaline and acid corrosive solutions.

Obviously, the corrosion characteristics largely depend on the crystal structure of the alloy. In the case of ternary CoWRe alloys deposited from both acidic citrate and polyligand citrate pyrophosphate electrolytes, alloys with a pronounced crystal structure and containing a small amount of rhenium have the highest corrosion resistance. At the same time, the ratio of refractory metals in the alloy is also important, where Re:W = 2–4 is optimal. The corrosion properties of coatings are also directly related to the electrocatalytic properties in the hydrogen evolution reaction. With an increase in the content of rhenium in the alloys due to an increase in the concentration of perrhenate ions in the solution or an increase in the deposition current density, the electrocatalytic properties of the alloys in HER deteriorate, *i.e.*, the overvoltage of hydrogen evolution increases. In the case of corrosion processes, this means that the depolarizer recovery rate decreases. Since the corrosion process takes place without access to oxygen, the only possible depolarizer is hydrogen. Decreasing the recovery rate of the depolarizer reduces correspondingly the rate of the corrosion process as a whole.

When assessing the possibility of using coatings as electrocatalysts, information on the corrosion stability of the material in time is needed. The authors of [14] showed that in the case of binary CoW alloys, the corrosion resistance in the simulated corrosive solution decreases within 12 hours by a factor of over 4. The KOH solution, which is mainly used to produce pure hydrogen, is still more aggressive, and this rapid loss of stability of electrodes is inadmissible. Using electrochemical impedance spectroscopy, we have studied the behaviour of a ternary CoWRe alloy deposited from electrolyte No. 3 at a current density of 10 mA/cm^2 in a KOH solution during 24 hours (Fig. 6).

Figure 6 shows a fivefold increase in corrosion resistance within 24 hours. This behaviour shows a gradual slow surface passivation owing

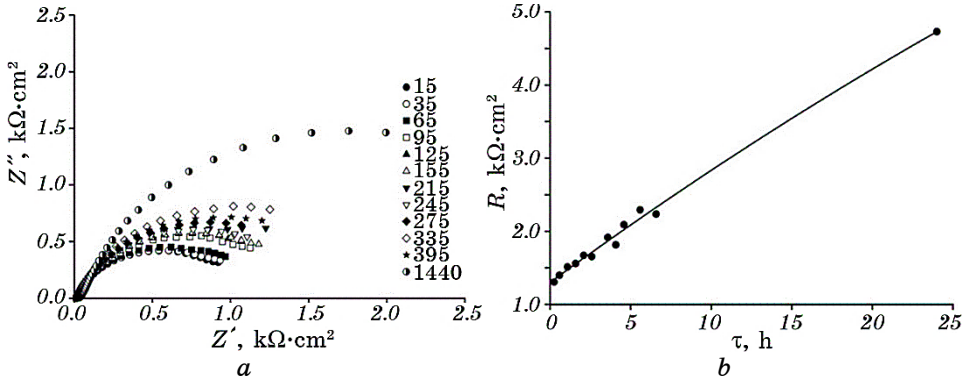

Fig. 6. Electrochemical impedance spectra (*a*) (the holding time in the solution is given in the figure in min.) and the time dependence of corrosion resistance (*b*).

to the formation of refractory metal oxide compounds.

4. CONCLUSION

The properties of alloys in the hydrogen evolution reaction in a KOH solution depend on the rhenium content in the coatings. Thus, an increase in the amount of rhenium in the precipitate leads to a significant increase in the overvoltage of hydrogen evolution, which affects negatively on the process of obtaining hydrogen in a KOH solution, but positively on the process of growing the precipitate in an electrodeposition solution and makes it possible to obtain an alloy with a current efficiency of up to 93%, which is not characteristic for the electrodeposition of binary alloys of this type with molybdenum and tungsten.

Ternary CoWRe alloys deposited from a citrate-pyrophosphate electrolyte have high corrosion resistance, especially in neutral (up to 8.9 kΩ·cm²) and alkaline media (up to 3.1 kΩ·cm²). Corrosion resistance of coatings increases by 4 times during exposure of samples in an alkaline solution for one day. The highest corrosion resistance in all investigated solutions is possessed by coatings electrodeposited at current densities of 5–10 mA/cm² and containing 25–35 at.% of refractory elements.

This work was performed with the financial support of the National Academy of Sciences of Ukraine within the state budget theme 'Finishing processing of materials in order to give them unique functional properties' (0123U100650).

REFERENCES

1. J. Zhu, L. Hu, P. Zhao, L. Yoon Suk Lee, and K.-Y. Wong, *Chem. Rev.*, **120**: 851

(2020).
2. F. M. Sapountzi, J. M. Gracia, C. J. (Kees-Jan) Weststrate, H. O. A. Fredriksson, and J. W. (Hans) Niemantsverdriet, *Prog. Energy Combust. Sci.*, **58**: 1 (2017).
3. M. A. Khan, H. Zhao, W. Zou, Z. Chen, W. Cao, J. Fang, J. Xu, L. Zhang, and J. Zhang, *Electrochem. Energy Rev.*, **1**: 483 (2018).
4. Y. S. Yapontseva, A. I. Dikusar, and V. S. Kublanovskii, *Surf. Engin. Appl. Electrochem.*, **50**: 330 (2014).
5. V. S. Kublanovsky and Yu. S. Yapontseva, *Electrocatalysts for Fuel Cells and Hydrogen Evolution—Theory to Design* (Ed. A. Ray) (IntechOpen: 2018).
6. Yu. S. Yapontseva, T. V. Maltseva, V. S. Kublanovsky, O. A. Vyshnevskyi, and Yu. N. Troshchenkov, *J. Refract. Metals Hard Mater.*, **96**: 105469 (2021).
7. H. Kim, J. Kim, G. H. Han, W. Guo, S. Hong, J. Park, and S. H. Ahn, *J. Ind. Eng. Chem.*, **95**: 357 (2021).
8. Yu. Yapontseva, V. Kublanovsky, T. Maltseva, Yu. Troshchenkov, and O. Vyshnevskyi, *Mater. Adv.*, **4**: 3662 (2023).
9. E. Vernickaite, N. Tsyntsaru, K. Sobczak, and H. Cesiulis, *Electrochimica Acta*, **318**: 597 (2019).
10. Yu. Yapontseva, T. Maltseva, and V. Kublanovsky, *Ukrainian Chem. J.*, **86**, No. 9: 28 (2020).
11. Y. Yapontseva, T. Maltseva, V. Kublanovsky, and O. A. Vyshnevskyi, *J. Mater. Research*, **37**: 2216 (2022).
12. H. Cesiulis and A. Budreika, *Physicochem. Mechanics Mater.*, **8**: 808 (2010).
13. E. Vernickaite, N. Tsyntsaru, and H. Cesiulis, *Int. J. Surf. Eng. Coatings*, **94**: 313 (2016).
14. A. Bodaghi and J. Hosseini, *Int. J. Electrochem. Sci.*, **7**: 2584 (2012).
15. G. Yar-Mukhamedova, M. Ved', N. Sakhnenko, and T. Nenastina, *Appl. Surf. Sci.*, **445**: 298 (2018).
16. N. D. Sakhnenko, M. V. Ved, Yu. K. Hapon, and T. A. Nenastina, *Russ. J. Appl. Chem.*, **88**: 1941 (2015).
17. Yu. S. Yapontseva, T. V. Maltseva, V. S. Kublanovsky, and O. A. Vyshnevskyi, *J. Alloys Compd.*, **803**: 1 (2019).
18. Yu. Yapontseva and V. Kublanovsky, *Mater. Sci.*, **2**: 213 (2019).
19. *Electroplating, Anodizing and Metal Treatment Hand Book* (Asia Pacific Business Press Inc.: 2003).
20. H. Cesiulis and A. Budreika, *Physicochem. Mechanics Mater.*, **8**: 808 (2010).
21. B. Viswanathan, *Catalysis: Principles and Applications* (Narosa: 2002).
22. B. E. Conway and B. V. Tilak, *Electrochem. Acta*, **47**: 3571 (2002).
23. V. V. Kuznetsov, Y. D. Gamburg, M. V. Zhalnerov, V. V. Zhulikov, and R. S. Batalov, *Russ. J. Electrochem.*, **52**: 901(2016).
24. C. Wang, H. K. Bilan, and E. J. Podlaha, *J. Electrochem. Soc.*, **166**: F661 (2019).

Metallophysics and Advanced Technologies
Металофіз. новітні технол.
Metallofiz. Noveishie Tekhnol.
2024, vol. 46, No. 5, pp. 507–515
https://doi.org/10.15407/mfint.46.05.0507
Reprints available directly from the publisher

PACS numbers: 01.60.+q

До 95-річчя від дня народження Михайла Олександровича Кривоглаза

А. І. Карасевський, В. А. Татаренко

Інститут металофізики ім. Г. В. Курдюмова НАН України,
бульв. Академіка Вернадського, 36,
03142 Київ, Україна

18 травня 2024 р. виповнилося 95 років від дня народження визначному фізику-теоретику, двічі лавреату Державної премії УРСР в галузі науки і техніки (у 1978 та 1988 рр.), лавреату премії імені Є. С. Федорова АН СРСР (у 1986 р.), члену-кореспонденту АН УРСР (від 1978 р.) Михайлу Олександровичу Кривоглазу. Далі охарактеризовано основні його праці.

Михайло Олександрович народився у Києві 18 травня 1929 року. Батько Михайла Олександровича був юристом, мати — вчителькою російської мови та літератури. Після закінчення із золотою медаллю у 1945 році середньої школи № 25 м. Києва Михайло Олександрович вступив до Київського державного університету на фізичний факультет, який закінчив з відзнакою у 1950 році.

Через рік після закінчення університету М. О. Кривоглаз почав працювати в Лабораторії металофізики АН УРСР інженером (1951–1954), молодшим науковим співробітником (1954–1959), старшим науковим співробітником (1959–1963). Після захистів кандидатської (1954) і докторської (1962) дисертацій у 1964 р. він очолив лабораторію (відділ) Інституту металофізики АН УРСР.

Corresponding author: Anatoliy Illich Karasevskii
E-mail: akarasevskii@gmail.com

G. V. Kurdyumov Institute for Metal Physics, N.A.S. of Ukraine,
Academician Vernadsky Blvd., Bldg. 36, UA-03142 Kyiv, Ukraine

Citation: A. I. Karasevskii and V. A. Tatarenko, On the Occasion of the 95th Anniversary of Birthday of Mykhaylo Oleksandrovych Kryvohlaz, *Metallofiz. Noveishie Tekhnol.*, **46**, No. 5: 507–515 (2024) (in Ukrainian).
DOI: 10.15407/mfint.46.05.0507.

Чл.-кор. АН УРСР, д.ф.-м.н., проф. М. О. Кривоглаз (18.05.1929–30.06.1988)

П'ятдесяті роки минулого століття були роками активного дослідження фізичних властивостей конденсованої речовини. Були відкриті та вивчались явища надпровідности металів, надплинности рідкого гелію, фазових переходів I та II роду в твердих тілах і рідинах.

До початку 1960-х років в Інституті металофізики сформувався колектив плідно працюючих молодих співробітників, які активно досліджували фізичні властивості конденсованих речовин (надпровідність металів, надплинність рідкого гелію, фазові переходи I і II роду в твердих тілах і рідинах), обґрунтовували дислокаційну концепцію пластичної деформації матеріялів, з'ясовували дефектну структуру кристалів, впорядкування та розпад металевих стопів, активно вивчали напівпровідникові властивості матеріялів, розвивали нові методи визначення фазового складу та структури неідеальних кристалів і стопів.

1. ПОЛЯРОНИ

Керівником дипломної роботи М. О. Кривоглаза був один з провідних учених у галузі теорії твердого тіла — Соломон Ісакович Пекар, який незадовго до початку співпраці з М. О. Кривоглазом ввів у фізику уявлення про полярони — автолокалізовані стани електронів у полярному середовищі, яка привернула до цього явища увагу фізиків усього світу. Подальша спільна робота М. О. Кривоглаза та С. І. Пекара привела до розробки нового математичного підходу в теоретичному описі поляронів, який дав змогу досліджувати полярони за будь-яких температури та величини електрон-фононної взаємодії — із сильним, проміжним і слабким зв'язком електронів провідности з поздовжніми коливаннями атомів кристалу. Розроблений теоретичний підхід ґрунтувався на обчисленні статистичної суми системи як сліду оператора (Гамільтоніяна), який описує взаємодію електронів з поздовжніми коливаннями атомів кристалу. Одержані результати використовувалися для аналізи впливу поляронного ефекту на термодинамічні та кінетичні властивості електронів у кристалах.

2. ОПТИЧНІ СПЕКТРИ ПОГЛИНАННЯ ТА БЕЗФОНОННІ ЛІНІЇ

У 1953 році М. О. Кривоглаз і С. І. Пекар передбачили наявність надзвичайно вузьких ліній у спектрах оптичного поглинання домішок у кристалах [2]. Вузькість спектральних ліній пов'язана з тим, що імпульс поглинання або випромінювання фотона передається кристалу в цілому, і в результаті відсутнє Допплерове розширення ліній, спричинене тепловим рухом атомів. На жаль, статтю М. О. Кривоглаза та С. І. Пекара про безфононні лінії оптичного поглинання домішок у кристалах було опубліковано в «Трудах Института физики АН УССР», які не перекладалися англійською мовою; тому ця робота протягом тривалого часу залишалася маловідомою. Аналогічний ефект, — вузькі безфононні лінії в спектрах γ-поглинання домішковими ядрами, — був відкритий Мессбауером у 1957 році, за що він отримав Нобелівську премію. А безфононні лінії в оптичному спектрі почали називати оптичним аналогом Мессбауерового ефекту. М. О. Кривоглазом було встановлено, що розширення безфононних ліній (модуляційне розширення) може бути пов'язане з ангармонізмом фононів або зміною їхніх частоти та координат під часи фотопереходу, тобто під час квазипружнього розсіювання фононів на електронному центрі. У 1965 році був опублікований огляд М. О. Кривоглаза «Эффект Мёссбауера и его применение в физике твёрдого тела» [3], в якому було докладно проаналізовано можливості використання Мессбауерового ефекту для вивчення електронної

структури твердих тіл, мікроструктури кристалу, ангармонізму коливань його атомів, дифузійної рухливости атомів у середовищі та ін.

3. ТЕОРІЯ ТЕПЛОВИХ ПЕРЕХОДІВ

У 1953 році М. О. Кривоглазом було показано, що в полярному середовищі теплові флюктуації поляризації навколо донорного та акцепторного центрів приводять до зміщення донорного та акцепторного електронних рівнів, що може створити резонансні умови для безвипромінювального квантового переходу електрона між цими рівнями [4]. На жаль, М. О. Кривоглаз обмежився розглядом безвипромінювального переходу електрона на одному центрі. На початку 1960-х років американський фізик Р. Маркус запропонував теорію, яка розглядала перенесення електрона в полярному розчиннику між просторово відокремленими донором і акцептором. У 1985 році Р. Маркусу було присуджено Нобелівську премію з хемії за пояснення механізму редокс-реакцій.

4. ТЕОРІЯ СТОПІВ І СИЛЬНО АНІЗОТРОПНИХ КРИСТАЛІВ

М. О. Кривоглазом були значно розвинуті термодинамічна та статистична теорії впорядкування та розпаду стопів, мікроскопічна теорія дифузії у стопах з упорядкуванням і розпадом, розвинуті теорії розчинности й утворення вакансій у різного типу стопах з упорядкуванням; він розвинув багатоелектронну теорію залишкового електроопору багатокомпонентних твердих розчинів з упорядкуванням, побудував кінематичну теорію розсіювання випромінень у твердих розчинах та ін.

4.1. Упорядкування атомів у стопах

На початку 1960-х років значну частину наукових інтересів М. О. Кривоглаза становила теорія упорядкування та розпаду стопів. Він успішно розвивав як термодинамічну, так і статистичну теорію впорядкування та розпаду стопів. В рамках різних теоретичних моделів було розглянуто розпад і впорядкування різних, головним чином, бінарних, стопів. Результати цих досліджень представлено у широко відомій монографії [5].

4.2. Дифузія у стопах

Принципово нові результати були одержані М. О. Кривоглазом

стосовно розробки теорії дифузії в твердих розчинах, що впорядковуються.

Було встановлено, що головна відмінність механізму дифузії у стопах, в порівнянні з дифузією в однокомпонентних системах, полягає в тому, що в розчинах рельєф потенціяльної енергії в процесі дифузії атома змінюється в залежності від локальної концентрації розчину; тому Арреніюсова температурна залежність коефіцієнта дифузії у стопах не застосовна [6].

4.3. Розчинність. Розпад стопів

У роботах М. О. Кривоглаза [7, 8] було запропоновано статистико-термодинамічний модель розчинности атомів третього компонента у міжвузлях або вузлах кристалічних ґратниць бінарних стопів заміщення. Досліджено вплив домішки деякого елемента, розміщеного в октаедричних міжвузлях стопу заміщення, що розпадається. Одержано рівняння для визначення залежности температури розпаду від складу стопу, тобто діяграми стану стопу.

4.4. Міжатомові взаємодії у стопах і сильно анізотропних кристалічних системах

Спільне застосування статистико-термодинамічного флюктуаційного методу та термодинамічної теорії збурень дало змогу М. О. Кривоглазу вивести аналітичний вираз, який отримав у світовій літературі назву «формула Кривоглаза–Клеппа–Мосса». За допомогою цієї формули достатньо просто можна пов'язати експериментально спостережувану інтенсивність дифузного розсіяння з фур'є-компонентами енергій змішання атомів у невпорядкованому стопі [9, 10]. Важливою перевагою такого підходу є можливість врахування далекосяжних внесків у міжатомові взаємодії, що актуально для застосування до реальних стопів.

Крім того, у реальних кристалах істотну роль відіграє деформаційна взаємодія точкових дефектів. На основі методів статики ґратниці (Мацубари–Кривоглаза–Канзакі–Харді) М. О. Кривоглазу вдалося врахувати цю взаємодію точкових дефектів.

5. ТЕОРІЯ РОЗСІЯННЯ РЕНТҐЕНОВИХ ПРОМЕНІВ У НЕІДЕАЛЬНИХ КРИСТАЛАХ

Найбільш значний внесок у теорію твердого тіла пов'язаний з видатними роботами М. О. Кривоглаза зі створення та розвитку кінематичної теорії розсіяння Рентґенових променів і нейтронів кристалами з дефектами. Ним було розроблено ефективний метод

флюктуаційних хвиль для опису спектрального розподілу зміщень, утворених дефектами в кристалах [9–12].

5.1. Класифікація дефектів кристалу

М. О. Кривоглазом вперше в рамках кінематичної теорії було проведено класифікацію дефектів за створюваним ними ефектом на картині рентґенівського розсіяння. Було показано, що належність дефектів кристалу до першого або другого класу визначається закономірностями спадання полів зміщень з віддаленням від дефекту.

До першого класу відносяться дефекти, поле зміщень від яких відносно швидко зменшується з віддаллю ($\propto 1/r^3$ або швидше). До них належать, наприклад, точкові дефекти, зародки частинок другої фази, флюктуаційні неоднорідності складу. Такі дефекти приводять до зміщення рентґенівських ліній через зміну середнього параметра ґратниці, викликаного наявністю дефектів, до ослаблення інтенсивности цих ліній, а також до появи плавного дифузного розсіяння. Водночас розширення ліній не спостерігається.

У випадку дефектів другого класу (коли поле зміщень $\propto r^{-3/2}$) спостерігається істотне розширення рентґенівських ліній, що пов'язано зі зростанням фактора Дебая–Валлера. До дефектів другого класу можуть бути віднесені прямолінійні дислокації, дислокаційні петлі, великі частинки другої фази тощо.

Для кількісного опису й аналізи впливу дефектів різного типу М. О. Кривоглазом зі співробітниками були розроблені різні підходи. Наприклад, було показано, що у кристалах з хаотичним розподілом дислокацій ширина квазиліній на дебаєграмі пропорційна квадратному кореню з густини дислокацій. М. О. Кривоглазом було побудовано теорію розсіяння у випадку нехаотичного розподілу дислокацій та об'єднання їх у стінки; розглянуто випадок, коли є як стінки, так і хаотично розподілені дислокації; побудовано теорію розсіяння у квазиодновимірних і квазидвовимірних системах тощо. Більшість передбачених М. О. Кривоглазом рентґенографічних ефектів знайшла своє експериментальне підтвердження й отримало широке практичне застосування як теоретична основа сучасних методів діягностики дефектів [9–13].

6. ТЕОРІЯ НЕДОСКОНАЛОСТЕЙ КРИСТАЛІЧНОЇ ҐРАТНИЦІ

6.1. Рух включень у твердих тілах

Дисперсні системи, що складаються з частинок розміром у 10–

10^3 Å, включених у матричну фазу, проявляють ряд специфічних властивостей і мають велике практичне значення. Змінюються характеристики міцности, підвищується жароміцність тощо. Високотемпературна плазучість таких систем істотно відрізняється від гомогенних систем, що пов'язане, головним чином, з дифузійною рухливістю включень або пор [14]. Сили, що приводять до руху включень, створюються різними чинниками. Дифузійний рух відбувається під дією зовнішніх сил — ґрадієнтів температури або концентрації, електричного або магнетного поля, різної концентрації дислокацій або вакансій, на межі поділу фаз тощо.

6.2. Зміщення температури мартенситного перетворення в магнетному полі

М. О. Кривоглазом були проведені дослідження [15, 16], які пояснювали виявлений В. Д. Садовським ефект зміщення температури мартенситного перетворення у криці в сильному імпульсному магнетному полі. Причина цього ефекту полягає в тому, що мартенситна фаза, на відміну від аустенітної, є феромагнетною, і тому зовнішнє магнетне поле понижує її термодинамічний потенціял, викликаючи фазове перетворення в аустенітній фазі у магнетному полі.

7. ЕЛЕКТРОННІ СТАНИ В КРИСТАЛАХ. ФЛЮКТУОНИ

7.1. Флюктуони

В 1960-х роках у фізиці конденсованого стану накопичилися експериментальні дані, що свідчать про наявність автолокалізованих станів електронів у ряді неполярних систем, таких як рідкі гелій та інертні гази Ne, Xe, Ar, неполярні рідини, деякі магнетні напівпровідники. В той же час локалізовані стани електронів у рідинах, таких як вода (гідратований електрон), або в метал-аміякових розчинах, істотно відрізнялися за своїми властивостями від поляронів у йонних кристалах.

У 1969 році, виходячи з геніяльної ідеї С. І. Пекара про полярон, М. О. Кривоглаз запропонував загальний теоретичний підхід щодо опису автолокалізації електронів у невпорядкованих середовищах [17]. Були одержані основні рівняння, які визначають умови виникнення та характеристики флюктуонів — утворень, в яких електрон локалізується на флюктуації близького порядку середовища, яку він же самоузгоджено підтримує.

Найпростіші автолокалізовані стани можуть виникати у напівпровідниках біля точок фазового переходу першого роду, коли на

ділянці нової фази потенціяльна енергія електрона понижується на певну величину відносно дна зони провідности напівпровідника. Флюктуони можуть виникати в магнетних напівпровідниках, напівпровідникових розчинах, а також у сеґнетоелектриках. У напівпровідникових розчинах або магнетиках в ефективному полі локалізованого електрона може відбуватися неперервна зміна внутрішнього параметра. На відміну від полярона, де йони набувають лише невеликих зміщень з положення рівноваги, у випадку флюктуонів в середовищі в області локалізації електрона відбувається істотна реорганізація, і електрон стабілізує кластер з атомів одного сорту.

7.2. Термодинамічно рівноважні гетерогенні стани [18]

Дисперсні системи широко поширені в природі. Однак через додаткову міжфазну енергію вони термодинамічно нестійкі та з часом мають коаґулювати, утворюючи масивну гомогенну фазу.

М. О. Кривоглаз вперше звернув увагу на те, що вільні (незв'язані) заряди є тими компонентами системи, перерозподіл яких між фазами приводить до пониження енергії, яке пропорційне площі міжфазної межі, а далекосяжні Кулонові сили, що водночас виникають, фіксують розмір частинки. Розмір утворюваних частинок має величину порядку радіюса Томаса–Фермі виродженого електронного газу. Форма дисперсних частинок залежить від екранування їхнього заряду в середовищі.

За достатньо високої концентрації вільних електронів у однорідному напівпровіднику енергетично вигіднішими порівняно з флюктуонами можуть стати області зміненого параметра середовища, стабільність яких підтримується виродженим газом електронів, які перейшли з оточувального середовища на частинки з металічною густиною електронного газу. У сильно вироджених напівпровідниках за невеликої величини константи взаємодії електронів у порівнянні з енергією Фермі електронного газу зі зміною концентрації розчину або намагнетованости умови гетерогенізації значно змінюються.

Перехід системи в гетерогенний стан відбувається як фазовий перехід першого роду, в результаті якого утворюється модульована структура [19].

Після смерті М. О. Кривоглаза пройшло вже 36 років, але досі на міжнародних конференціях і в наукових журналах цитуються його роботи й обговорюються його наукові ідеї, а тим послідовникам, хто працював разом із Михайлом Олександровичем (і навіть просто поряд з ним), використовуючи його ідеї та напрацювання, вони слугують дороговказом у світі фізичної науки.

ЦИТОВАНА ЛІТЕРАТУРА

1. М. А. Кривоглаз, С. И. Пекар, Метод шпуров для электронов проводимости в полупроводниках, *Изв. АН СССР. Сер. физ.*, **21**, вып. 1: 3–32 (1957).
2. М. А. Кривоглаз, С. И. Пекар, Форма спектров примесного поглощения света и люминесценции в диэлектриках, *Труды Института физики АН УССР*, вып. 4: 37–70 (1953).
3. М. А. Кривоглаз, *Физика твердого тела. Теория твердого тела. Серия «Итоги науки»* (Москва: ВИНИТИ: 1965), с. 7–125.
4. М. А. Кривоглаз, Теория тепловых переходов, *ЖЭТФ*, **25**, вып. 2: 191–207 (1953).
5. М. А. Кривоглаз, А. А. Смирнов, *Теория упорядочивающихся сплавов* (Москва: Физматгиз: 1958).
6. М. А. Кривоглаз, А. А. Смирнов, Теория диффузии внедренных атомов в упорядочивающихся сплавах, *ЖЭТФ*, **24**, вып. 4: 409–418 (1953).
7. М. А. Кривоглаз, Растворимость водорода в упорядочивающихся сплавах, *ЖТФ*, **24**, вып. 6: 1077–1089 (1954).
8. М. А. Кривоглаз, А. А. Смирнов, Влияние примеси внедренных атомов на распад сплавов, *ЖФХ*, **29**, вып. 8: 1532–1534 (1955).
9. М. А. Кривоглаз, Теория диффузного рассеяния рентгеновских лучей и тепловых нейтронов твердыми растворами, *ЖЭТФ*, **32**, вып. 6: 1368–1381 (1957).
10. М. А. Кривоглаз, *Теория рассеяния рентгеновских лучей и тепловых нейтронов реальными кристаллами* (Москва: Наука: 1967).
11. М. А. Кривоглаз, *Дифракция рентгеновских лучей и нейтронов в неидеальных кристаллах* (Киев: Наукова думка: 1984).
12. М. А. Кривоглаз, *Диффузное рассеяние рентгеновских лучей и нейтронов на флуктуационных неоднородностях в неидеальных кристаллах* (Киев: Наукова думка: 1984).
13. М. А. Кривоглаз, К теории рассеяния рентгеновских лучей кристаллами, содержащими дефекты, *ФММ*, **12**, вып. 4: 465–475 (1961).
14. Я. Е. Гегузин, М. А. Кривоглаз, *Движение макроскопических включений в твердых телах* (Москва: Металлургия: 1971).
15. М. А. Кривоглаз, В. Д. Садовский, О влиянии сильных магнитных полей на фазовые переходы, *ФММ*, **18**, вып. 4: 502–505 (1964).
16. М. А. Кривоглаз, В. Д. Садовский, Л. Ф. Смирнов, Е. А. Фокина, *Закалка стали в магнитном поле* (Москва: Наука: 1977).
17. М. А. Кривоглаз, Флуктуонные состояния электронов, *УФН*, **111**, № 4: 617–654 (1973).
18. М. А. Кривоглаз, О возможности существования равновесной дисперсной фазы, содержащей металлические частицы, *ЖЭТФ*, **63**, вып. 2: 670–683 (1972).
19. B. V. Egorov, I. B. Egorova, M. A. Krivoglaz, The electronic heterogeneous states in ferromagnetic semiconductors, *phys. stat. sol. (b)*, **139**, No. 1: 173–184 (1987).

Засновник: Національна академія наук України, Інститут металофізики ім. Г. В. Курдюмова НАН України
Видавець: ВД «Академперіодика» НАН України
Передплатний індекс/Subscription index: 74312 ISSN 1024-1809

Інформація для передплатників журналу
«МЕТАЛОФІЗИКА ТА НОВІТНІ ТЕХНОЛОГІЇ»

Редакція журналу МНТ повідомляє читачів про передплату (що починається з будь-якого місяця випуску). Журнал МНТ входить за індексом **74312** до «Каталогу видань України». Рекомендуємо оформити передплату
1) у відділеннях поштового зв'язку через централізоване аґентство ДПРПВ «ПРЕСА» (вул. Георгія Кирпи, буд. 2[a], 03999 Київ, Україна; телефакси: +380 44 2890774 / 2480377 / 2480384 / 2487802 / 2480406); e-mail: pod_ukr@presa.ua, rozn@presa.ua, info@presa.ua) або
2) через Internet:

http://presa.ua/metallofizika-i-novejshie-tehnologii.html?___SID=U

(передплатний індекс МНТ: 74312) або ж
3) безпосереднім перерахуванням від **170 грн.** за один випуск до **2040 грн.** за один том (12 випусків на рік):
«ОТРИМУВАЧУ»: Інститут металофізики ім. Г. В. Курдюмова НАН України
на розрахунковий рахунок № UA058201720313291001201001901 в банку ГУДКСУ в м. Києві
Код банку: 820172
Код єдиного державного реєстру підприємств і організацій України (ЕДРПОУ): 05417331
Для «ПОСТАЧАЛЬНИКА» — Інституту металофізики ім. Г. В. Курдюмова НАН України
Свідоцтво платника податку на додану вартість (ПДВ) № 36283185, індивідуальний податковий номер (ІПН) 054173326066
Код призначення платежу: 25010100
ПРИЗНАЧЕННЯ ПЛАТЕЖУ: за журнал «Металофізика та новітні технології» (том(и), номер(и), рік(роки)) для РВВ ІМФ НАНУ
ПІДСТАВА: передоплата 100%.

INFORMATION FOR FOREIGN SUBSCRIBERS

Editorial Board of a Monthly Research Journal 'Metallophysics and Advanced Technologies' (transliteration: **'Metallofizika i Noveishie Tekhnologii'**) (CODEN: MNTEEU; ISSN: 1024-1809) advertises the subscription on an annual basis. Orders should be placed through one of the methods described below. Besides the subscription *via* the centralized service by State Enterprise 'PRESA' (2[a] Georgiy Kyrpa Str., UA-03999 Kyiv, Ukraine; faxes: +380 44 2890774 / 2480377 / 2480384 / 2487802 / 2480406 / 2487809; e-mail: pod_ukr@presa.ua, rozn@presa.ua, info@presa.ua) or *via* Internet:

http://presa.ua/metallofizika-i-novejshie-tehnologii.html?___SID=U

the Editorial Board will take orders sent directly to the Editorial Board. To obtain our journal, the persons and institutions, interested in this title, should made the definite payment sent, according to the order, to the account of the Publisher—G. V. Kurdyumov Institute for Metal Physics of the N.A.S. of Ukraine.
The journal frequency is 12 issues per year. The annual subscription rate for 'Metallophysics and Advanced Technologies' is 156 USD (or 132 EUR), including airmail postage, packing and handling charges. All other-currency payments should be made using the current conversion rate set by the Publisher (subscribers should contact the Editorial Board).
Subscription is valid after obtaining by the Editorial Board of banker's order. Banker's order should be sent to the address:
G. V. Kurdyumov Institute for Metal Physics, N.A.S. of Ukraine,
currency account No. UA603223130000025308000000067, MFO 322313,
in the Kyiv's Branch of JSC 'The State Export-Import Bank of Ukraine' (Public Joint Stock Company 'Ukreximbank') (11[b] Bulvarno-Kudryavska Str., UA-04053 Kyiv, Ukraine)
simultaneously with written notice providing the Editorial Board with a copy of banker's order for subscription and detailed address for mailing.
Prepayment is 100%.
Address of the Editorial Board: G. V. Kurdyumov Institute for Metal Physics, N.A.S. of Ukraine, 36 Academician Vernadsky Blvd., UA-03142 Kyiv, Ukraine.
E-mail: mfint@imp.kiev.ua (with subject beginning by word 'mfint')
Fax: +380 44 4242561. Phone: +380 44 4249042, +380 4241221.
After receiving of banker's order, the Editorial Board will send the guarantee letter to the subscriber's address for mailing the journal for a corresponding term.

The Editorial Board of this journal hopes for effective co-operation with its present and future readers and requests to promote the maximum information about its contents to persons and organizations concerned.